ON THE STRUCTURE AND DYNAMICS OF THE MARTIAN MIDDLE ATMOSPHERE

by

Tamara Lea McDunn

A dissertation submitted in partial fulfillment
of the requirements for the degree of
Doctor of Philosophy
(Atmospheric and Space Sciences)
in The University of Michigan
2012

Doctoral Committee:

Collegiate Research Professor Stephen W. Bougher, Chair
Professor Edwin A. Bergin
Emeritus Professor Andrew F. Nagy
Professor Nilton O. Rennó
Michael A. Mischna, Jet Propulsion Laboratory

ACKNOWLEDGEMENTS

I'd like to take this space to attempt to express my gratitude to the many people who in one way or another helped make this thesis possible. To begin, I'd like to thank my thesis advisor Dr. Stephen Bougher for bringing me to Michigan and for his on-going support and mentorship throughout my graduate career. You have taught me how to do research: how to ask questions, how to set about trying to answer them, and how to communicate what I find. You've also shared your wisdom and taught me that, with the right attitude and a little time, criticism can be received as a constructive gift! And you've taught me how to navigate a career in research yet still balance it with the most important things in life. Thank you.

Next, to the other members of my thesis committee, Dr. Andy Nagy, Dr. Michael Mischna, Dr. Nilton Rennó, and Dr. Ted Bergin: thank you for your thoughtful and insightful questions and feedback. I'd also like thank Dr. Nagy, Dr. Mischna, and Dr. Jim Murphy who have acted as informal mentors to me. Thank you for the interest you've taken in my work and the time and energy you've each spent helping me to develop as a scientist, challenging me with questions and encouraging me to ask my own. Thank you, too, to my undergraduate meteorology professors, Dr. Bart Wolf, Dr. Teresa Bals-Elsholz, and Dr. Craig Clark, who profoundly influenced my education and my outlook on science.

Next, I'd like to acknowledge my collaborators. For the study presented in Chapter 2: Dr. Bougher, Dr. Murphy, Dr. Smith, Dr. François Forget, Dr. Jean-Loup Bertaux, and Dr. Franck Montmessin. For the study presented in Chapter 3: Dr.

Bougher, Dr. Murphy, Dr. Armin Kleinböhl, Dr. Forget, Dr. Bob Tolson, and Dr. Smith. And for the study presented in Chapter 4: Dr. Bougher, Dr. Murphy, and Dr. Mischna. I'd like to also acknowledge my funding sources: the Rackham Graduate School at the U. of Michigan (Rackham Engineering Award II) and NASA (NESSF award), as well as NCAR and JPL for providing the super computer resources necessary for this thesis work.

Next, I'd like to thank my fellow graduate students. Many of you showed me the ropes as I was coming into graduate school, or we learned together during late-night homework and study sessions. Amanda Brecht, Dave Pawlowski, Ahmed Tawfik, Kristen Mihalka, Dan Gershman, Manish Mehta, Matt Trantham, Jacob Gruesbeck, Yiqun Yu, Jared Bell, Anna DeJong, Dan Welling, Erika Roesler, Dave Applbaum, and Josh Adamson: grad school would have been a lonely road without you guys. I also send my thanks to the AOSS faculty and administrative and IT staff for all they do to make AOSS a great place to be a grad student.

To some dear friends, Everett Mayes, Joanne Borchert, Heidi Nathan, Luke Ellison, Erik Swenson, Eileen Q., and Sue W.: your love, understanding, and companionship has helped keep me whole.

And finally, I'd like to thank my family, whose love time and again made it possible to regain the perspective needed to make it through the emotional challenges of graduate school (and my 20s! ha.). Mom and Dad, you've shown me the meaning of unconditional love, hard work, inquisitiveness, and humility. What's more, you've always encouraged me to seek out what makes me fulfilled and do my best at it, and have loved me regardless of the result. I couldn't ask for more. Tara, you've been my best friend and an unfaltering example of how to maintain humanity, compassion, and humor despite tremendous stress. Thank you. Peter and Madeline, you've both shown me how much more there is in life. Thank you to Buggie, Robbie, Huebes, and Adrienne, for your un-ending encouragement. And to Grandpa Quentin for

showing me the meaning of strength and love, to Grandpa Adrian for showing me the meaning of strong will and confidence, to Grandma Joyce for showing me the meaning of gentleness, courage, and quiet strength, and to Grandma Ginnie for showing me the meaning of grace. To all of you, from the bottom of my heart, thank you.

PREFACE

The entire scope of this research was not foreseen at the outset of my graduate studies. Instead, each project has arisen in response to the results of the previous project and the best-available observations and modeling capabilities at the time. Therefore this dissertation is not a discourse on one over-arching question but rather is an accumulation of the work undertaken in the course of my graduate career (though I attempt here to make it read as cohesively as possible as a single document). As such, following the introduction, this thesis is organized chronologically by the projects I worked on. Much of the content of Chapters 2, 3, and 4 can be found in the first-author journal articles generated by this thesis work.

TABLE OF CONTENTS

LIST OF FIGURES

Figure

LIST OF TABLES

Table

LIST OF APPENDICES

Appendix

LIST OF ABBREVIATIONS

ACC accelerometer

AU astronomical unit

CFL Courant-Friedrichs-Lewy

DISORT Discrete-Ordinate Model of Radiative Transfer

DoD Department of Defense

EDL entry, descent, and landing

ESA European Space Agency

GCM general circulation model

GDS global dust storm

GFDL Geophysical Fluid Dynamics Laboratory

GWMD gravity wave momentum deposition

IRIS Infrared Interferometer Spectrometer

IRR Infrared Radiometer

LMD Laboratoire de Météorologie Dynamique

LBLRTM Line-by-Line Radiative Transfer Model

LT local time

MarsWRF Mars Weather Research and Forecasting General Circulation Model

MAVEN Mars Atmosphere and Volatile Evolution

MCS Mars Climate Sounder

MER Mars Exploration Rovers

MEX Mars Express

MGCM Mars General Circulation Model

MGS Mars Global Surveyor

MOLA Mars Orbiter Laser Altimeter

MPF Mars Pathfinder

MRO Mars Reconnaissance Orbiter

MTGCM Mars Thermosphere General Circulation Model

MY Mars Year

M-GITM Mars-Global Ionosphere Thermosphere Model

NASA National Aeronautics and Space Administration

NCAR National Center for Atmospheric Research

nLTE non-local thermodynamic equilibrium

NOAA National Oceanic and Atmospheric Administration

ODY Mars Odyssey

PW polar warming

SPICAM Spectroscopy for the Investigation of the Characteristics of the Atmosphere of Mars

TES Thermal Emission Spectrometer

TGCM Thermosphere General Circulation Model

THEMIS Thermal Emission Infrared Spectrometer

UCLA University of California, Los Angeles

VL Viking Lander

XRFS X-Ray Fluorescence Spectrometer

ABSTRACT

ON THE STRUCTURE AND DYNAMICS OF THE MARTIAN MIDDLE ATMOSPHERE

by

Tamara Lea McDunn

Chair: Stephen W. Bougher

The martian middle atmosphere (∼50-130 km altitude) is notoriously understudied, yet important for several reasons. It passes upward propagating planetary waves, gravity waves, and thermal tides from the lower atmosphere to the upper atmosphere. It also communicates the seasonal and dust-heating driven expansion and contraction of the lower atmosphere to the upper atmosphere. The middle atmosphere itself can be affected by and affect these dynamical processes. Characterization of this coupling region is therefore necessary if we are to fully understand the lower and upper atmospheres. It is also important for ensuring the safety of spacecraft that pass through this region.

In part one of this thesis we characterize the nightside density and thermal structure in the 80-130 km altitude region as observed by stellar occultations. The nightside mesopause ranges from warm and high (115 K at 118 km) over the tropics during southern summer to cool and low (105 K at 103 km) over middle-southern winter latitudes. Using a general circulation model we find that the temperature and density of the 80-130 km region is significantly affected by even short-term increases in lower

atmospheric dust loading.

In part two, we quantitatively characterize dynamical polar warming (PW) over three martian years. Unexpectedly we find that during a typical dust year the magnitude of PW is larger during the $L_s = 180^\circ$ equinox than during northern winter, and it is comparable during southern winter and northern winter. Moreover, during equinoxes, the magnitude of PW is larger in the southern hemisphere than in the northern hemisphere. Results from this work provide quantitative constraints for model calculations of middle-atmosphere temperatures and winds.

We close with part three, in which we use a general circulation model to investigate the role that the forcings generated by dust heating and by gravity wave momentum deposition play in producing the observed PW trends from part two. We show that while the effects of dust heating upon the mean meridional circulation contribute significantly to PW, they are insufficient for producing its precise magnitude, vertical distribution, and seasonality. Gravity wave momentum deposition shows promise for improving modeled PW.

CHAPTER I

Introduction to the Martian Atmosphere

1.1 A Brief Introduction to Mars

As one of the closest and brightest objects in the nightsky, Mars has captivated human imaginations and intellects for ages. The fourth planet from the Sun and arguably the most Earth-like planet, Mars is interesting for both its similarities and differences from Earth. In this thesis we explore some of each, specifically as pertains to the atmosphere.

In this chapter we will become acquainted with Mars. We focus in this section on those aspects of its orbit, physical properties, surface, and interior that have implications for the atmosphere. The atmosphere itself will be discussed in the subsequent sections. As we are most familiar with the properties of Earth and the ramifications they hold for an atmosphere, much of the discussion that follows will be of a comparative nature, drawing out the similarities and differences for the case of Mars. To avoid cluttering this chapter with the same five references over and again, let us state here that the main sources for the information within this chapter are *Kieffer et al.* (1992), *Read and Lewis* (2004), *Forget et al.* (2008), *Bougher et al.* (submitted 2011), and *Smith et al.* (submitted 2011).

A comparison of the orbital properties of Mars and Earth can be found in Table 1.1. Mars has an angular rotation rate of 7.088 x 10^{-5}s^{-1}, just slightly slower than

Table 1.1: Orbital properties of Mars and Earth.

Property	Mars	Earth
Angular rotation rate, Ω (s^{-1})	7.088e-5	7.294e-5
Solar day, sol (h)	24.6597	24
Mean orbital radius (AU)	1.52	1
Mean solar constant (W m^{-2})	589.2	1367
Solar year (sol)	668.6	365.24
Orbital eccentricity	0.093	0.017
Perihelion distance (AU)	1.38	0.98
Aphelion distance (AU)	1.67	1.02
Obliquity (°)	25.19	23.93
Longitude of Perihelion (°)	251	281
Longitude of Aphelion (°)	71	103

Earth's. Consequently, the length of a solar day (sol) on Mars is slightly longer than a day on Earth, measuring 24h 39m 35s. This leads to a diurnal heating pattern on Mars similar to that at Earth. Mars has a mean orbital radius of $\sim$ 1.52 AU[1]). Since electromagnetic radiation scales as one over the distance squared, one consequence of having a larger orbital radius is that Mars receives on average just 45% the solar radiation that Earth does. This leads to a cooler equilibrium temperature for Mars than for Earth (see Table 1.2). Another consequence of Mars's larger orbital radius is that its orbital period (year), is 686.97 sols, nearly twice as long as Earth's year. Mars's orbit is also more eccentric than Earth's, with a perihelion (closest approach to the Sun) of 1.38 astronomical unit (AU) and an aphelion (farthest approach to the Sun) of 1.67 AU (Figure 1.1). This means that Mars experiences a wider range of radiation conditions over the course of a year than Earth, leading to more dramatic seasonal variability. Another orbital parameter of interest is the obliquity of the planet's spin axis to its orbital plane. Mars's present day obliquity is very similar to Earth's. This means that the subsolar point (i.e., the latitude that receives direct solar radiation at local noon) migrates between roughly the same latitudes over the course of a year on Mars (25.19°S to 25.19°N) as it does on Earth (23.93°S to 23.93°N). In

[1]An AU is the average orbital radius of Earth, defined as AU = 1.50 x 10^{11} m.

Table 1.2: Physical properties of Mars and Earth.

Property	Mars	Earth
Equatorial radius (km)	3389.5	6378
Mass (kg)	6.4185e+23	5.9742e+24
Gravitational acceleration (m s^{-2})	3.72	9.81
Escape velocity, V_{esc} (km s^{-1})	5.03	11.19
Average albedo	0.250	0.306
Equilibrium temperature, T_e (K)	210	256
Mean density (kg m^{-3})	3933	5515

addition, it means that roughly the same portion of the high latitudes (>64.81°) experience polar night (continuous darkness) and polar day (continuous daylight) during local winter and local summer, respectively. The final orbital parameter important for atmospheric studies is the precession. Currently, the precession of Mars is such that aphelion occurs near southern winter solstice (L_s[2]= 90°) and perihelion occurs near the southern summer solstice (L_s = 270°) (see Figure 1.1). This results in the southern hemisphere experiencing more drastic seasonal variability than the northern hemisphere (i.e., southern summer is warmer than northern summer and southern winter is colder than northern winter, similar to the situation on Earth.

The physical properties of a planet also affect its atmosphere. A comparison of the physical properties of Mars and Earth can be found in Table 1.2. The equatorial radius of Mars is approximately one half that of the Earth. Its mass is a factor of 10 less than Earth's, creating a gravitational acceleration at the surface equal to 3.72 ms^{-2}, a little more than one third of Earth's. This has consequences for the velocity required of atmospheric constituents to escape out the topside of the atmosphere, making it easier for molecules and atoms to escape from Mars's atmosphere than from Earth's.

[2]Seasonal dates on Mars are given by areocentric longitude, or L_s, which describes the location of Mars in its orbit around the Sun. L_s = 0° is defined as northern hemisphere spring equinox, with L_s = 90°, 180°, and 270°, denoting northern summer solstice, fall equinox, and winter solstice, respectively. Years on Mars (L_s = 0° to 360°) are designated by a Mars Year (MY) calendar. By convention, MY 1, L_s = 0° is defined as 11 April 1955 (*Clancy et al.*, 2000). The current year is MY 31, which began 13 September 2011.

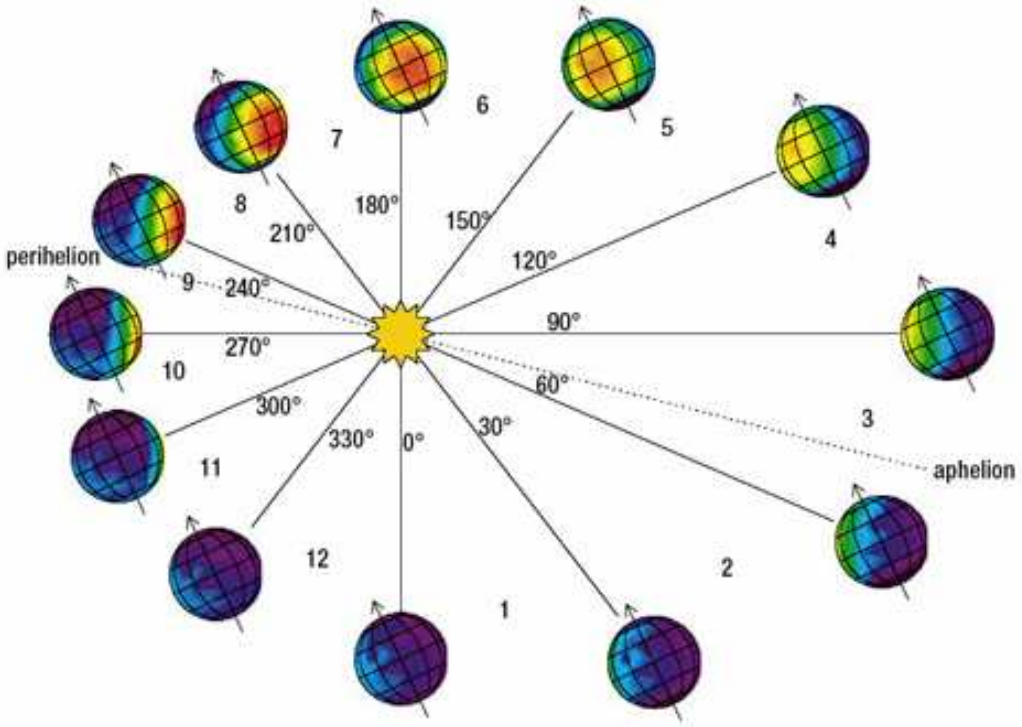

Figure 1.1: Schematic of Mars's orbit indicating the timing of different orbital events. Solid radial lines represent the beginning of each "month" or 30°-L_s interval. Dashed lines represent the planet's closest (perihelion) and farthest (aphelion) approaches to the Sun. Coloring indicates surface temperature representative of the season and the local time shown for each image (as indicated by which portion of the planet is facing the Sun in each position). From: LASP/University of Colorado (lasp.colorado.edu/ bangenal/3720/CLASS22/MarsEvolution.html).

A planet's surface properties also hold interesting ramifications for its atmosphere. Unlike Earth, Mars is a desert planet whose landscape is dominated by large boulders, small rocks, and a layer of fine dust overlying the surface soil and clay (Figure 1.2). As anyone who has ever gazed at Mars in the sky will know, the planet earned its name by virtue of its hue. The surface rock is basaltic in nature. Infrared spectra analysis by the Viking Lander (VL) X-Ray Fluorescence Spectrometer (XRFS) instrument and by Mars Pathfinder (MPF) found the surface soil and dust is composed largely of silicate minerals (mostly SiO_2) with a significant portion of iron oxides (FeO and Fe_2O_3) (*Bandfield et al.*, 2000; *Kieffer et al.*, 1992). The iron oxides preferentially scatter longer wavelengths, giving the planet's surface its characteristic reddish-orange color.

There are (presently) no standing or flowing bodies of water, no known biosphere, and thus no vegetation, on Mars. These factors contribute to a very different weather profile from that at Earth. In addition to the obvious loss of sources and sinks of atmospheric water vapor, the lack of standing or flowing water on the surface of Mars also contributes to a smaller average specific heat of the planetary surface (since water absorbs and holds onto heat longer than the surface does), greater surface relief (oceans and lakes on Earth mask many large topographic features), and a lower surface albedo. The average albedo at Mars (see Table 1.2) is lower than at Earth, meaning a smaller proportion of the incoming solar radiation at Mars is reflected away by the atmosphere or the surface, leaving a larger proportion to be absorbed by the atmosphere or the planetary surface. Furthermore, the latent heat associated with evaporation, condensation, and evapotranspiration on Earth support a climate heavily influenced by moist convection, clouds, and precipitation. Conversely, the latent heat that is important for Mars is that of the deposition and sublimation of carbon dioxide and the dry atmosphere and surface support a climate where dust devils, regional dust storms and even global dust storms are common and comprise

the planet's most significant weather systems. The lack of biosphere and lack of sustained liquid water on the surface have also conspired to allow the geography of Mars to reveal the planet's history.

Hosting both the tallest volcano (Olympus Mons) and the biggest canyon (Valles Marineris) in the solar system, the topographic relief on Mars is some of the most extreme in the solar system. Enormous extinct volcanoes spot the surface, valley systems carve deep into the subsurface, and impact basins bear witness to early impacts that ejected planetary material (Figure 1.3). This large scale topography leads to interesting interactions with the atmosphere (Sections 1.2- 1.4). While the large scale of the relief on Mars is in part due to the absence of oceans, it is also a result of the planet's evolution.

The southern hemisphere is dominated by heavily cratered highlands. These craters bear witness to the heavy bombardment of the planet during its early formation and indicate that the southern highlands are ancient terrain. The northern hemisphere, on the other hand, is dominated by flat lowland plains. This suggests the surface here has been smoothed over by volcanic flows and is therefore relatively young. The fact that the southern highland craters remain indicates that the southern hemisphere was relatively untouched by the ancient volcanic lavas.

A final set of surface features important for the atmosphere of Mars are the seasonal polar caps. These caps are a thin layer of (mostly) CO_2 ice that coat the permanent (and much deeper) water ice caps (see Sections 1.2.3.1 and 1.2.3.3). The seasonal polar caps grow and shrink with the approach and passage of local winter (Figure 1.4). In the northern hemisphere during local summer, the seasonal CO_2 cap completely sublimes back into the atmosphere, leaving the perennial water ice cap exposed. In the southern hemisphere during local summer, the majority of the CO_2 cap sublimes back into the atmosphere but there remains a"residual cap" that never completely returns to the atmosphere. This "permanent reservoir of solidified atmo-

Figure 1.2: A panoramic image of the martian surface taken by the Mars Pathfinder. Image credit: NASA.

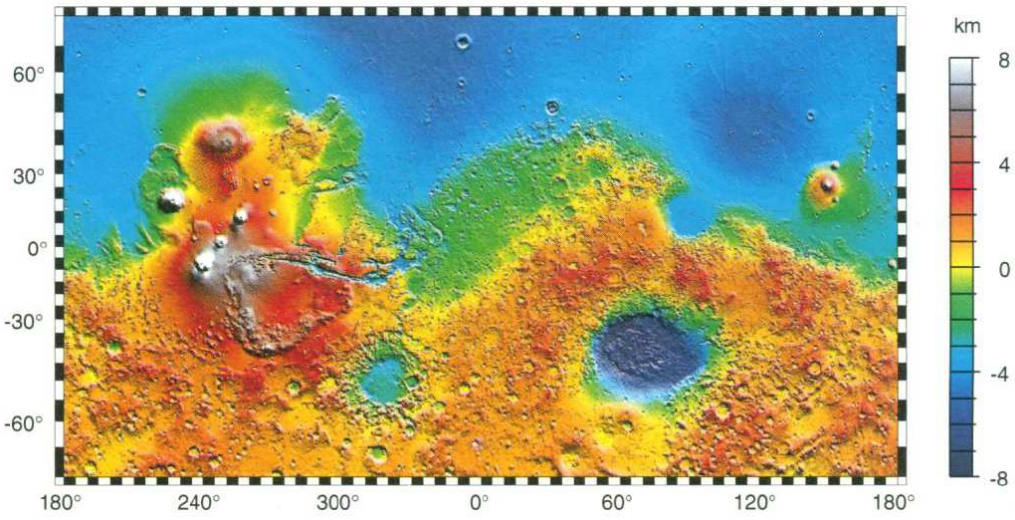

Figure 1.3: Map of Mars' surface topography as observed by MGS-MOLA. Projection is Mercator to 70°. Color scale saturates at elevations above 8 km. From *Smith et al.* (1999).

spheric gas" (*Forget et al.*, 2008) has no analogue on Earth. As will be discussed in the next section, the fact that the major constituent condenses out of the atmosphere during local winter is an exotic phenomenon that has repercussions for the global dynamics and local composition.

Finally, the interior of a planet, particularly the presence or lack of an internal dynamo, has ramifications for the atmosphere and its long term evolution. While Mars currently lacks an internal dynamo, it had one earlier in its history as evidenced by remnant magnetic fields in the planetary crust of the southern highlands. When the ancient dynamo turned off continues to be an active area of research (e.g., *Arkani-Hamed*, 2004). Mars's remnant magnetic fields are the only known instance in the solar system of what are called "crustal magnetic fields." These non-uniform (in distribution and in strength) magnetic anomalies are locked into the surface rocks (*Acuña et al.*, 1999; *Arkani-Hamed*, 2005). They form mini-magnetospheres high above the planet that determine the present-day atmosphere's (highly localized) protection from, and interaction with, the solar wind. In regions where the field lines of the mini-magnetospheres are vertical ("cusps") and in regions devoid of mini-

Figure 1.4: Images of the North Polar Cap taken by the Hubble Space Telescope. The cap shrinks as northern winter (far left) phases into northern spring (far right) and the CO_2 ice of which the seasonal cap is composed sublimates back into the atmosphere. Image credit: Phil James, Todd Clancy, Steve Lee, and NASA (http://hubblesite.org/gallery/album/entire/pr1997015b/).

magnetospheres (e.g., most of the northern hemisphere), the solar wind interacts directly with the neutral upper atmosphere and ionosphere. In such cases the solar wind can ionize atmospheric constituents and create auroral signatures (e.g., *Brain et al.*, 2006) in the cusp regions.

1.2 Entire Atmosphere

1.2.1 Structure

The word atmosphere comes from the greek words "atmos" meaning vapor and "sphaira" meaning ball or globe, which join together to literally denote the globe of vapors or gases that envelopes a planetary body. The atmosphere is a compressible fluid that can largely be described by its macroscopic state variables: pressure (p), density (ρ), and temperature (T) and by its composition and momentum. In this section we will become familiar with these descriptive variables of the martian atmosphere.

Mars's atmosphere is thin compared to Earth's. The average surface pressure is on the order of one hundredth the surface pressure on Earth. Hydrostatic balance assumes that the upward vertical pressure gradient force is balanced by the downward gravitational force

$$\frac{dp}{dz} = -\rho g, \tag{1.1}$$

(forces here are per unit volume), where z is height and g is the gravitational acceleration at the surface (see Table 1.2). Under this assumption, and further assuming an ideal gas

$$p = \rho R T, \tag{1.2}$$

where R is the specific gas constant[3], we arrive at the solution that atmospheric

[3] $R = R^*/M$, where $R^* = 8.314$ JK^{-1}mol^{-1} is the universal gas constant and M is the molar mass of the gas being considered.

Table 1.3: Atmospheric properties of Mars and Earth.

Property	Mars	Earth
Surface pressure, p_{sfc} (Pa)	600	101350
Pressure scale height, H_p (km)	10.8	8
Mean environmental lapse rate, Γ (-K/km)	2.5	6.5
Equilibrium temperature, T_e (K)	210	256
Surface temperature (K)	140-300	230-315

pressure decreases monotonically and exponentially with height

$$p = p_0 \exp(-\frac{z}{H_p}). \tag{1.3}$$

In Eq. 1.3, p_0 is some reference pressure and H_p is the pressure scale height

$$H_p = \frac{kT}{\mu g}, \tag{1.4}$$

where k = 1.38e-23 JK^{-1} is the Boltzmann constant and μ is the mean molecular mass of the atmosphere[4]. The pressure scale height identifies the distance over which pressure decreases by a factor of e. For the martian lower atmosphere, H_p is approximately 10.8 km, roughly a third again larger than that for the Earth's troposphere. This means that pressure decreases less rapidly with height on Mars than it does on Earth.

The composition of the well-mixed martian atmosphere (below ∼125 km altitude on average) is given in Table 1.4. Having CO_2, a condensable gas, as its primary constituent (as opposed to the non-condensable N_2, like at Earth) results in repercussions for the martian atmosphere. Perhaps most significant is that up to 30% of the atmospheric mass condenses out of the atmosphere onto the polar ice caps during solstices (see Sections 1.2.3.1, and 1.2.3.3). Huge latitudinal pressure gradients result and drive a pole to pole CO_2 flux which influences the winds throughout all layers of

[4]For the martian homosphere, μ = 43.34 daltons (*Magalhães et al.*, 1999).

Table 1.4: Average composition of the well-mixed martian atmosphere.

Percentage by volume	Constituent
95.32	CO_2
2.7	N_2
1.6	Ar
0.13	O
0.07	CO
0.03 (approximately 10 precipitable microns[5])	H_2O
Trace	NO
Trace	NO
Trace	Ne
Trace	Kr
Trace	CH_2O
Trace	Xe
30 ppb	O_3
10.5 ppb	CH_4*

the atmosphere. Large seasonal pressure swings also result (Figure 1.5).

Another significant component of the atmospheric composition is the extremely small amount of water vapor, leading to a very dry atmosphere with few clouds and a dramatically different profile of precipitation across the climate. It is worth noting that the average surface pressure of Mars is just below the triple point of water (611.73 Pa). This means that when the atmospheric temperature sinks below the freezing point of water (273.15 K), water vapor, lacking the pressure necessary to phase to liquid water, freezes directly and is deposited onto the polar caps. Likewise, when the atmosphere warms above the melting point, the water ice on the polar caps sublimates into the atmosphere as water vapor. It should be noted that the observed surface pressures have, on occasion, exceeded the triple point (e.g., VL1 and VL2 observed pressures as high as 9-10 mb, see Figure 1.5), and therefore it is possible that pure liquid water may exist on the surface for short periods, under the right circumstances. In addition it should be noted that salt in water acts as an antifreeze, permitting the

[5] 1 precipitable micron = 10^{-3} kg m^{-2}.

*Positive detection of methane at Mars is actively debated (e.g., *Smith et al.*, submitted 2011).

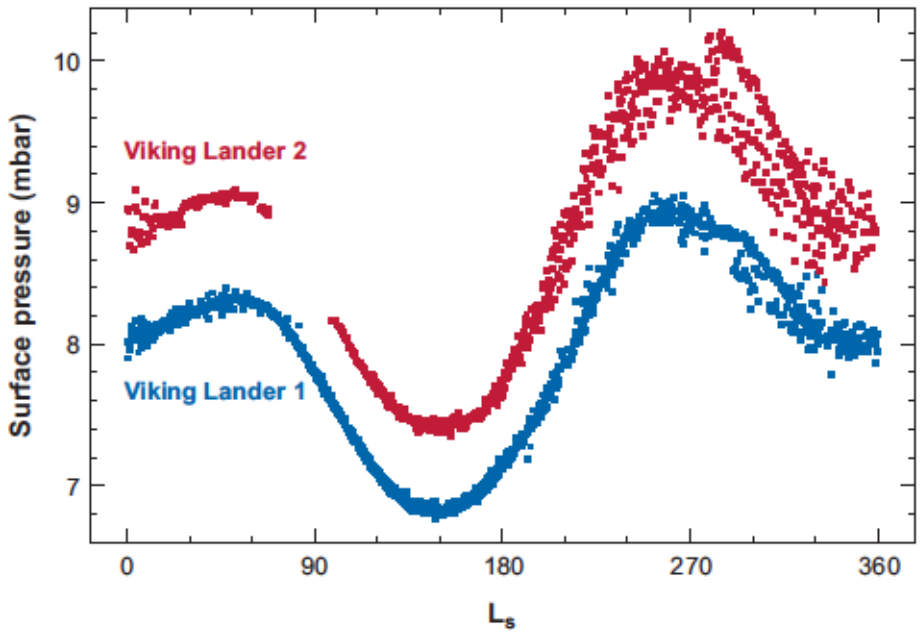

Figure 1.5: Surface pressure as a function of solar longitude, as measured by the Viking Landers. More of the atmosphere is condensed out during southern winter ($L_s \sim 150°$) because it is longer than northern winter. From *Smith* (2008), originally from *Tillman* (1988).

resultant saline solution to remain in a liquid state to temperatures below pure water's freezing point and that perchlorate salts are observed to be common at the martian poles. The first observations of such brine solutions on the surface were made in areas disturbed by the Phoenix lander (*Rennó et al.*, 2009). Subsequent studies suggest that such a saline solution may be ubiquitous in the subsurface of Mars (*Rennó and Mehta*, 2010)

The standard temperature profiles of Mars are very different from Earth (Figure 1.6). However, much like the terrestrial atmosphere, the average temperature profiles of the martian atmosphere suggests vertical regions, each hosting its own set of chemical, dynamical, and energetic processes. The lower atmosphere is that portion of the atmosphere whose primary source of heat is thermal emission from the surface and therefore, generally exhibits temperature that decreases with height. The atmospheric lapse rate is given by

$$\Gamma = -\frac{dT}{dz}, \tag{1.5}$$

and it is smaller in the lower atmosphere of Mars than the lower atmosphere of Earth (see Table 1.3).

The distinction between the lower atmosphere and the middle atmosphere is not altogether clearly defined for Mars. It is largely a matter of a change in the lapse rate. In the case of the polar night (blue curve in Figure 1.6), the boundary between the lower and middle atmosphere might be said to be the place where the lapse rate becomes positive ($\sim$ 50 km). In the case of the rest of the atmosphere, the boundary might be characterized by the change to a more gradual lapse rate (also $\sim$ 50 km). Alternatively, it might be distinguished by the top of the typical (i.e., in the absence of storms) dust layer (which also happens to be $\sim$ 50 km). Despite the lack of consensus as to the process or feature that should be used to define the boundary

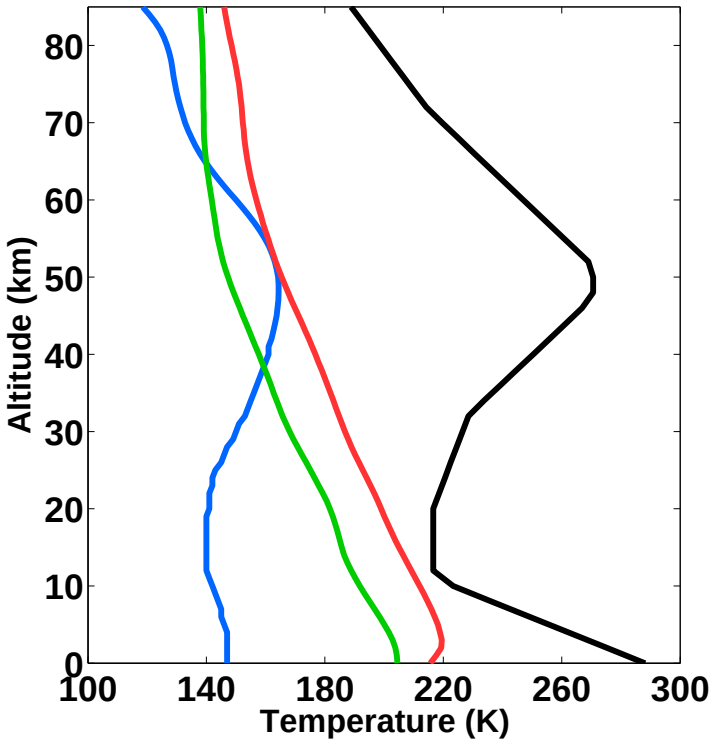

Figure 1.6: 1976 U.S. standard atmosphere (black) and martian standard atmosphere for clear (green), dusty (red), and polar night (blue) conditions. The Mars standard atmosphere data are based on observations made by the MCS instrument as reported in *Smith et al.* (submitted 2011).

between the lower and middle atmosphere, this boundary is typically associated with $\sim$ 50 km altitude. That said, a clear boundary like the tropopause on Earth is not especially constructive when conceptualizing the atmosphere of Mars. For Earth the tropopause marks the transition to the statically stable stratosphere, and hence the topmost extent of weather systems. For Mars the change in lapse rate that might be used to draw a boundary between the lower and middle atmosphere is not a change that leads to static stability. Consequently, the topmost extent of martian weather systems does not coincide with this lapse rate change. In fact, the atmosphere of Mars is characterized by large scale circulations that reach into the middle atmosphere and even the upper atmosphere, and by regional weather systems that penetrate high into the middle atmosphere (as evidenced by dust lofting up to heights above 50 km (*Smith*, 2003)).

The temperature decrease with height that occurs in the mesosphere is the result of weak solar heating, increased CO_2 vibrational cooling (at $\lambda = 15$ μm), and the absence of convection-driven heating.

The distinction between the mesosphere and the thermosphere is given by an inflection point in the temperature profile. The mesopause (the inflection point) is the coldest point in the vertical profile.

Above the mesopause lies the thermosphere, that portion of the atmosphere whose temperature rapidly increases with height. This increase in temperature with height is due to the absorption of EUV and UV solar radiation by the molecular and atomic constituents that dominate the higher altitudes.

Within the thermosphere there exists another type of boundary called the homopause. The homopause represents not a temperature or lapse rate boundary, but a composition boundary. Below the homopause, in the region called the homosphere the composition of the atmosphere is essentially well-mixed by atmospheric turbulence (i.e., large- and small-scale eddies). At the homopause (on average $\sim$ 125 km alti-

tude), molecular diffusion overtakes eddy diffusion. Above the homopause, in what is called the heterosphere, the composition of the atmosphere is stratified by molecular mass (or atomic mass, as the case may be) as each constituent of the atmosphere is governed by its own scale height such that heavier molecules (e.g., CO_2) congregate near the homopause and lighter elements (e.g., O) dominate the higher altitudes.

In the studies comprised in this thesis, we will use the terms "lower atmosphere" to refer to the region governed by convection and the top of the typical dust layer (approximately <50 km), "upper atmosphere" to refer to the heterosphere (approximately >130 km), and "middle atmosphere" to refer the layer between the two (approximately 50-130 km altitude).

For completeness' sake, it should be noted that within the middle and upper atmospheres exist still other boundaries, namely those pertaining to the ionized atmosphere. While the ionosphere is a critical component for understanding the planetary system as a whole (*Schunk and Nagy*, 2009), significant impacts upon the neutral atmosphere are generally confined to the thermosphere. The work in this thesis addresses the neutral middle atmosphere and does not consider the ionosphere, except where its treatment is a necessary component of a numerical model (e.g., Section 2.3).

1.2.2 Dynamics

1.2.2.1 Circulation

The primary source of winds in the atmosphere is differential solar heating (Figure 1.7) and the associated pressure gradients. The mean meridional circulation of the atmosphere is driven by the differential heating between the low latitudes and the poles, and takes the form of thermally driven Hadley cells. During equinoxes, a rising branch of air forms over the equator (subsolar point and area of maximum solar heating). This air rises into the middle atmosphere where it then moves poleward (one cell in each hemisphere). At high latitudes convergence occurs which results

in descending branches over both poles. Return flow from the high latitudes to the tropics occurs at low altitudes. During solstices the subsolar point moves into the summer hemisphere and so does the rising branch of the meridional cells. In the middle atmosphere the air again diverges toward the poles (one of the cells crosses the equator) where it once again converges and sinks. These thermally direct cells lead to mechanically forced Ferrel cells over the high-latitudes, in which the sinking branch of the Hadley cells forces divergence at the surface, resulting in poleward flow and rising air over the poles.

Planetary rotation also causes winds. The zonal wind, u, obeys the thermal wind relationship

$$\frac{\partial u}{\partial z} \simeq \frac{1}{H_p}\frac{\partial u}{\partial \ln p} = \frac{g}{af\theta}\frac{\partial \theta}{\partial \phi}, \tag{1.6}$$

where $f = 2\Omega\sin\phi$ is the Coriolis parameter, ϕ is latitude, and θ is the potential temperature, given by

$$\theta = T\left(\frac{p_0}{p}\right)^{\left(\frac{R}{c_p}\right)}. \tag{1.7}$$

The thermal wind relationship (Equation (1.6)) is an expression of geostrophic balance (pressure gradient force is balanced by the Coriolis force), indicating the importance of planetary rotation in generating winds. Equation (1.6) indicates that the zonal wind over mid-latitudes grows westerly (i.e., eastward) with height, generating a westerly jetstream in the middle and upper atmosphere that encircles the polar latitudes (Figure 1.7). At lower latitudes, trade winds dominate, as they do on Earth.

1.2.2.2 Waves

Mid-latitude pressure systems (cyclones and anticyclones) occur on Mars. On Earth, these pressure systems are associated with upper-level waves (troughs and ridges) that often extend to the tropopause. On Mars, such upper-level waves (also called "planetary waves") extend much higher, affecting the depth of the atmosphere.

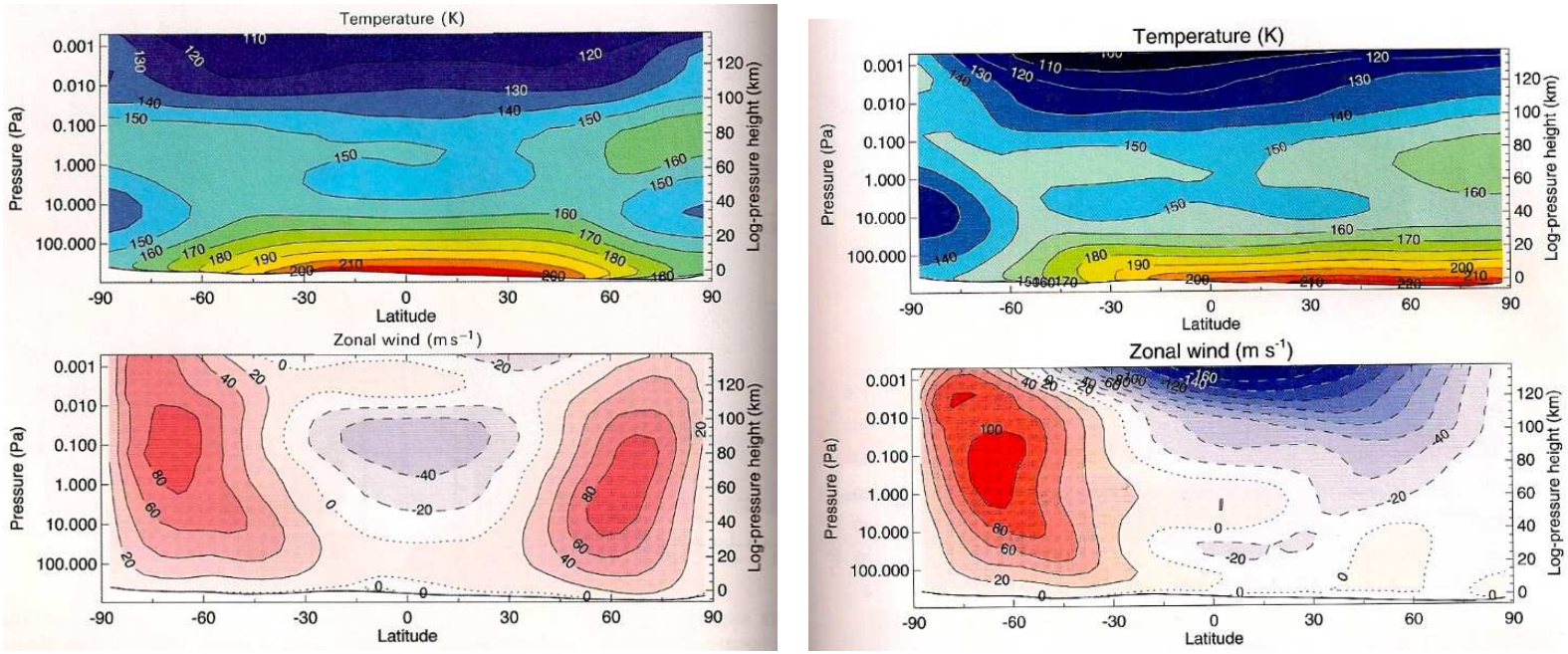

Figure 1.7: Cross-sections of the zonal-mean temperature and zonal wind simulated by the Oxford Mars GCM showing the mid-latitude westerly jets in the middle atmosphere. (a) $L_s = 0°$ equinox and (b) $L_s = 90°$ solstice. From *Read and Lewis* (2004), Figures 3.18 and 3.19.

These waves are the atmosphere's response to horizontal perturbations to the mean flow (typically resulting from baroclinic instability in the mid-latitudes, shear instability, or flow over topography). The defining characteristic of planetary waves is that their restoring force is the Coriolis force. These waves propagate horizontally and vertically. Their horizontal scale is on the order of 10^3 km.

Another form of wave that forms in the martian atmosphere is gravity waves. These are waves that result from vertical perturbations to the mean flow (typically resulting from flow over topography, convection, or shear instability) and whose restoring force is buoyancy. Gravity waves propagate horizontally and vertically. They grow with altitude and their typical vertical wavelengths are on the order of a few km. Gravity waves have significant effects on the momentum and energy budgets of the middle and upper atmosphere, where they deposit their momentum and energy (*Barnes*, 1990; *Forget et al.*, 1999; *Collins et al.*, 1997; *Fritts et al.*, 2006; *Heavens et al.*, 2010). In the case of Earth, when gravity waves break in the mesosphere, the associated momentum deposition acts as a drag on the zonal velocities and closes the mesospheric zonal jets (see Figure 1.7). Similar effects are expected at Mars (*Bougher et al.*, 2011a; *Medvedev et al.*, 2011a).

Thermal tides are gravity waves that are launched by solar heating and whose oscillation frequencies are subharmonics of a solar day. Thermal tides are generated by the harmonics of solar heating as well as topography. Like gravity waves, they propagate vertically and grow with altitude. Their typical vertical wavelengths are on the order of 10 to 10^2 km. Thermal tides have particular importance for the momentum and energy budgets of the upper and middle atmosphere, where they have been shown to create large amplitude longitudinal variability in observations of density and temperature from aerobraking accelerometry and from the Spectroscopy for the Investigation of the Characteristics of the Atmosphere of Mars (SPICAM) stellar occultation datasets (*Forbes*, 2004; *Withers et al.*, 2003b; *Withers*, 2006; *Withers*

et al., 2011). They also generate ionospheric oscillations (e.g., *Bougher et al.*, 2004).

1.2.3 Seasonal Cycles

The most important seasonal cycles of the atmosphere are those of CO_2, dust, and water.

1.2.3.1 CO_2 Cycle

The seasonal deposition of CO_2 onto the polar caps and its sublimation months later (the process responsible for large seasonal swings in surface pressure, as shown in Figure 1.5) are the consequences of the very low surface temperatures (as low as 140 K) achieved over the high latitudes during local winter. The CO_2 frost point at martian surface pressures is near 150 K. When the atmospheric temperature sinks below the frost point, CO_2 can condense to form CO_2-ice clouds which can then "snow" CO_2 ice onto the surface, or the CO_2 in the atmosphere can deposit directly onto the surface. The atmosphere constantly seeks equilibrium and thus the loss of atmospheric mass onto the cap (pressure drop) instigates a response to restore equilibrium. Meridional winds of $v \sim 0.5$ m s^{-1} flow into the winter polar region to replenish the mass lost to the cap. To conserve angular momentum, a zonal wind perturbation ("condensation flow") of $u \sim 10$ m s^{-1} develops. This does not have a significant effect on the zonal winds of the middle and upper atmosphere (where u>100 m s^{-1}), but its relative importance is greater near the surface. Since CO_2 is the major constituent of the atmosphere, it is plentifully available for condensation, and deposition continues (seasonal cap depth can reach up to 1 m thick) until the temperature rises above the frost point in the spring time.

The seasonal condensation of the major atmospheric constituent affects the local composition of the atmosphere above the pole as well. Noncondensable gases are left behind as CO_2 condenses out of the atmosphere and mixing with lower-latitude air

does not completely restore their mixing ratios locally. Argon and molecular nitrogen enhancements from a factor of 1.5 to a factor of 6 have been observed and modeled over the seasonal polar caps (*Sprague et al.*, 2004, 2007; *Nelli et al.*, 2007).

1.2.3.2 Dust Cycle

Dust in suspension in the martian atmosphere is radiatively active (e.g., *Toon et al.*, 1977; *Pollack et al.*, 1979). It absorbs solar radiation and re-emits it at longer wavelengths, significantly warming the atmosphere. This dust heating intensifies the mean meridional circulation (*Haberle et al.*, 1982; *Murphy et al.*, 1995). It also leads to a thermal expansion of the atmosphere, whereby surfaces of constant pressure are lifted to higher altitudes (*Bougher et al.*, 1997, 1999a). While the airborne dust itself typically does not extend much above 50-60 km in altitude, the thermal expansion it produces is felt as high as the thermosphere (*Bell et al.*, 2007). The seasonal cycle of atmospheric dust loading is such that the aphelion season (L_s = 0 - 180°) is typically and repeatedly "clear" (the atmosphere always has a small amount of background dust present) from one year to the next (*Smith*, 2003). The perihelion season (L_s = 180-360°), on the other hand, experiences regional and sometimes global dust storms and exhibits wide variability from one year to the next in terms of timing, duration, latitudinal extent, and strength of dust storms (dust opacity) (e.g., Figure 2.3). Regional dust storms are more common in the southern hemisphere and global storms often originate there as well. This is because the perihelion season, when such events occur, is near southern summer and therefore atmospheric heating (and lifting) is stronger in the southern hemisphere during this season. Dust devils are also part of the martian dust cycle. These vortices of dust are thought to be much larger (frequently 100 m to 1 km across and 5 km high) than dust devils on Earth and may contribute significantly to the supply of suspended dust (*Thomas and Gierasch*, 1985; *Rennó et al.*, 2004).

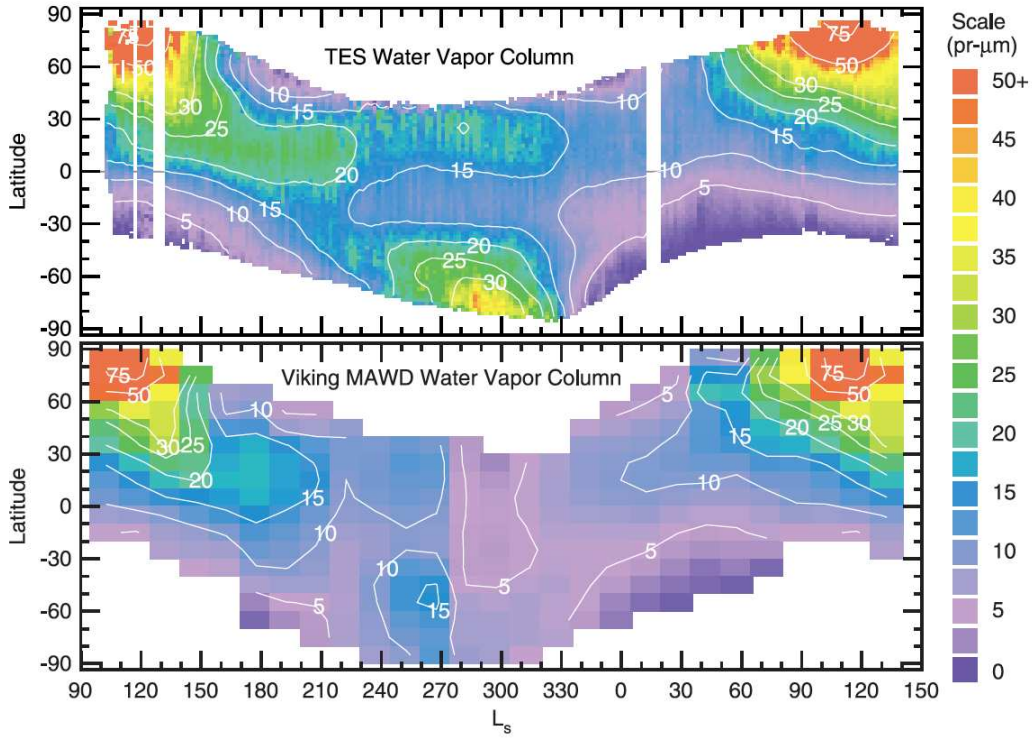

Figure 1.8: Water vapor column abundance as a function of latitude and season from TES (*Smith*, 2002) and Viking Mars Atmospheric Water Detector (*Jakosky and Farmer*, 1982). Figure from *Smith* (2002).

1.2.3.3 Water Cycle

Though the present-day martian atmosphere is very dry, it does experience a seasonal water cycle. The principal source of water for the atmosphere is the north polar water ice cap. As mentioned in Section 1.1 the northern CO_2 seasonal cap completely sublimes during northern summer, leaving the water ice cap below exposed to the atmosphere and able to sublime. This leads to a seasonal spike in atmospheric water vapor over the northern high latitudes during early northern summer that spreads equatorward via atmospheric transport as northern fall progresses (Figure 1.8) (*Smith*, 2002).

The south polar water ice cap is believed to act as a "cold trap" (permanent sink) for atmospheric water vapor rather than a source (*Kieffer*, 1979). Since the southern CO_2 ice cap does not completely sublime away during local summer, the

water ice below is not exposed to be able to sublimate. Moreover, since the surface temperature of the south cap remains close to the CO_2 frost point, which is colder than the H_2O frost point, water vapor that is transported to the south polar region immediately freezes onto the cap (*Kieffer*, 1979). The source of the secondary water vapor maximum that occurs in the souther mid-latitudes during southern summer is likely due to sublimation of water adsorbed into the regolith (*Jakosky and Farmer*, 1982; *Smith*, 2002).

When atmospheric temperatures fall below the condensation point of water, water ice clouds form in the martian atmosphere. This repeatedly occurs over tropical latitudes during the aphelion season (called the "aphelion cloud belt"). It also occurs commonly near the edge of the polar cap during local winters (*Smith*, 2003).

1.3 Upper Atmosphere

There are far fewer observations for the neutral upper atmosphere of Mars than for the lower atmosphere. Still, the observations available characterize the temperature and mass density of this region and modeling efforts have provided insight into the wind structure.

1.3.1 Temperature

The temperature of the upper atmosphere is governed by the balance achieved between five heating and cooling terms: absorption of solar EUV and UV radiation primarily by CO_2 and atomic O (heating), molecular conduction (cooling), horizontal advection (heating and cooling), adiabatic motions (heating and cooling), and 15 μm IR emission by CO_2 (cooling) (*Bougher et al.*, 1999a). Since the main source of heating is absorption of solar EUV and UV (portions of the solar spectrum that vary markedly throughout the solar cycle), the temperature of the upper atmosphere is closely tied to the solar cycle, as well as the diurnal cycle, as observed by aerobraking accelerometry

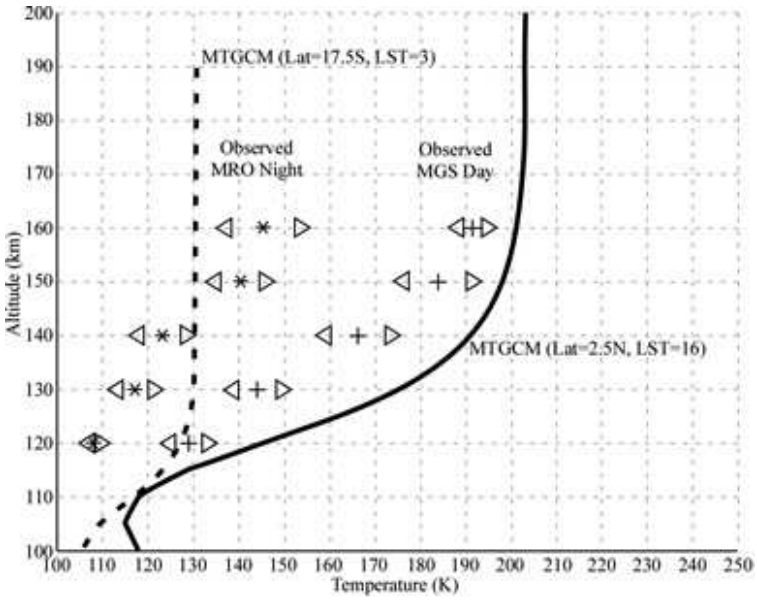

Figure 1.9: Upper atmosphere temperature profiles from accelerometer measurements. Stars are average nightside temperatures from MRO. Pluses are average dayside temperatures from MGS. Curves are the corresponding simulations from the MTGCM. From *Keating et al.* (2008).

(Figure 1.9). Upper atmosphere temperatures also exhibit strong northern winter polar warming (PW) and modest to weak southern winter PW (Figure 1.10).

1.3.2 Density

The mass density of the upper atmosphere is fairly stable over periods of weeks, as evidenced by densities calculated from accelerometer measurements (Figure 1.11). As mentioned in Section 1.2.2.2, the upper atmosphere exhibits longitudinal variations in mass density that are caused by vertically propagating thermal tides.

1.3.3 Waves

The winds in the upper atmosphere are heavily influenced by upward propagating gravity waves, planetary waves, and thermal tides, as well as by dust-heating and the subsequent inflation of the atmosphere. All of these influences come from the lower atmosphere and are translated through, and sometimes altered by, the middle

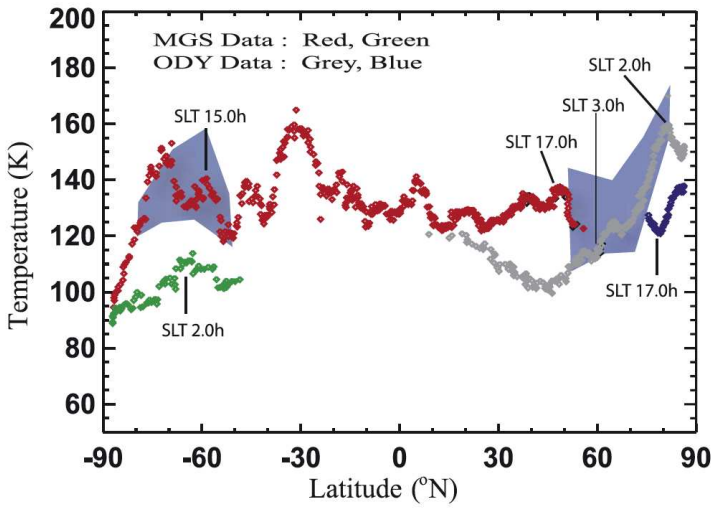

Figure 1.10: 120-km temperatures from accelerometer densities. Dynamical winter PW in the northern hemisphere is approximately 40-60 K in magnitude while that in the southern hemisphere is approximately 10-20 K. Blue shading indicates the range of nightside temperatures simulated by the MGCM-MTGCM. From *Bougher et al.* (2006).

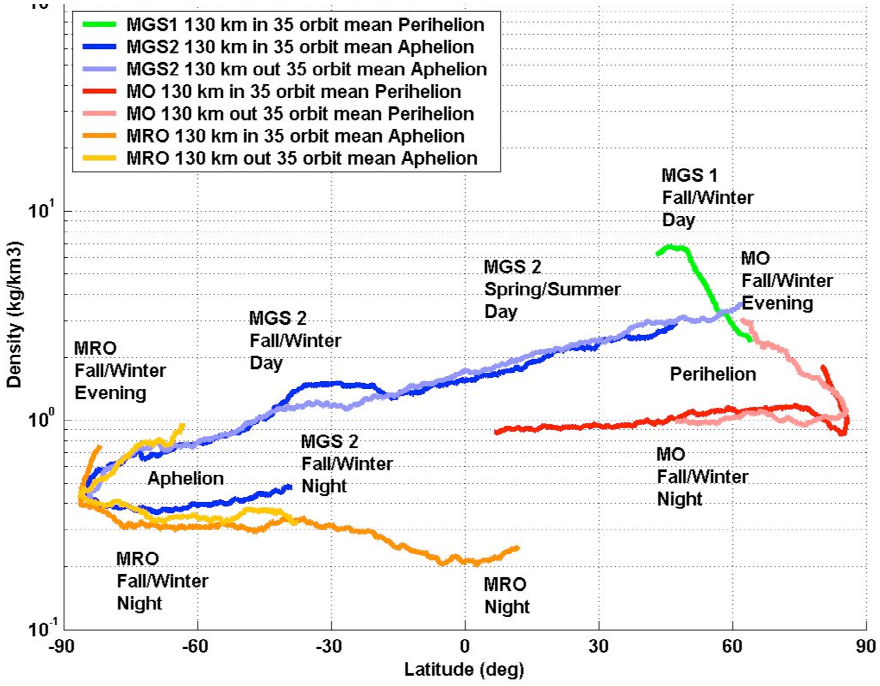

Figure 1.11: 130-km mass density from accelerometers. The inbound and outbound passes exhibit relatively consistent densities despite being separated by periods of several weeks, indicating that the mass density of the upper atmosphere is stable on periods of weeks. From *Keating et al.* (2006).

atmosphere. This coupling means that a good understanding of the structure and dynamics of the middle atmosphere and the factors that affect it are necessary to achieve a good understanding of the upper atmosphere.

1.4 Middle Atmosphere

As with the upper atmosphere, previous spacecraft and ground-based measurements of the middle atmosphere have been limited spatially and temporally. Despite this limitation, a clearer picture of this highly-coupled portion of the atmosphere is emerging. This section summarizes the state of observational knowledge of the middle atmosphere prior to the work presented later in this thesis.

1.4.1 Temperature

The temperature of the atmosphere up to approximately 40 km altitude was first observed by the Mariner 9 spacecraft's Infrared Radiometer (IRR) instrument, while the temperature up to approximately 60 km was first observed by Mariner 9's Infrared Interferometer Spectrometer (IRIS) instrument. IRR observed a 30-km temperature of ~ 240 K, above which a sharp lapse rate brought the temperature to 200 K at ~ 40 km. This observation took place during the global dust storm of 1971. IRIS observed temperatures up to approximately 60 km altitude during the global dust storm of 1971 and found that temperatures over the north-polar region were approximately isothermal at $T = 180$ K between 30 and 60 km (*Jakosky and Martin*, 1987).

The next temperature observations of the middle atmosphere came from the Viking Landers during their entry, descent, and landing (EDL). Viking Lander 1 and Viking Lander 2 observed temperatures profiles very similar to one another, despite their different landing locations (northern tropical-latitudes during mid-afternoon versus northern mid-latitudes during night). Temperature in the 30-130 km altitude region ranged from ~ 160 K (near 30 km) to ~ 115 K (near 115-125 km) (see Fig-

ure 1.15).

After Viking, the next temperature observations came from ground-based heterodyne spectroscopy. These measurements were taken during mid-northern summer and were averaged over the 50-85 km altitude range and spread across the disk of the planet. These observations revealed for the first time dynamical PW in the middle atmosphere of Mars. The winter pole-to-summer pole temperature gradient was 0.4 - 0.9 K per degree of latitude (*Deming et al.*, 1986).

Middle atmosphere temperatures up to 80 km altitude were retrieved from global scale millimeter wave observations (of CO) from a ground-based telescope in 1993. These profiles generally gave temperatures that decreased with height from $\sim$ 170 K at 30 km to $\sim$ 142 K at 80 km (*Théodore et al.*, 1993).

MPF measured atmospheric temperature during its EDL. The resulting middle-atmosphere temperature profile found a 30-km temperature close to 170 K, above which the temperature decreased to a mesopause at 82 km of $\sim$ 90 K (well below the CO_2 condensation point). Above the mesopause the temperature increased with height to $\sim$ 120 K around 120-130 km.

Mars Global Surveyor (MGS)-Thermal Emission Spectrometer (TES) provided the first systematic observations of middle-atmosphere temperatures up to $\sim$ 65 km (nadir and limb mode). Analyses of this dataset identified, for the first time, seasonal and interannual variations in the zonal mean thermal structure of the atmosphere (below 65 km) (*Smith*, 2004). They found that the atmosphere exhibited two seasonal modes: a warm, dusty, and highly variable perihelion season and a cool, clear, and highly repeatable aphelion season. They also found evidence of PW in the middle atmosphere at heights above $\sim$ 30 km during northern winter, southern winter, and equinoxes (*Smith*, 2008).

The most recent observations of the middle-atmosphere temperature structure have come from spacecraft currently orbiting Mars, namely Mars Express (MEX)

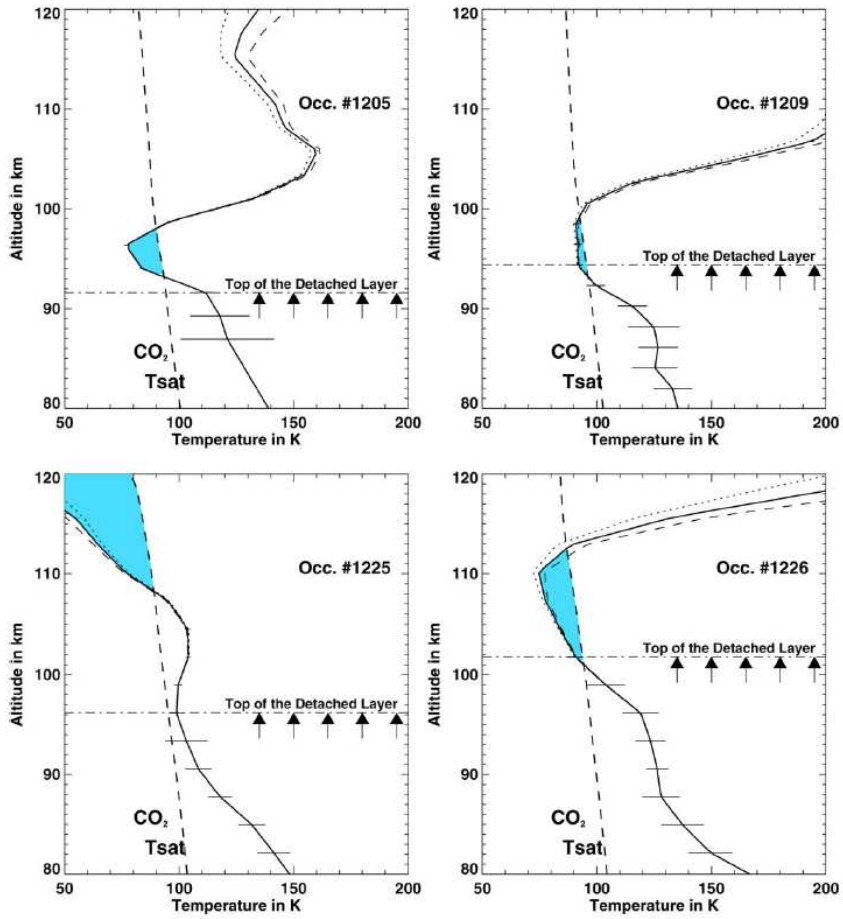

Figure 1.12: Temperature profiles from SPICAM. Dashed and dotted profiles show the uncertainty in the retrievals. Blue shading highlights regions with temperature below the CO_2 condensation point. From *Montmessin et al.* (2006).

(SPICAM instrument) and Mars Reconnaissance Orbiter (MRO) (Mars Climate Sounder (MCS) instrument). SPICAM stellar-occultation temperatures have shed light on the vertical and seasonal structure of nightside temperature in the 70-130 km altitude range. *Montmessin et al.* (2006) and *Forget et al.* (2009) identified mesopause temperatures below the CO_2 frost-point, primarily in the southern winter tropics (Figure 1.12), and *Forget et al.* (2009) found moderate ($\sim$ 20-30 K) nightside PW from $p = 1 \times 10^{-1}$ to 1×10^{-2} Pa during southern winter (L_s = 90-120°).

MRO-MCS temperatures have revealed the zonal mean thermal structure and its variability from near the surface to 80-90 km altitude. *McCleese et al.* (2010)

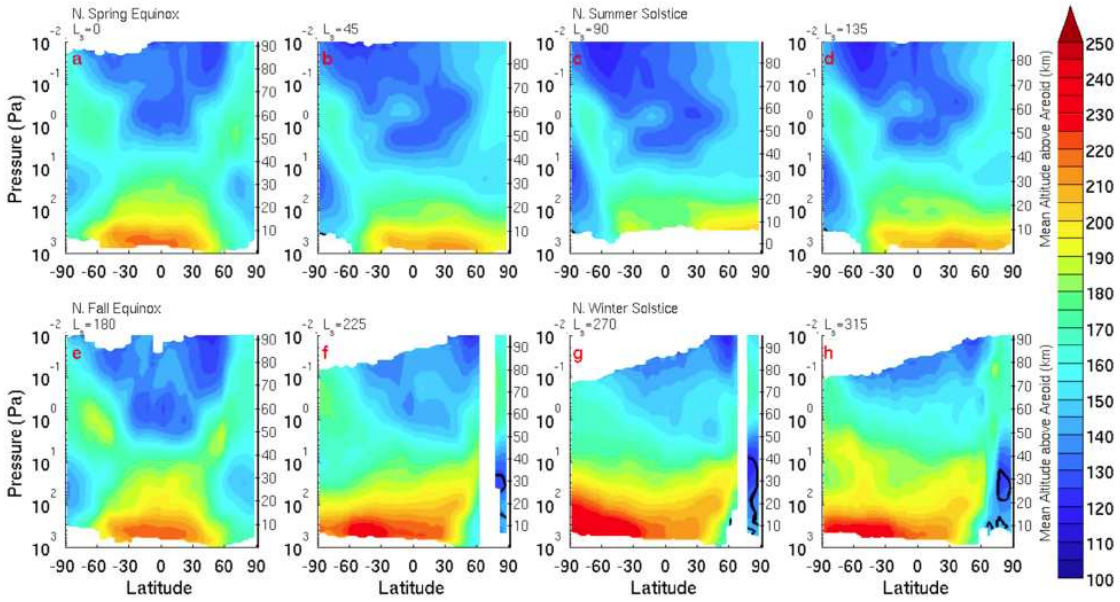

Figure 1.13: Zonal average nightside temperatures from MCS during MY 29. From *McCleese et al.* (2010).

found two modes of thermal structure: a symmetric equinoctial structure and an asymmetric solstitial structure (Figure 1.13). *McCleese et al.* (2008a) and *McCleese et al.* (2010) identified PW during solstices and *McCleese et al.* (2010) identified PW during equinoxes. *Lee et al.* (2009) examined thermal tides (Figure 1.14) and found most diurnal variations in temperature were associated with the diurnal thermal tide. *Heavens et al.* (2010) investigated dry convective instabilities in the middle-atmosphere and found them to be widespread across the planet and largest over the northern winter extratropics. Finally, *Heavens et al.* (2011a) studied the kinematic coupling between the mean meridional circulation of the lower and middle atmosphere.

1.4.2 Density

VL1 measured atmospheric density during its EDL and found a profile that decreased exponentially with height from $\sim 10^{-3}$ kg m^{-3} at 30 km to $\sim 10^{-8}$ kg m^{-3} at 120 km. MPF also measured atmospheric density during its EDL and found similar

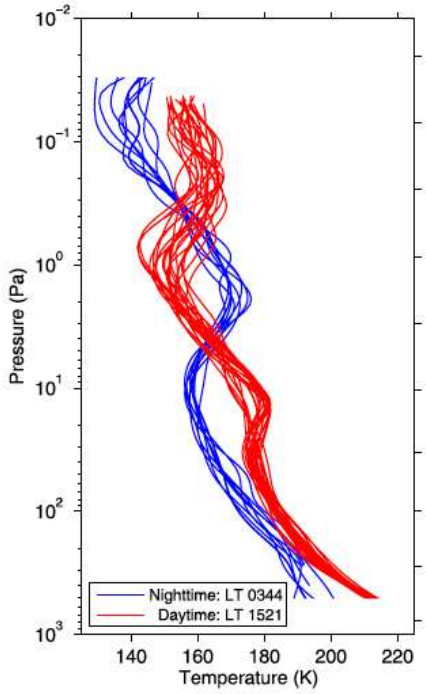

Figure 1.14: MCS temperature profiles from late northern summer, mid-northern latitudes, highlighting the presence of thermal tides. Red curves are daytime observations and blue curves are nighttime observations. From *Lee et al.* (2009).

values to those of VL1. One noteworthy difference, however, was a kink in the MPF profile around 80 km, above which the densities were approximately half an order of magnitude smaller than the VL1 values (*Schofield et al.*, 1997).

1.4.3 Winds

50- to 90-km winds have been retrieved from ground-based infrared heterodyne spectroscopy of CO_2 (e.g., *Sonnabend et al.*, 2006). Such retrievals have revealed strong westerly jets over the mid-latitudes of the winter hemisphere.

1.4.4 Waves

Oscillations in the VL1 and VL2 temperature profiles were the first evidence of thermal tides and gravity waves propagating up into the middle atmosphere (see Figure 1.15). Ground-based temperature observations and high-altitude TES temperature observations of PW in the middle atmosphere provide support for the theory that gravity waves propagate through, and sometimes break in, the middle atmosphere and affect the global winds, thereby inducing the dynamical PW observed in these datasets.

1.4.5 Dust

Finally, TES-limb dust observations determined that atmospheric dust can reach high into the middle atmosphere (up to 50-60 km altitude) during periods of high opacities (M. Smith, personal communication, 2009).

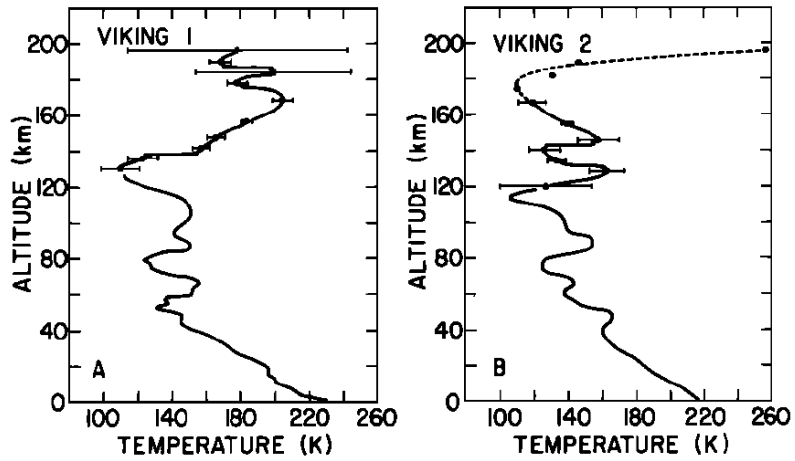

Figure 1.15: Temperature profiles from the Viking Landers. Temperatures above 120 km are obtained from an analysis of neutral density scale heights (*Nier and McElroy*, 1977) while those below 120 km are from entry science data (*Seiff and Kirk*, 1977). Figure from *Nier and McElroy* (1977).

1.5 Motivation For This Thesis

1.5.1 Why Continue to Study the Atmosphere of Mars?

As the previous sections have shown, much has already been learned about the atmosphere of Mars. Why should we continue in this endeavor? What makes the martian atmosphere interesting and compelling from a scientific point of view?

First, study of the martian atmosphere is compelling because it represents a laboratory in which we can better understand our home planet's atmosphere, its history, and possibly its fate. Comparative planetary science is a bit like an experiment in reverse, like walking into a laboratory where someone else developed the experiment and forgot to leave a description of the experimental set-up. Each planet is an experiment on a global scale that has controls and variables both similar to and different from those involved in the experiment of Earth. We have no (or little) control over the controls and variables involved in these planetary experiments, yet we know the experiments are governed by the same fundamental physical and chemical laws. By determining the important parameters for the martian experiment and their values,

and determining if they are similar to or different from those for the Earth experiment, we can glean understanding of the martian system that may improve our understanding of the Earth system or other systems. Gradually, we piece together an understanding of how these worlds operate. The Earth is but one experiment in a universe full of experiments. Surely much remains to be learned by observing and coming to understand the other experiments being run.

A second reason we study the atmosphere of Mars is to learn about how we can utilize the planet. We are interested in what we can learn about the planet and how we can ensure the safety of the craft we send there to deliver us clues to the scientific mysteries we are attempting to de-mystify. We may also be interested in using the planet as a human base and the mean state and variability of the atmosphere are constraints on the viability of doing so.

Finally, studying the atmosphere of Mars is interesting for its prospect of indigenous life. If life were to be found somewhere other than Earth, it would lead to many lines of scientific (biological and astronomical) as well as philosophical and theological inquiry that may alter the way humans view themselves. While such questions are far outside the scope of this thesis, they do lend motivation for seeking to understand the entire Mars system, including the atmosphere.

1.5.2 Why Continue to Study the Middle Atmosphere?

As indicated in the previous sections, the middle atmosphere is the interface between the lower and the upper atmospheres. As was the case for Earth, this region has been relatively inaccessible to measurements and consequently it was notoriously understudied, earning the nickname "The Ignorosphere." Paralleling the development of terrestrial atmospheric science, study of the martian middle atmosphere has only developed recently in response to the recognition of its importance to understanding the upper atmosphere and, to a lesser extent, the lower atmosphere.

The martian middle atmosphere is important for several reasons. It is an interface region, affected by the upward propagating planetary waves, gravity waves, and thermal tides generated in the lower atmosphere, the dust-heating driven and seasonal expansion and contraction of the lower atmosphere, and the downward molecular conduction of thermospheric energy. It is connected to both the lower atmosphere and the upper atmosphere through the deep global mean meridional circulation. It is the region across which information is passed from the convectively driven, dust-heating dominated lower atmosphere to the solar UV and EUV dominated upper atmosphere. It experiences thermal, dynamical, and chemical processes that are unique to these altitudes (and in some cases, unique to this planet), and which must be understood in order to develop a full understanding of the dynamical coupling between the lower and upper atmospheres.

The upper portion of the middle atmosphere is also of great importance for aerobraking missions. As spacecraft use the atmosphere to brake their speeds and circularize their orbits, they pass through the lower thermosphere ($\sim$ 100-130 km). Accurate predictions of the structure and variability of this region are therefore of vital importance for proper aerobraking, as well as for the safety of the spacecraft. In addition, the 2013 NASA mission to Mars, Mars Atmosphere and Volatile Evolution (MAVEN), is slated to conduct five "deep dip" campaigns in which the spacecraft will be flown down to aerobraking altitudes to collect *in-situ* measurements. Accurate understanding of this region is critical to the safety of the MAVEN spacecraft during these campaigns.

Finally, simulations of the middle atmosphere provide the lower boundary conditions required for properly calculating the solar wind interaction with Mars. Validation of general circulation model (GCM) calculations of middle atmosphere fields is therefore of considerable importance for studies of atmospheric escape and the long term evolution of the atmosphere.

Recently, a growing amount of data has been collected from the middle atmosphere and is now available for study. In particular, density and temperature profiles from MEX/SPICAM stellar occultations, temperature profiles from MRO/MCS, and temperature data from the accelerometers onboard MGS, Mars Odyssey (ODY), and MRO are now available for analysis. Especially exciting are the SPICAM and MCS profiles, which provide, for the first time, systematic observations of the middle atmosphere, allowing for the climatological characterization of this region found in this thesis.

1.6 Roadmap For This Dissertation

The objective of this thesis is to advance the understanding of the structure and dynamics of the middle atmosphere of Mars. In Chapter II we characterize the nightside density and thermal structure and variability observed by SPICAM in the 70-130 km altitude region, including the location and magnitude of the mesopause. We also validate the Mars General Circulation Model (MGCM)-Mars Thermosphere General Circulation Model (MTGCM) framework in this altitude region and use this GCM to investigate the importance of lower atmosphere dust loading for this previously unconstrained portion of the atmosphere and the character of its heat balance. In Chapter III we introduce a metric for quantifying dynamical PW in the middle atmosphere, characterize the PW observed in the available spacecraft datasets and provide quantitative constraints for GCM middle atmosphere calculations. In Chapter IV we investigate the relative importance of dust loading and gravity wave momentum deposition in producing the dynamical PW observed in Chapter III. Finally, in Chapter V we summarize the unique contributions of this research and suggest directions for future work in these areas.

CHAPTER II

A Characterization of the Density and Thermal Structure of the Middle Atmosphere at Mars

2.1 Context and Objectives

Until 2006, the martian atmosphere above 65 km truly was an ignorosphere, with no observations aside from some ground based observations and a small number of entry profiles. In 2006 this changed, with the entry into orbit of the European MEX mission. This orbiter carried the SPICAM instrument (see Section 2.2), which provided the first systematic observations of the middle atmosphere above 65 km. *Forget et al.* (2009) presented and analyzed the SPICAM dataset, using the Laboratoire de Météorologie Dynamique (LMD) GCM to aid their interpretation of the data. Discrepancies were shown to exist between the SPICAM-observed density and the LMD GCM calculations, particularly in the season leading up to perihelion (L_s = 140°-200°). The densities calculated by the LMD GCM for this season were significantly smaller than the values observed by SPICAM. *Forget et al.* (2009) proposed that this was due to an atypical dust event observed during this season of MY 27 (see footnote 2 on page 3 for a description of the MY convention) by the Mars Exploration Rovers (MER) Mini-TES instruments (*Smith et al.*, 2006). They found that the density structure of the middle atmosphere is intimately tied to lower atmosphere

conditions, particularly dust loads, in agreement with earlier findings for the thermosphere (*Bell et al.*, 2007). Another, more surprising, finding was that the middle atmosphere observed by SPICAM was colder than anticipated from previous *in-situ* observations (e.g., VL1 and 2 and MPF) and model simulations (e.g., *Bougher et al.*, 2006). Significant discrepancies between the observed and simulated temperature fields suggested that the thermal balances underlying the LMD GCM temperatures needed refinement.

Our first aim here is to build upon the analysis done by *Forget et al.* (2009) by developing a quantitative characterization of the vertical structure and seasonal variability of density and temperature between 80 and 130 km. SPICAM provides the most comprehensive dataset to-date for this vertical region of Mars's atmosphere, and as such, invites a more complete climatology of this region than has previously been possible. Our second aim is to use the SPICAM dataset to test the MGCM-MTGCM: (a) near the coupling boundary (1.32 μbar, corresponding roughly to 60-80 km altitude), (b) near the mesopause (90-110 km altitude), and (c) near the homopause ($\sim$ 125 km altitude). Our third aim is to use the tested model to further investigate the extent to which the middle atmosphere is sensitive to lower atmospheric dust conditions. Interpreting the data with this additional modeling framework may illuminate other possible explanations for the discrepancy discussed by *Forget et al.* (2009) between the observed densities and those calculated with the LMD GCM. Our fourth and final aim is to perform an inter-model comparison between the MGCM-MTGCM and the LMD GCM to examine the consequences arising from the different IR-heating and cooling schemes employed in these two codes. A thorough inter-model comparison is a large undertaking that will be reserved for a future study; however we present and discuss preliminary comparisons in this chapter.

In Sections 2.2 and 2.3 we describe the details of the MEX-SPICAM dataset and the MGCM-MTGCM modeling framework, respectively. In Section 2.4 we discus the

suspended dust record and its relevance to the structure of the middle atmosphere. We describe in Section 2.5 the method we use to interpret the SPICAM data and test the MGCM-MTGCM. In Section 2.6 we present the results of the data analysis and model validation, followed by a discussion of their implications in Section 2.7.

2.2 SPICAM Dataset

The SPICAM instrument is a dual UV-IR spectrometer that performs stellar occultations in the 110-310 nm (UV) and 1-1.7 μm (near-IR) bands (*Quémerais et al.*, 2006). Neutral density profiles are extracted from the UV occultations for altitudes of 50-140 km at a vertical resolution of 1-2 km (*Quémerais et al.*, 2006; *Bertaux et al.*, 2006). The density retrievals are reliable down to altitudes of 60 km (*Forget et al.*, 2009). Below this level, uncertainties, such as extinction by dust, diminish confidence in the retrievals (*Quémerais et al.*, 2006). *Forget et al.* (2009) assume a temperature at the top of the density profile to derive neutral temperature profiles from the computed density scale heights. Since the top temperature is not known and must be assumed, they calculate three temperature profiles for each density profile, assuming top temperatures of 100 K, 175 K, and 250 K (Figure 2.1). We choose to utilize the profiles that assume a top temperature of 175 K, as this falls near the middle of values previously observed (*Seiff and Kirk*, 1977; *Magalhães et al.*, 1999) and simulated (*Bougher et al.*, 1999a, 2006), though the computed temperature profile at $p > 1\text{x}10^{-4}$ Pa (altitudes below ~120 km) was found to be insensitive to the assumed top temperature (*Forget et al.*, 2009). Temperatures at $p > 1$ x 10^{-1} Pa (altitudes below $\sim$ 70 km) are over-estimated due to dust (*Forget et al.*, 2009). Therefore, we consider temperature profiles between 70-140 km with the caveat that the data extending from 120-140 km is sensitive to the assumed top boundary temperature. The vertical resolution of the temperature profiles is 1-2 km with uncertainties on the order of 3-15 K (smaller errors at 120 km altitude, larger errors at 70 km altitude)

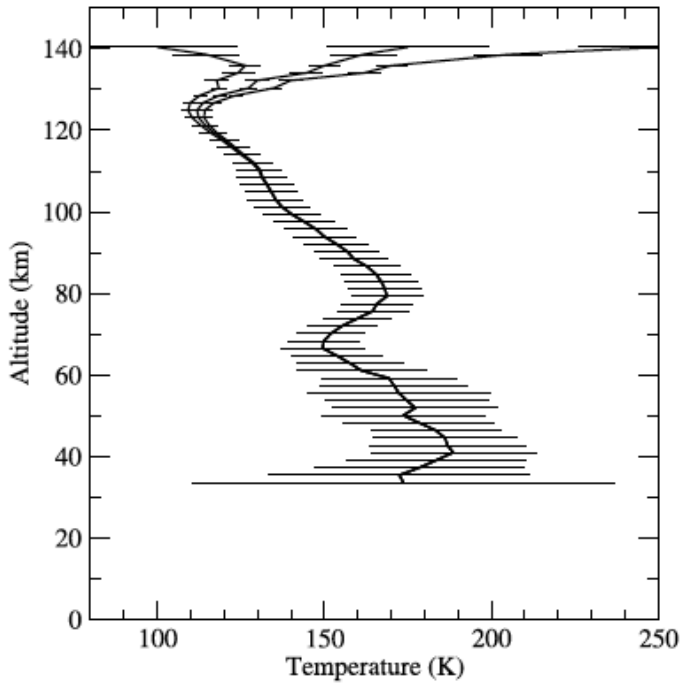

Figure 2.1: Example of a temperature profile derived from SPICAM observations. Error bars show the total uncertainty due to instrumental and retrieval errors as well as the uncertainty in CO_2 cross section. Three profiles are derived with top temperatures of 100, 175, and 250 K. From *Forget et al.* (2009).

(*Forget et al.*, 2009).

MEX arrived at Mars and began observing the martian atmosphere on 23 December 2003 (Mars Year (MY) 26, $L_s = 353°$). In its first martian year of operations, MY 27, SPICAM accumulated 616 profiles (*Forget et al.*, 2009). Due to the non-uniform distribution of UV stars across the sky (*Quémerais et al.*, 2006), most of SPICAM's observations are of the fall and winter hemispheres (Figure 2.2b). In addition, occultations were preferentially performed on the nightside (Figure 2.2c) so as to avoid contamination of the star's spectrum by scattered and reflected solar light (*Forget et al.*, 2009).

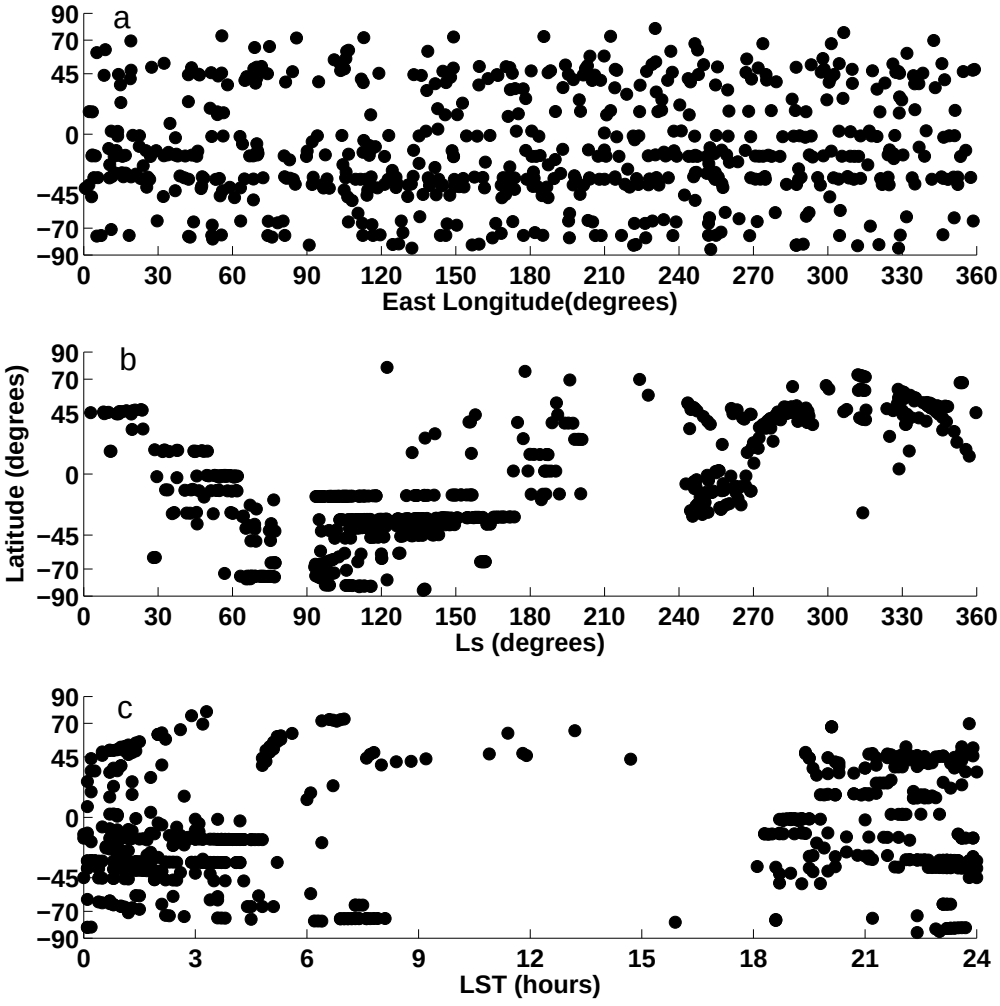

Figure 2.2: Horizontal (a), seasonal (b), and local time (c) distribution of SPICAM temperatures.

2.3 MGCM-MTGCM Framework

The MGCM-MTGCM is a coupled lower atmosphere-upper atmosphere model consisting of the Michigan MTGCM from $\sim$ 60-80 km to 300 km altitude and the NASA Ames MGCM from the surface to $\sim$ 60-80 km altitude. The MTGCM itself consists of a finite-difference primitive-equation dynamical core and physics routines and parameterizations that are appropriate to the martian environment. It is based on the National Center for Atmospheric Research (NCAR) terrestrial Thermosphere General Circulation Model (TGCM) and was first adapted for Mars studies by *Bougher et al.* (1988). It self-consistently solves for time-dependent neutral temperatures, neutral, ion, and electron densities, and three component neutral winds on 33-pressure levels above 1.32-μbar (corresponding to $\sim$ 70-300 km altitude), at a 5° latitude x 5° longitude grid resolution (*Bougher et al.*, 2004, 2006, 2008). A fast non-local thermodynamic equilibrium (nLTE) 15-μm cooling scheme is implemented in the code, along with corresponding nLTE near-IR heating rates (*Bougher et al.*, 2006). These improvements are based upon detailed one-dimensional nLTE model calculations for the martian upper atmosphere (*López-Valverde et al.*, 1998).

In addition to the neutral atmosphere, the MTGCM calculates a detailed photochemical ionosphere which captures the major ions (O_2^+, CO_2^+, O^+, and NO^+) below $\sim$ 180 km altitude (*Bougher et al.*, 2004). The inclusion of this ionosphere is critical to the self-consistent simulation of dayside atomic O abundances above $\sim$100 km. This self-consistent simulation of O is necessary because the abundance of O directly impacts the CO_2 15-μm cooling rate, yet currently there exist no direct measurements of the abundance O for the martian upper atmosphere. Thermospheric winds are known to transport O atoms from their dayside source region to the nightside and polar latitudes (*Bougher et al.*, 1999a, 2000), however O abundances have only been inferred from UV airglow measurements (*Stewart et al.*, 1992; *Huestis et al.*, 2008) and ion density measurements (*Hanson et al.*, 1977). These optically thick O

emissions are used by detailed radiative transfer models to derive the distribution of O abundances. However, the generally low abundance of O at Mars (compared to Venus and Earth) makes this modeling process difficult and subject to uncertainties. The resulting uncertainties in the Mars O abundances directly affect the simulation of the CO_2 15-μm cooling rates in the Mars dayside and nightside upper atmospheres (*Huestis et al.*, 2008).

Every 2 minutes the MTGCM receives lower boundary input at the 1.32-μbar pressure level from the MGCM code (*Haberle et al.*, 1999). The MGCM passes key prognostic (temperatures, zonal and meridional winds) and diagnostic (geopotential height) fields upward to the MTGCM at every MTGCM-grid point. This coupling allows upward-propagating tides to enter the MTGCM's simulated atmosphere. It also allows the simulated thermosphere to experience the effects of the thermal expansion and contraction of the lower atmosphere that occurs with dust storm events and with the passage of the seasons (*Bougher et al.*, 2004, 2006; *Bell et al.*, 2007). No downward coupling from the MTGCM to the MGCM is activated. However, the focus of this chapter is the structure and dynamics of the middle-to-upper atmosphere and the factors influencing these conditions. An upward coupling between the MGCM and MTGCM is necessary to reproduce these conditions, while a downward coupling has only a minor influence (*Bougher et al.*, 2008).

The MGCM is another finite-difference primitive-equation model with terrestrial heritage. It is based on the University of California, Los Angeles (UCLA) terrestrial GCM and was the first GCM adapted for Mars studies (*Leovy and Mintz*, 1969). The MGCM employs the terrain following "sigma" (normalized pressure) coordinate in the vertical, in which 26-30 model layers extend to an altitude of $\sim$ 90 km ($\sim$ 0.05 μbar) above the reference 'areoid' defined by MGS-Mars Orbiter Laser Altimeter (MOLA) (1° x 1°) data (*Smith and Zuber*, 1996) (see Figure 1.3). It runs on a 5° latitude x 5° longitude Arakawa C-grid (*Suarez and Takacs*, 1995). Recent improvements to the

treatment of dust within the model allows it to now be run with active dust lifting (*Kahre et al.*, 2006, 2008). This includes both surface stress lifting (*Newman et al.*, 2005a; *Haberle et al.*, 2003) and dust devil-dependent lifting (*Newman et al.*, 2005b). This also includes particle-size dependent dust sedimentation, according to the Stokes-Cunningham relation (*Pruppacher and Klett*, 2000). Another recent improvement to the physics of the model is the inclusion of suspended-dust radiative heating within the correlated-k radiative transfer routine, which covers 12 spectral bands tailored for the Mars CO_2-water vapor atmosphere covering the range of 0.3 to 250 μm.

Adjustable parameters in the MGCM-MTGCM that are important for middle-atmosphere calculations are the solar flux index and the prescription of dust in the lower atmosphere. In the present study we employ a moderate solar flux index (see Section 2.7) for all simulations. The lower atmosphere dust prescriptions used in this study are discussed in Section 2.4.

2.4 Suspended Dust History

It is well documented that the dust opacity within Mars's atmosphere undergoes strong seasonal variability as well as interannual variations (e.g., *Liu et al.*, 2003; *Smith*, 2004; *Kahre et al.*, 2008). The dust opacity during the aphelion season ($L_s \sim 90°$) is relatively consistent from one martian year to the next (Figure 2.3). In contrast, the dust opacity during the perihelion season ($L_s \sim 240°$-$270°$) displays wide interannual variability in terms of: (1) time evolution of the dust opacity, (2) number, strength, and latitudinal extent of storm events, and (3) dust storm timing and duration.

Martian dust is composed primarily of silicate particles and a few percent iron oxide minerals, and ranges in size from 0.1 to 10 μm (*Ockert-Bell et al.*, 1997; *Tomasko et al.*, 1999; *Wolff et al.*, 2006). It has been shown that the single scattering albedo and asymmetry parameter of this dust are size dependent and lead to absorption of short-

wave (solar) radiation, which then warms the atmosphere (*Wolff et al.*, 2006). This in turn leads to a thermal expansion of the entire atmosphere, elevating constant-pressure surfaces (or, equivalently, increasing the pressure at any given altitude). Though the airborne dust and the warming it causes are confined to the lower atmosphere (z <50-60 km)(*Gurwell et al.*, 2005), the thermal expansion it produces manifests throughout the atmosphere. Therefore accurate prescription of the latitudinal and vertical distribution of dust is important for accurately simulating middle atmosphere observations (e.g., *Bell et al.*, 2007).

2.4.1 Dust Treatment in GCMs

The treatment of the distribution of dust in general circulation models (GCMs) generally falls into the following categories, from simplest to most complex: (1) uniform or empirically prescribed dust distributions (e.g., *Lewis et al.*, 1999; *Nelli et al.*, 2007), (2) prescribed injection of dust into the modeled atmosphere, after which the model is free to transport and deposit the dust (e.g., *Murphy et al.*, 1995), and (3) fully interactive dust cycles that lift, transport, and deposit dust (e.g., *Kahre et al.*, 2006, 2008). Each of these treatments has its advantages and its own applications to which it is best suited. Treatments (1) and (2), for example, have the advantage that they are less computationally expensive, while treatment (3) treats the dust cycle self-consistently. Treatment (1) has the advantages that, depending on the level of detail of the prescription, it can: (a) provide a more controlled model calculation by removing anomalous dust events that may be present for any given MY (e.g., by using a horizontally uniform prescription of dust opacity) or (b) be better-suited to reproducing the atmosphere from a specific time-period and thus provide a better tool for interpreting datasets (e.g., by using empirically based dust distributions).

When a GCM is used for one of the applications suited to treatment (1), it typically employs one of two methods to prescribe the horizontal distribution of dust. The

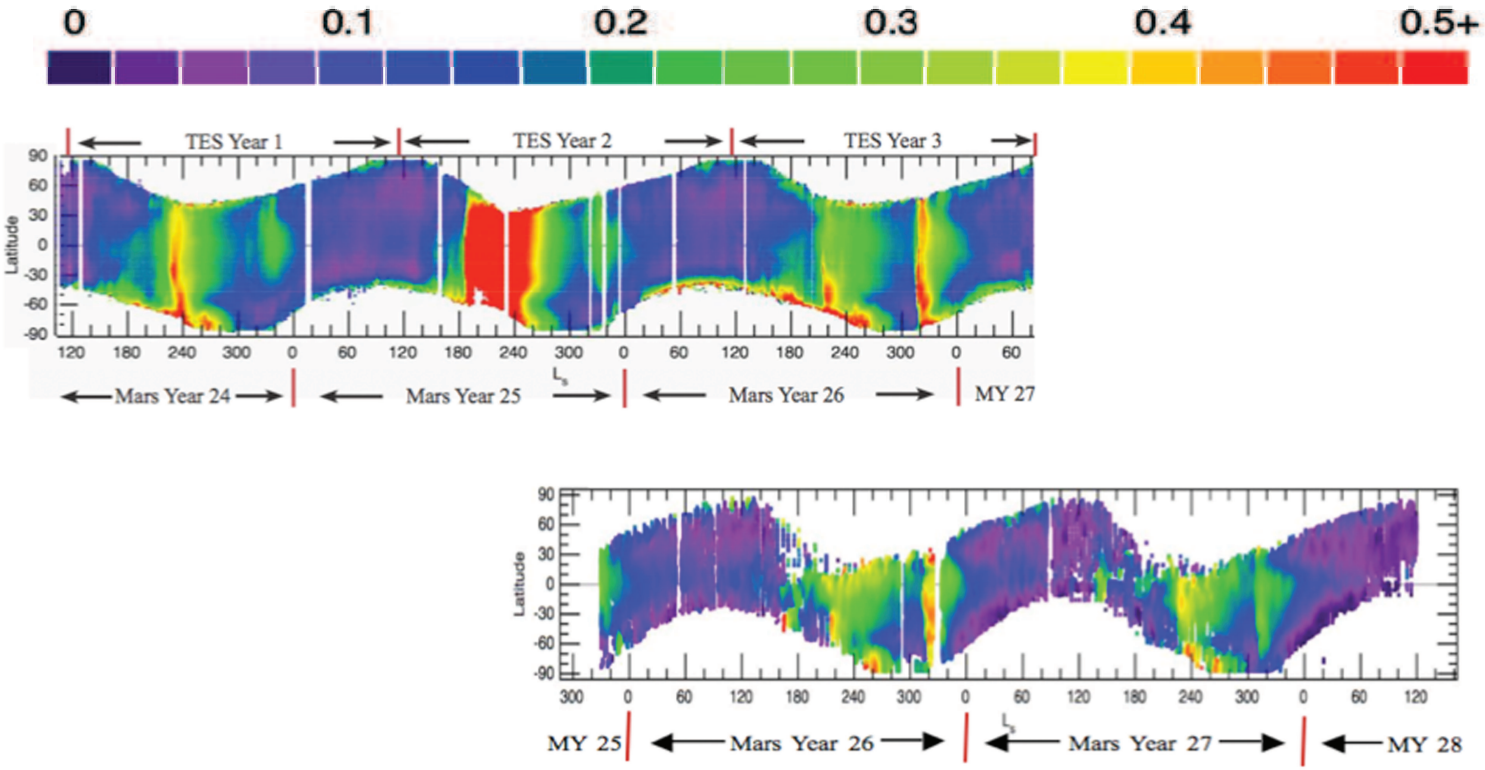

Figure 2.3: Record of lower-atmosphere dust opacity. The top panel displays MGS-TES 1075 cm^{-1} dust opacity from MY 24, $L_s = 120°$ through MY 27, $L_s = 81°$ (adapted from *Bell et al.*, 2007). The bottom panel displays longitudinally averaged ODY-THEMIS 1075 cm^{-1} dust opacity from MY 25, $L_s = 330°$ through MY 28, $L_s = 120°$ (adapted from *Smith*, 2009). The panels are arranged to highlight periods with coincident observations (e.g., MY 26).

Table 2.1: Mixing depths corresponding to a variety of ν values.

ν	Mixing Depth (H_p)
3e-1	1.2
3e-2	3.5
3e-3	5.8
3e-4	8.1
1e-4	9.2

first method is to prescribe a horizontally uniform column opacity at a specified magnitude. The second method is to use zonal averages or 2-D maps (i.e., varying with latitude and with longitude) of column opacity from spacecraft observations. The datasets commonly used for this are the 1075 cm^{-1} column opacities from the MGS-TES (MY 24-26) (*Smith*, 2004) and ODY-THEMIS (MY 27-31) (*Smith*, 2009) nadir observations. These zonal-mean or 2-D maps of column dust opacity distributions are incorporated into a model, typically at five-degree L_s intervals throughout the martian year.

Once the horizontal distribution of column opacity is assigned, a GCM conventionally distributes the dust in the vertical according to the Conrath formalism (*Conrath*, 1975)

$$q(z) = q_0 e^{\left[\nu\left(1-e^{[z/H]}\right)\right]}, \tag{2.1}$$

or some modification of this (for example, see *Forget et al.*, 1999). In Equation 2.1, q_0 is the specific concentration of dust at the surface (particles/g) and the parameter ν is given by $\nu = H\omega_0{}^*/K$, where H is the pressure scale height, $\omega_0{}^*$ is the terminal velocity of the dust particle at the surface, and K is the eddy diffusion coefficient (*Conrath*, 1975). The ratio given by ν characterizes the importance of vertical mixing versus gravitational settling and determines the top of the dust layer, z_t = -H ln(ν) (Table 2.1), above which, gravitational settling overtakes eddy mixing and the dust mixing ratio falls off rapidly (Figure 2.4).

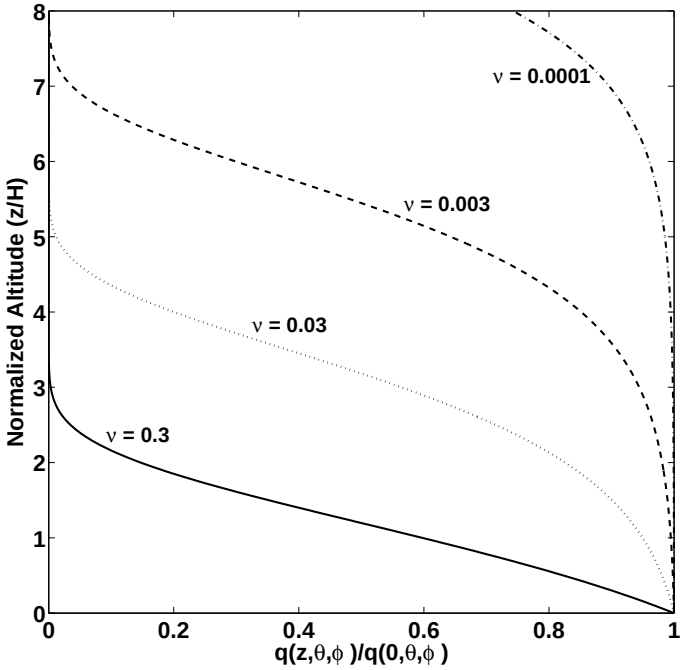

Figure 2.4: Specific concentration of dust as a function of altitude for the ν values used in this study. The x-axis is normalized to the amount of dust at z = 0.

Traditionally, Mars GCM simulations have used $\nu = 0.03$ (e.g., *Bell et al.*, 2007), which corresponds to a moderate mixing depth of 3-4 scale heights, depending on season. However, TES limb observations provide evidence that dust particles can be mixed much higher than five scale heights in regions of high opacity ($\tau \geq 0.5$) (*Smith*, 2003). *Smith* (2003) also showed that when more dust is in the atmosphere, it tends to be lofted higher. Accordingly, some GCMs allow ν to vary latitudinally with the local dust opacity, so that deepest mixing occurs where the vertically integrated dust opacity is largest.

2.4.2 Dust Prescriptions Used in this Study

As mentioned in Section 2.1, one of the primary objectives of the present work is to test the MGCM-MTGCM via comparison with the SPICAM observations. For this, we force simulations with dust conditions that as closely as possible reflect the state of the atmosphere at the time of the observations, namely, ODY-THEMIS MY27 1075 cm^{-1} opacities (*Smith*, 2009). Latitude-vs.-L_s zonal-mean column dust opacity distributions (M. Smith, personal communication, 2009) are incorporated into the MGCM code at five-degree L_s intervals throughout the martian year. The Mini-TES instruments on the MER rovers (*Smith et al.*, 2006; *Wolff et al.*, 2006) provide additional, independent point observations of dust opacities for the MY 27 timeframe that are used to complement the findings gleaned using the THEMIS opacities.

A second objective of the present work is to build upon previous investigations and explore the extent to which the middle atmosphere is sensitive to variations in the lower atmosphere's dust content and distribution. For this, we run simulations with a variety of latitudinal and vertical dust distributions, as shown in Table 2.2. If the structure of the middle atmosphere is sensitive to fine variations in the latitudinal distribution of lower atmospheric dust, this sensitivity is expected to manifest as differences between simulations conducted with THEMIS MY 27 dust loads (hereafter,

Table 2.2: Parameters used for the simulations in this study.

Simulation	Latitudinal Dust Prescription	ν	Solar Flux Index[1]	O Abundances[2]
1	MY 27[3]	3e-3	130	1.0
2	MY 24[4]	3e-3	130	1.0
3	MY 24[4]	1e-3	130	1.0
4	MY 24[4]	1e-4	130	1.0
5	Interactive mixing[5]		130	1.0
6	MY 27[3]	3e-3	70	1.0
7	MY 27[3]	3e-3	130	1.5

Simulation 1) and those conducted with dust loads from the first TES mapping year (hereafter, TES 1 and Simulation 2), whose dust record closely matches the THEMIS MY 27 record in terms of magnitude and latitudinal extent of storm events as well as dust opacity evolution (see Figure 2.3).

Here we also investigate the middle atmosphere's sensitivity to dust mixing depth by comparing simulations forced with TES 1 column dust opacities (*Smith*, 2004), and a variety of vertical mixing depths: ν= 3x10^{-3} (Simulation 2), ν = 1x10^{-3} (Simulation 3), and ν = 1x10^{-4} (Simulation 4) (Table 2.2). Simulation 4 is used as an extreme upper-limit case. In each of these simulations ν is allowed to vary latitudinally with the local dust opacity, so that deepest mixing occurs where the vertically integrated dust opacity is largest ($\tau \sim 1.3$). In none of these simulations are we considering great dust storm events, where $\tau \gg 1$.

A final suite of simulations is performed using *Kahre et al.* (2006, 2008)'s innovative and interactive dust-mixing scheme (Simulation 5). This scheme is an example of treatment (3) described above. In this scheme, the altitude to which dust particles are lofted is dependent upon the size of the particle. Finer particles are lofted higher and

[1]A proxy for solar activity in the MGCM-MTGCM (see Section 2.7).
[2]Normalized to presently accepted values.
[3]From THEMIS.
[4]From TES.
[5]Self-consistent and independent and thus does not require a ν value to be declared.

remain suspended longer than their heavier counterparts, which gravitationally settle more rapidly. Since a dust particle's size affects its scattering properties, this new scheme is expected to capture the atmosphere's thermal structure more accurately than simulations forced with latitudinally uniform mixing depths. In this mixing scheme, the three-dimensional distribution of dust is self-consistently calculated and therefore Simulation 5 requires neither latitudinal dust distribution nor ν be specified.

2.5 Methodology

2.5.1 Vertical Structure

The 616 SPICAM temperature and density profiles are grouped according to solar longitude (L_s = 0°±15°, 30°±15°, 60°±15°, etc.), and then, within these seasonal groupings, further binned as a function of latitude (30° increments) and LT (2-hour increments). The 30° latitude x 2 hour local time bin with the greatest sampling is selected for each seasonal grouping for comparison with the model results. Our focus in examining the vertical structure of temperature and density is on the solstice seasons. The most populous bin for the southern winter season (L_s = 120°±15°), contains 48 SPICAM profiles and addresses southern (winter) middle latitudes on the nightside of the planet (latitude = 30°S - 60°S and LT = 0.5 - 2.5; hereafter, Bin 1). The most populous bin for the southern summer season (L_s = 270°±15°), contains 16 SPICAM profiles and addresses southern (summer) tropical latitudes on the nightside (latitude = equator - 30°S and LT = 0.0 - 2.0; hereafter, Bin 2).

For the purpose of validating the model's ability to reproduce the observed vertical temperature structure, we compare the zonally averaged simulation profile for each L_s-latitude-LT bin's center point against the average of the SPICAM temperature profiles in each L_s-latitude-LT bin (since the observations in each bin span all longitudes, the result is essentially a zonally averaged profile). A 5-vertical point moving average is

applied to the zonally averaged SPICAM profile in order to minimize some of the finer vertical scale structure that the model results are incapable of addressing.

For the purpose of validating the model's ability to reproduce the observed vertical density structure, we compare the average of the simulation profiles within each L_s-latitude-LT bin to the individual SPICAM profiles in each L_s-latitude-LT bin. Individual SPICAM profiles are retained for the density comparison (and not for the temperature comparison) because...

2.5.2 Seasonal Structure

In order to isolate seasonal variations in the middle atmosphere temperatures and densities, analysis of the full profile is replaced by analysis of temperature and density at three altitudes: 80 km, 100 km, and 130 km above the areoid. These altitudes encompass the upper mesosphere through the lower thermosphere. We bin the SPICAM temperatures and densities at these altitudes into five latitude bins: 90°-70°S, 70°-45°S, 45°S-45°N, 45°-70°N, and 70°-90°N. By isolating the region from 45°S-45°N, we ensure that our analysis of seasonal variations of the low-to-mid latitudes is not muddied by dynamical polar warming signatures (*Bougher et al.*, 2006), and by isolating the regions from 70°-90°, we expect that our analysis of seasonal variations of the polar regions will highlight any signatures of dynamical polar warming that may exist in the data. Modeled temperatures and densities are extracted at the L_s, LT, and latitude of the SPICAM observations.

2.5.3 Inter-model Comparison of Mesopause Temperature and Level

A third objective of the present study is a preliminary inter-model comparison of middle-atmosphere calculations. To this end, MGCM-MTGCM temperature profiles are also compared with the SPICAM observations at each solstice near the equator. For southern winter solstice (L_s = 90°-120°), 39 SPICAM profiles are available in

the latitude bin 17°S-16°S (hereafter, Bin 3). These 39 profiles span all longitudes on the nightside of the planet (LT = 2.6-4.8). For southern summer solstice (L_s = 240°-270°), 48 nightside SPICAM profiles are available in the latitude bin 30°S-10°N. This choice of bins permit a direct comparison with recently published results from the LMD MGCM (see Fig. 16 in *Forget et al.* (2009)).

2.5.4 Heat Balances

The middle atmospheric temperature structure is generally regulated by a balance between five heating terms: molecular thermal conduction, horizontal advection, adiabatic warming/cooling, radiative heating (EUV, UV, & IR), and CO_2 15-μm (IR) cooling (*Bougher et al.*, 1999a, 2000, 2009). Discrepancies between the observed and calculated temperature profiles (see Sections 2.6.1 and 2.6.3), particularly in the level and temperature of the mesopause, indicate that one or more of these terms are incorrect. Vertical profiles of the simulated heat balance terms can provide a clue as to the culprit.

2.6 Results

2.6.1 Vertical Structure

The average of the 48 SPICAM profiles in Bin 1 displays a mesopause temperature of 105 K at an altitude of 103 km (Figure 2.5A). The temperature lapse rate in the 80-103 km altitude region is subadiabatic at $\sim$ 1.0 K/km. Below the mesopause, Simulation 1 is 2-8 K warmer than the observations. Simulation 1 produces a good fit to the observations with a mesopause that is $\sim$2 K warmer than the observed value and 3 km lower. Above the Simulation-1 mesopause, the temperature increases more rapidly with height than does the observed temperature and is $\sim$20 K warmer than the observations at 130 km. The Simulation-2 mesopause occurs at a height similar

to the observed mesopause but is ∼15 K warmer than observed mesopause.

The Bin-1 SPICAM density profiles (Figure 2.6A) are physically consistent with Bin-1 SPICAM temperatures. The 48-profile mean density at 80 km is ∼1.0 x 10^{-6} kg m^{-3} and it decreases at a rate that increases with height up to the mesopause. A vertical density structure such as this is expected for an environment in which temperature (and thus scale height) decreases with height. Above the mesopause, where temperature increases with height, the rate at which the Bin-1 SPICAM density decreases with height itself decreases as the scale height increases. Below ∼115 km, the simulated density is less than observed, with a Simulation-1 80-km density of ∼ 8.5 x 10^{-7} kg m^{-3}. Such a density offset at this lower boundary could be due to a simulated lower atmosphere (MGCM) that is too cold, resulting in an overly vertically contracted atmosphere (i.e., hydrostatic pressure surfaces occur at lower elevations in the model than in the real atmosphere).

The average of the 16 profiles in Bin 2 displays a mesopause temperature of 115 K at an altitude of 118 km (see Figure 2.5B). The Simulation-1 and Simulation-2 (see Table 2.2) temperature profiles correspond well with the observations in the 90-110 km altitude range. However, the height of the mesopause is poorly fit by both simulations (∼100 km in Simulation 2 and ∼ 108 km in Simulation 1). The observed 130-km southern summer temperature (Bin 2) is 36 K colder than the southern winter temperature (Bin 1) at the same height (and higher latitude), indicating a difference in the heat balances. Moreover, the simulated 130-km Bin-2 temperatures are 30-40 K colder than those of Bin 1, suggesting that this seasonal and latitudinal variation in the heat balances is well-captured by the model.

The Bin-2 SPICAM density profiles exhibit less non-exponential structure (see Figure 2.5B) than the Bin-1 profiles, which is consistent with the more isothermal nature of the Bin-2 temperature profiles. The Bin-2 average density at 80-km is ∼ 4 x 10^{-6} kg m^{-3}, a factor of four greater than the Bin-1 average 80-km density. This

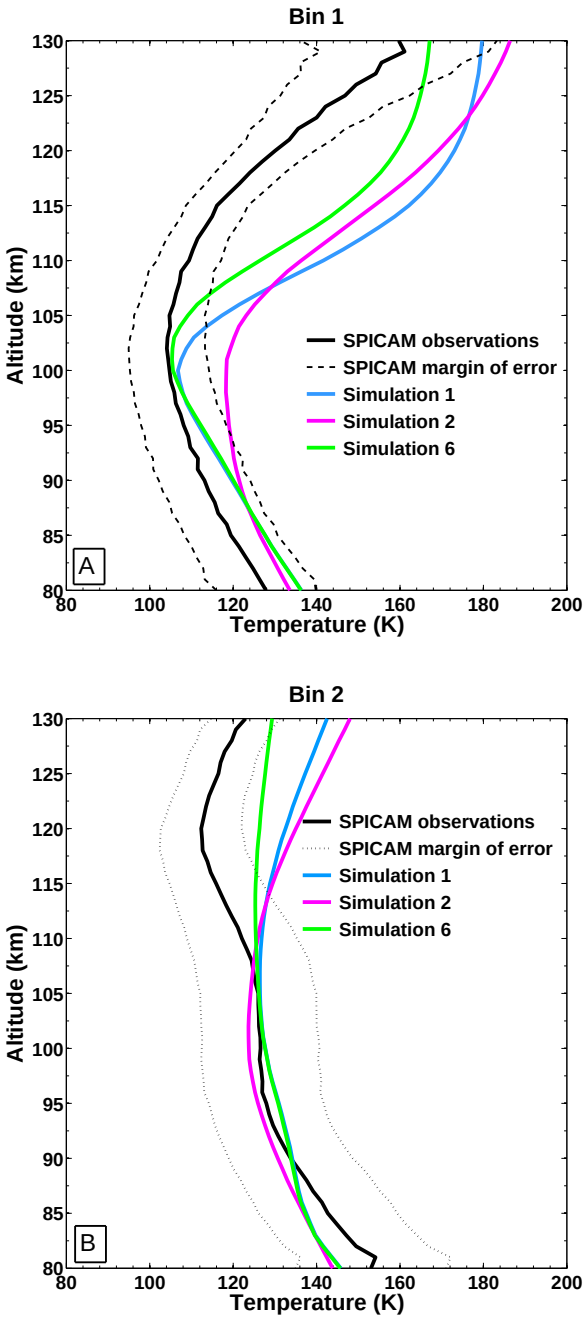

Figure 2.5: Observed and modeled nightside temperature profiles for (A) Bin 1: southern middle latitudes during southern winter ($L_s = 120° \pm 15°$), and (B) Bin 2: southern tropical-subtropical latitudes during southern summer ($L_s = 270° \pm 15°$). In each panel the black curve is the average of all SPICAM profiles falling within the indicated bin, and the dashed lines show the average envelope of uncertainty associated with the retrieved temperatures (see Forget et al., 2009). Shown in color are zonally averaged modeled profiles corresponding to the mean latitude and mean local time of the bin, for Simulation 1 (blue), Simulation 2 (magenta), and Simulation 6 (green) (see Table 2.2).

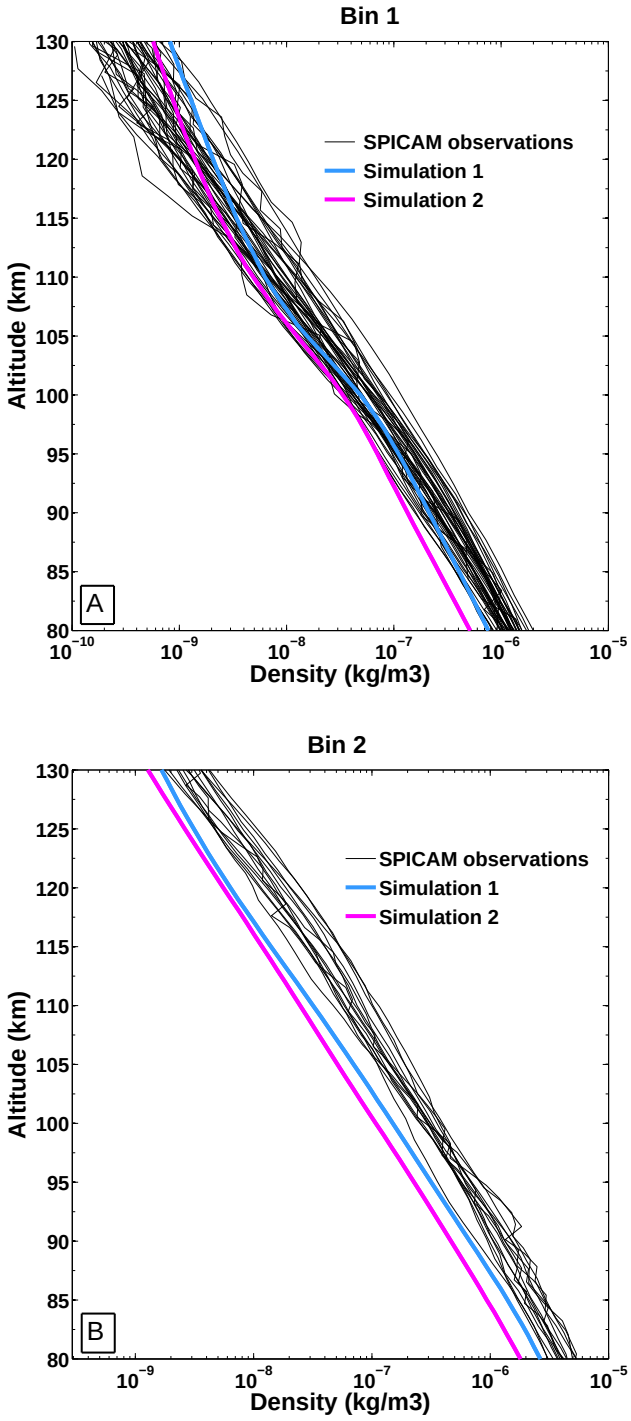

Figure 2.6: Observed and modeled nightside density profiles for the same solstice cases addressed in Figure 2.5. In each panel the black curves represent the SPICAM observations falling within the bin. Shown in color is the average of the model-generated profiles corresponding in time and space to the SPICAM profiles, for Simulation 1 (blue) and Simulation 2 (magenta).

seasonal enhancement is due to: (1) the perihelion lower atmosphere being warmer and more vertically extended (itself a result of the greater insolation at this season and the enhanced suspended dust at this season) and (2) the ∼25% greater atmospheric mass during the perihelion season (itself a result of the seasonal sublimation of the CO_2 polar caps, see Section 1.2.3.1). Throughout the profile, the simulated Bin-2 density values are smaller than the observed values. At 80 km, the simulation that comes closest to the observations is Simulation 1, having a density ∼66% of the mean observed value. If the pressure associated with the 80-km height in the simulated atmosphere was the same as that in the observed atmosphere, the overly cold model temperature at 80 km would itself result in a simulated density at 80 km that exceeds the observations. The comparison highlighted here must then arise from a simulated lower atmosphere that is too cold. This would result in an overly vertically contracted atmosphere and thus explain the simulated density (and pressure) values at and above 80 km that are smaller than the observations.

2.6.2 Seasonal Structure

Our investigation of the seasonal variation of SPICAM temperatures and densities is constrained by the latitudinal coverage available during each season (see Figure. 2.2b). For most L_s intervals throughout the martian year, observations are available for the low latitudes of the spring/summer hemisphere through the middle latitudes of the fall/winter hemisphere. The discussion in the following sub-sections pertains to Figures 2.7 and 2.8.

2.6.2.1 $L_s = 0°$-$90°$

During northern spring, the SPICAM observations migrate from northern (spring) middle latitudes ($L_s = 0°$-$30°$) through both southern and subtropical latitudes ($L_s = 30°$-$60°$), to middle southern (autumn) latitudes ($L_s = 60°$-$80°$) (see Figure 2.2b).

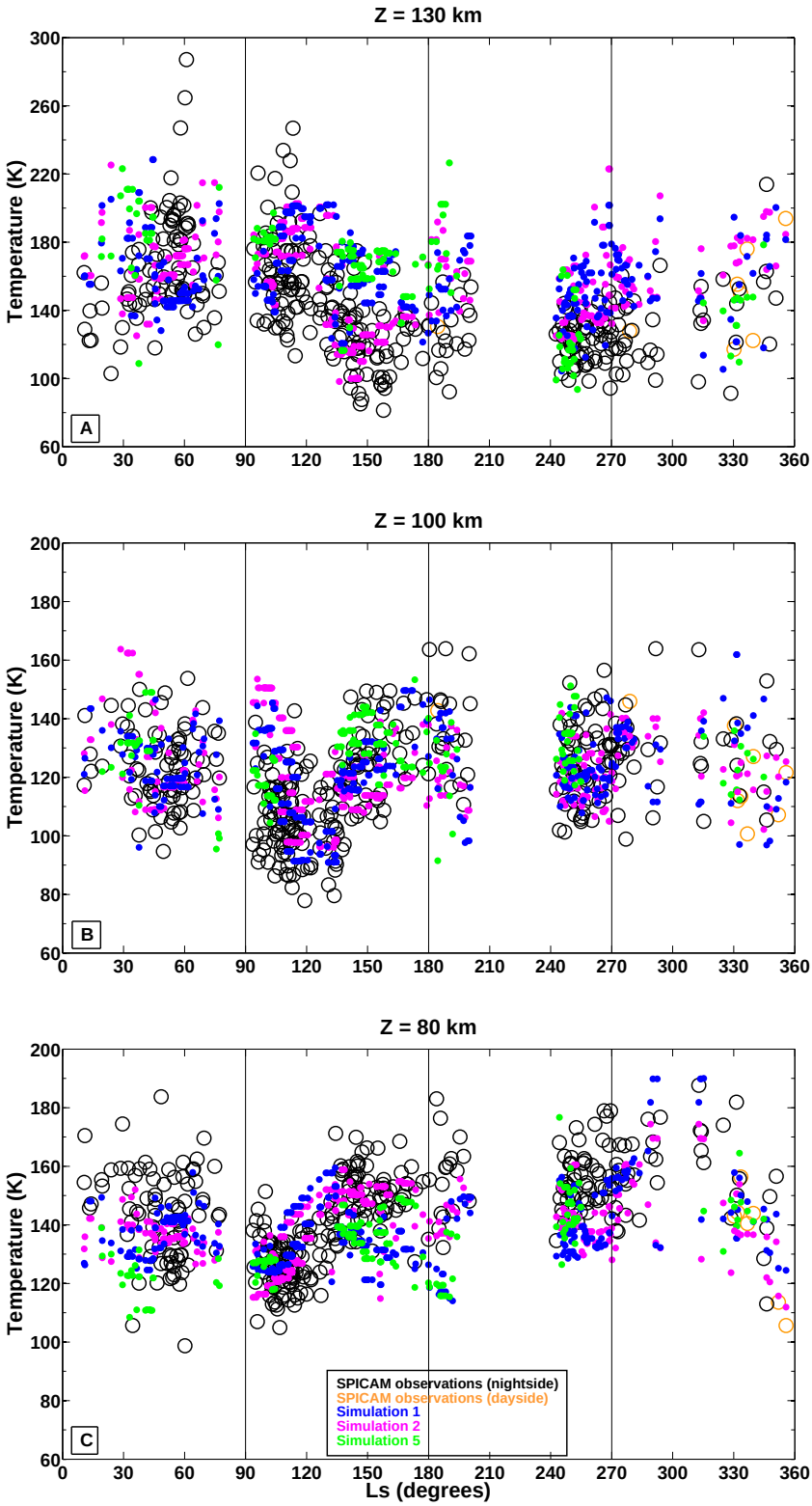

Figure 2.7: Observed and modeled seasonal temperature structure at low latitudes (45°S-45°N), at altitudes of (A) 130km, (B) 100 km, and (C) 80 km. Shown in color are simulations driven with various latitudinal and vertical dust distributions: Simulation 1 (blue), Simulation 2 (magenta), and Simulation 5 (green). Notice that the temperature scale for A is different than that for B and C.

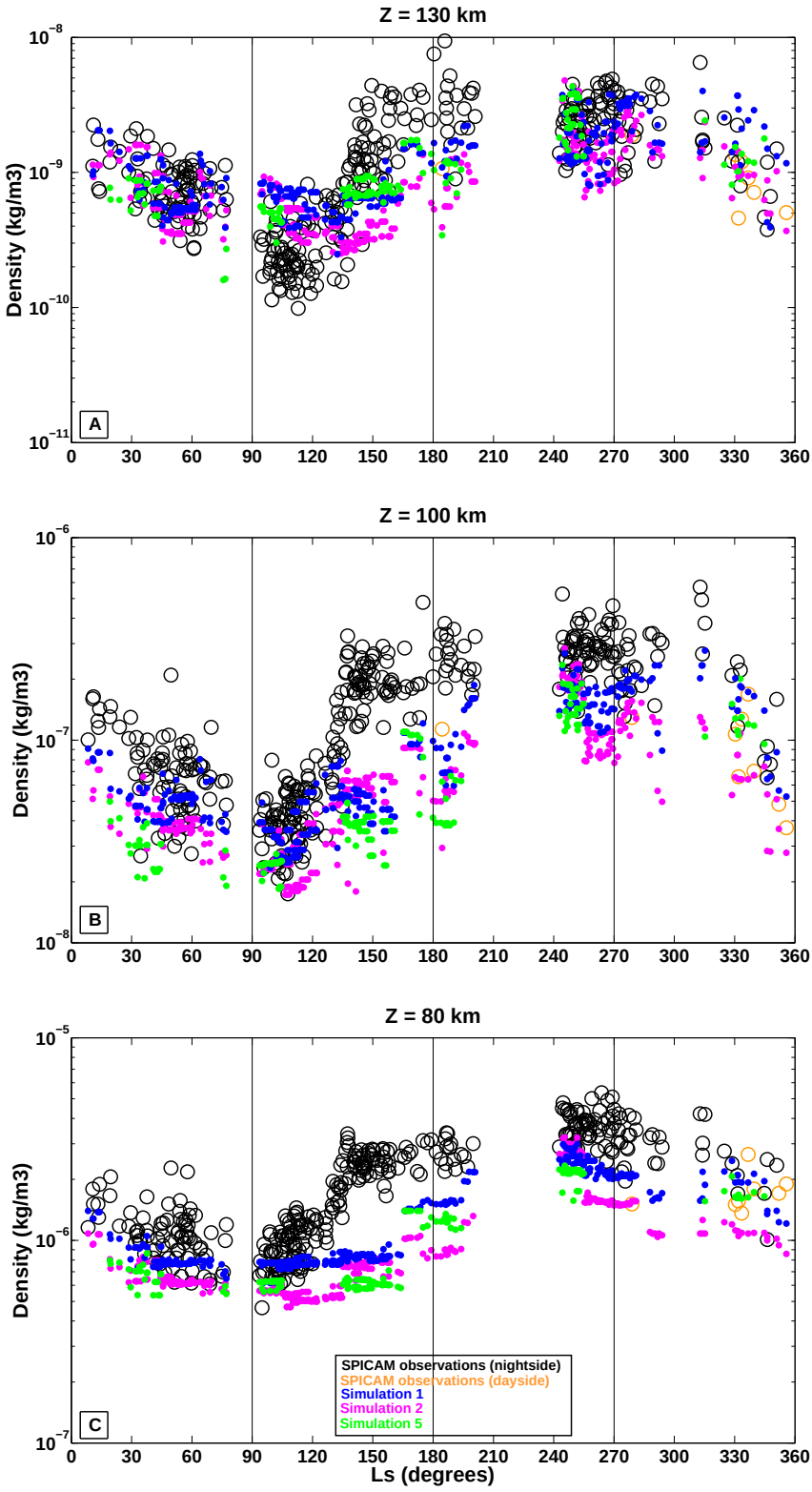

Figure 2.8: Same as Figure 2.7, except for densities. Here, the model performs well during the low-dust season (L_s = 0°-120°) and the high-dust season (L_s = 250°-360°), but displays difficulty during the pre-dust-season ramp-up period (L_s = 120°-200°). Notice that the density scales are different for each panel.

As northern spring progresses and the observations drift southward, 80-km temperatures (Figure 2.7C) exhibit an increased range with relatively constant maxima near 160 K and decreasing minima from 140 K to near 120 K in the L_s = 30°-60° time interval. Thus, northern middle-latitude early-spring 80-km temperatures are as warm as those at southern middle-latitudes during late autumn. A similar trend is apparent in the 100-km temperatures, which are ∼20 K colder than the 80-km temperatures. Temperatures at 130 km also exhibit an increase in range over the L_s = 0°-90° period, but the initial temperatures of 130-140 K represent the minima of the range, which expands to include warmer temperatures (as warm as 210 K) through L_s= 60°, and shrinks (to cooler temperatures) thereafter through L_s = 80°. This cooling coincides with the observations moving to middle southern (autumn) latitudes.

The simulated temperatures exhibit a narrower range at 80 km than the observations. The simulated 80-km temperatures range between 120 K and 150 K, and do not get quite as warm as the observations. Simulation 5 exhibits the narrowest range of 80-km temperatures. At 100 km, the simulated temperatures span a range similar to the observations. At this height, all three horizontal dust scenarios (Simulations 1, 2, and 5) result in similar temperatures. At 130 km, Simulations 1 and 2 produce temperatures that agree well with the magnitude and range of the observations, though they do not reproduce the few outlying hot observations. In addition, the simulations at 130-km exhibit a marked drop in temperatures during the L_s = 40°-60° interval with a subsequent return of warmer (180-220 K) temperatures through L_s = 80°.

During the northern spring season, SPICAM density values at 80, 100, and 130 km (see Figure 2.8) exhibit a trend of decreasing magnitude with advancing season (and southward profile migration). The observed densities span one order of magnitude at both 100 and 130 km altitudes, and average values at 100 km are ∼2 orders of magnitude greater than the 130 km density values. This corresponds to 4 to 5

density scale heights. The temporally decreasing density values do not correspond to obvious seasonal trends in the accompanying temperatures, implying that the density trend at all three altitudes is a hydrostatic consequence of decreasing temperatures at even lower altitudes. Lower atmosphere temperatures are observed to cool during the planet's approach to aphelion and the accompanying annual minimum in atmospheric dust content (*Smith*, 2004). The factor of ∼2 decrease in 80-km density between early spring at ∼45°N and late spring at ∼45°S requires a 10 K cooling of the atmospheric column below 80 km (from northern mid-latitudes at $L_s = 0°$ to southern mid-latitudes at $L_s = 90°$), which is generally consistent with TES and THEMIS temperature observations.

The simulated density values do, at all three altitudes, also exhibit an overall decrease with advancing season. However, at 80 km the modeled densities exhibit a much narrower range than do the observed densities, and they are skewed toward the lowest of the observed values. The model density values at 100 km exhibit a greater range than those at 80 km, but again the simulated range is not as great as the observed range, and the simulated density values are again at the lower end of the observed values. At 130 km, the simulated density values exhibit a range that is consistent with the observed range, and magnitudes that coincide with the observed values. Thus, the simulations improve with decreasing pressure (increasing altitude). This may be a consequence of model temperatures warming beyond the observations at these higher altitudes.

2.6.2.2 L_s = 90°-180°

During southern winter, the SPICAM observations span southern middle and low latitudes. Beginning at $L_s \sim 140°$, the observation range expands northward to encompass northern low and middle latitudes as well (see Figure 2.2b).

During the L_s = 90°-180° southern winter interval, the SPICAM temperatures at

80 km exhibit a general warming trend, from mean values of ∼120 K at $L_s = 90°$ to mean values of ∼155 K at $L_s = 180°$. The branch of higher temperatures that develops at $L_s \sim 145°$ coincides with the inclusion of several northern subtropical profiles at that late northern summer season (see Figure. 2.2b). The 100-km temperatures exhibit cooler values during the $L_s = 90°$-$140°$ time period than were present during the preceding season, but the range during this early southern winter interval is large, from 80 K to 125 K. The warm extent of the range increases to 155 K subsequent to $L_s = 140°$, commensurate with the branch of warming noted at 80 km. At the same time, the cool extent of the range also warms to 110 K. At 130 km, there is a general cooling trend through $L_s = 150°$, with no prominent feature evident at $L_s = 140°$. The minimum 130-km temperatures during this interval occur at $L_s = 150°$, and at 80 km, are 55 K colder than the warm end of the well-populated range at the same season, and 175 K colder than the absolute maximum during this southern winter season.

During the southern winter season, the modeled temperatures exhibit trends and absolute values similar to the observations. Overall, the simulations generated with prescribed dust loadings (i.e., Simulations 1 and 2) agree better with the observations than do the simulation generated with the interactive dust scheme (Simulation 5). However, during the latter third of the season (as the dust seasons is ramping up), the interactive dust scheme produces temperatures at 100 km that match the observations better the other Simulations.

The SPICAM density values during the $L_s = 90°$-$180°$ interval exhibit prominent increases at all three altitudes. These trends set in shortly after $L_s = 125°$ at all three levels. The 80-km and 100-km density values increase steadily through $L_s = 140°$, after which the rate of their increase slows through $L_s = 180°$. At 130 km, the prominent increase in density continues through $L_s = 160°$. The increasing temperatures at 80 km during this same season would themselves in isolation argue

for a decrease in density there if no other effects were considered, but the increasing density in the presence of the increasing temperatures implies that warming is also occurring at altitudes below 80 km which hydrostatically increases the pressure at 80 km. This warming is occurring in the presence of the lowest surface pressures of the annual cycle (as CO_2 is condensed out on the southern winter cap, see Figure 1.5), and the column temperature increase below 80 km must also overcome that effect.

The simulated density values during the L_s = 90°-180° interval also exhibit an increasing trend at all three altitudes. However, at 80 km, the simulated values exhibit a smaller range than the observations, and, after L_s = 125°, the simulated density values are significantly smaller than the observations. The comparison improves somewhat after L_s = 160°. The modeled 100-km density values do compare well with the observations through L_s = 120°, but thereafter the modeled values increase at a slower rate than the observations. At 130 km, the overall comparison is better than at the lower altitudes, though the modeled values during L_s = 90°-140° cluster at the upper range of the observations while after L_s = 140°, they cluster at the lower end of the observations.

2.6.2.3 L_s = 180°-270°

The L_s = 180°-270° seasonal interval is dominated by a SPICAM data gap extending from L_s = 200°-240°. During the L_s = 180°-200° and L_s = 240°-270° intervals, SPICAM observations span southern low latitudes through northern middle latitudes, with the majority of the observations at the subtropical latitudes of both hemispheres (see Figure. 2.2b).

SPICAM temperatures during the southern-spring/northern-autumn interval do not exhibit any prominent temporal trends, but large ranges are evident at all heights (130 K -180 K at 80 km, 110 K - 160 K at 100 km, and 95 K - 160 K at 130 km). Interestingly, though the 80-km and 100-km temperatures are at or near their annual

maximum during this perihelion season ($L_s = 250°$), the 130-km temperatures at this season are clustered at a cooler mean value than those from the slightly post-aphelion season ($L_s = 100°$). Consequently, this southern summer season boasts the largest 100-130 km environmental lapse rate of any season during the year, which should have implications for vertical wave propagation at this season.

Simulated temperatures during the $L_s = 180°$-$200°$ time period agree well with the observations. The best comparison is at 100 km, while at 80 km the simulations cluster toward the lower end of the observations and at 130 km the simulations cluster at the higher end of the observations. These same trends are present, though less pronounced, during the $L_s = 240°$-$270°$ interval, and are consistent with the vertical profiles discussed in Section 2.6.1 (Figure 2.5b). The Simulation-5 results exhibit a prominent warming trend at 130 km over this time interval that is not present in the Simulation-1 or Simulation-2 results.

There is little trend in the SPICAM density values at any of the three altitudes during the northern-autumn/southern-spring period. The spread of density values increases with height.

During $L_s = 180°$-$200°$, the modeled density values are noticeably smaller than the observations at all three altitudes, a continuation of the pattern seen during the preceding season ($L_s = 90°$-$180°$). During $L_s = 240°$-$270°$, the 130-km modeled density values agree well with the observations. Simulation 2 provides the best correspondence. The modeled density values at 100 km and 80 km during the $L_s = 240°$-$270°$ time period are less than the observations, but the discrepancy is smaller than the discrepancy for the $L_s = 180°$-$200°$ period.

2.6.2.4 $L_s = 270°$-$360°$

During the $L_s = 270°$-$360°$ season, the SPICAM profiles are confined to the northern hemisphere, with the majority of the profiles occurring during the earlier and

latter periods of this seasonal interval.

The 80-km temperatures exhibit a wide spread through $L_s = 330°$ (including the more greatly populated $L_s = 270°$-$300°$ time period). A cooling trend is suggested after $L_s = 330°$, but the spread remains large (110 K - 150 K). The 100-km and 130-km temperatures also continue to exhibit a large range during this seasonal interval with no clear temporal trends.

The modeled temperatures compare well with the observations and exhibit wide ranges at each altitude during this $L_s = 270°$-$360°$ time interval. The modeled 80-km temperatures exhibit a cooling trend during the $L_s = 330°$-$360°$ time period, which corresponds well to the 80-km observations. The modeled 130-km temperatures are on average consistent with the warm end of the observations.

After $L_s = 330°$, the SPICAM density values decrease at all altitudes, which is consistent with the decreasing noted during the $L_s = 0°$-$80°$ time interval. This density decline during late northern winter is hydrostatically consistent with the decline in the 80-km temperature observations.

During the $L_s = 270°$-$330°$ time interval, the modeled density values are generally smaller than the observations, especially at 80 km and 100 km, but after $L_s = 330°$, the modeled densities exhibit better agreement with the observations, especially at 130 km.

2.6.3 Inter-model Comparison of Mesopause Temperature and Level

Preliminary inter-model comparisons between the MGCM-MTGCM and the LMD GCM reveal that both general circulation models calculate mesopause values for Bin 3 conditions that are too warm and occur too low in the atmosphere (Figure 2.9). Both models calculate the mesopause at pressures of $\sim 2.5\text{x}10^{-3}$ Pa, whereas observations place the mesopause at a pressure of $\sim 1\text{x}10^{-3}$ Pa. The MGCM-MTGCM fares better than the LMD GCM at calculating the temperature of the mesopause, achieving a

minimum temperature of 112 K (versus 120 K), compared to the observed minimum of 104 K.

2.6.4 Heat Balances

Figure 2.10 shows the heat-balance terms that correspond to the zonally averaged bin-average temperature profile for Bin 3 calculated from the MGCM-MTGCM (red curve in Figure 2.9). Since the Bin 3 domain is confined to the nightside of the planet, the direct solar heating term is zero. The minimum net heating rate occurs at 2.5x10^{-3} Pa, which is consistent with the modeled mesopause. The adiabatic warming term is negative below this level (indicative of rising motion) and positive above this level (indicative of subsidence), indicating there is vertical convergence at this level in the model. In addition, the horizontal advection heating term is positive below the calculated mesopause level and remains positive above it, increasing to a peak near 4x10^{-4} Pa, well above the observed mesopause. Weaker global winds at these pressures would decrease warm air advection to the nightside, thereby decreasing the dynamical heating terms, which in turn would raise the calculated mesopause as well as decrease its magnitude. Gravity waves propagating from the lower atmosphere are capable of depositing significant amounts of energy and momentum in the middle and upper atmosphere (*Parish et al.*, 2009; *Medvedev et al.*, 2011a,b; *Bougher et al.*, 2011a), potentially slowing global winds and significantly impacting the dynamical heating processes in this region. The incorporation of vertically propagating gravity waves into the MGCM-MTGCM code is therefore expected to decrease global winds at these altitudes and thereby improve mesopause calculations.

The other significant curve in Figure 2.10 is the CO_2 15-μm IR cooling term. As mentioned in Section 2.3, the magnitude of this cooling term is highly sensitive to atomic O abundances, which are poorly known at present. O abundances that are greater than current estimates would result in more frequent CO_2 - O collisions,

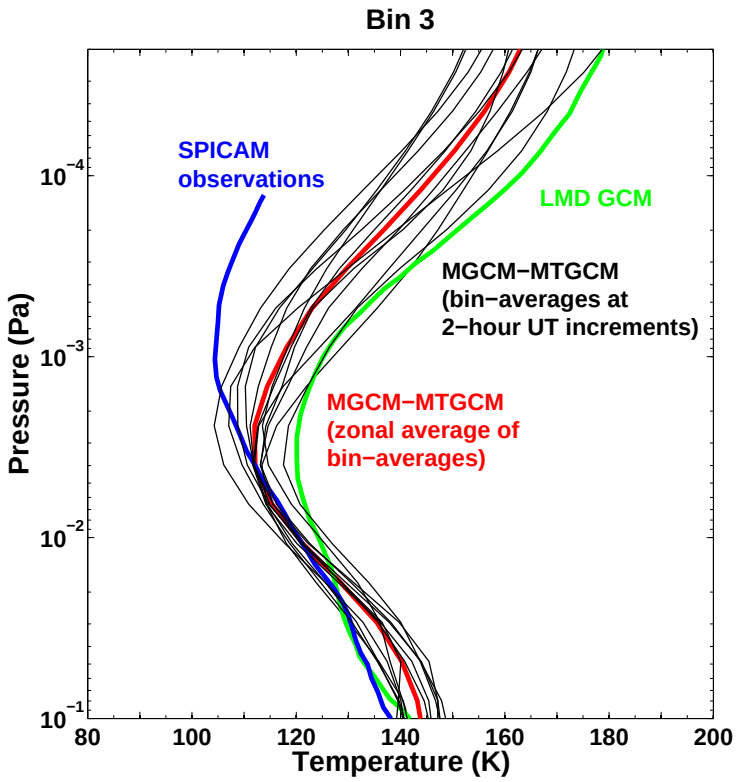

Figure 2.9: Observed and modeled temperature profiles for Bin 3 (nightside at southern tropical latitudes during southern winter), for data-model and inter-model comparisons. The blue curve represents the average of the 39 SPICAM observations falling within the bin (these profiles span all longitudes). Each black curve represents the bin-average model profile (average of the 39 MGCM-MTGCM-generated profiles corresponding to the precise observation latitudes), at a distinct 2-hour UT (30 longitude) increment across the globe. The red curve is the zonally averaged bin-average MGCM-MTGCM-generated profile (i.e. the average of the black curves). The green curve represents the average LMD-GCM profile (see Forget et al., 2009, Fig. 16, Row 3, Column 1). The appropriate data-model comparison is between the blue and red curves while the appropriate inter-model comparison is between the red and green curves.

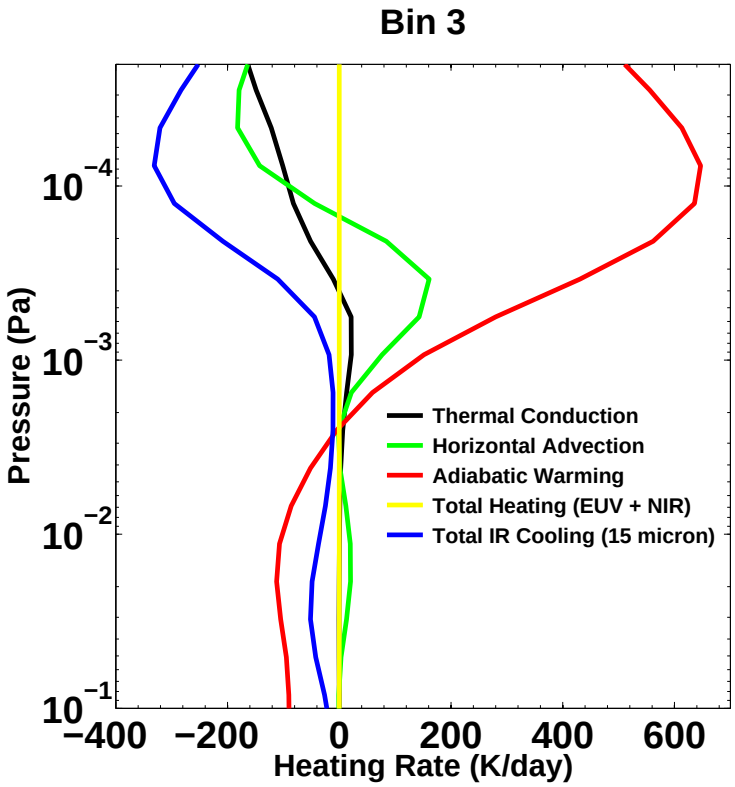

Figure 2.10: Calculated heat-balance terms for the Bin 3 mesopause region. The zonally averaged bin-average model temperature profile (red curve in Figure 2.9) is directly related to the balance achieved among the heating and cooling terms shown here.

which in turn would cause 15-μm cooling rates to increase. Therefore, a significant enhancement of O abundances above presently accepted values may also lead to a reduction in modeled mesopause temperatures that would bring the modeled values into alignment with the values observed in Bin 3.

2.7 Discussion

The results of the vertical density structure investigation show that model performance does exhibit a significant dependence upon dust specifications, particularly during the southern summer season. During this high-dust season, the MGCM-MTGCM simulations conducted with THEMIS opacities result in an improvement

over those conducted with TES 1 opacities. However, the fact that the model struggles to reproduce the observed densities at all altitudes, regardless of the dust loads employed, suggests another process is at work in the atmosphere during southern summer that is not accurately represented in the calculations. In the past, a height offset has often been used to mimic adjustment of the height scale consistent with an adjusted temperature structure (e.g., *Bougher et al.*, 1999b). No height offsets are used in the present study. Rather, the present work is an effort to move away from the need for such offsets.

The results of the seasonal density investigation further confirm the model's ability to accurately reproduce observed middle-atmosphere densities during low-dust and high-dust conditions, when provided with dust opacities that are in accord with the observation time period. At the same time, regardless of the accuracy of the dust prescription, there remain discrepancies between the MGCM-MTGCM density simulations and the SPICAM observations during the anomalous MY27 dust ramp-up period ($L_s = 140°$-$200°$), a period that typically exhibits small dust loads. This reveals that aside from the prescribed latitudinal (zonally averaged) and vertical distributions of dust, there is some process not well represented in the model that is influencing the densities in the middle atmosphere during this atypically dusty period. *Forget et al.* (2009) reveal a similar discrepancy between the SPICAM observations and LMD GCM simulations conducted with TES 1 dust loads. They propose that this may be due to an anomalous dust event that is seen in both the global THEMIS-derived opacities (see Figure 2.3 bottom panel) and point observations from the more sensitive Mini-TES instruments onboard the MER rovers (*Smith et al.*, 2006). The THEMIS-derived dust opacity values decline rapidly following the short $L_s = 140°$ event, while the Mini-TES observations exhibit a less rapid decline. If the longer decay time observed in the Mini-TES dust opacity data is in fact more appropriate for this period, lower-altitude atmospheric temperatures would remain warm longer due

to suspended dust levels remaining enhanced for a more prolonged period than the THEMIS measurements indicate. This could result in modeled mesosphere conditions possessing higher density values.

The results of the thermal investigation show that the MGCM-MTGCM consistently reproduces the magnitude of the nightside thermal profile within the margin of error of the observations nearly up to the mesopause altitude, during both solstice seasons, when dust opacities that are consistent with the observed time period are employed (i.e., THEMIS MY27 dust opacities). However, the precise temperature and altitude of the mesopause are not reproduced. The significant increase of both dynamical terms directly above the calculated mesopause (see Figure 2.10) indicates that the modeled mesopause is too warm and too low in the atmosphere because these dynamical terms are too large. This may be evidence that the global winds in the model are too strong and suggests that processes that impact global winds are missing from the MGCM-MTGCM (e.g., gravity wave momentum forcing) and need to be addressed before further progress can be made toward constraining the nightside heat balances and reproducing mesopause temperatures (*Bougher et al.*, 2006).

Above the mesopause, the simulated temperatures are consistently too warm. One explanation for this is the solar fluxes employed in these baseline MGCM-MTGCM simulations. Incoming solar EUV and UV largely dominate the thermal structure of the upper atmosphere and drive significant variations over the solar cycle. As noted in Section 2.3, solar forcing is an adjustable parameter within the MGCM-MTGCM code. The MGCM-MTGCM uses the F10.7 cm index as a proxy for solar activity, with F10.7 = 70, 130, and 200 (at Earth) corresponding to solar minimum, moderate and maximum conditions, respectively. In Section 2.2 it was mentioned that the first year of SPICAM observations, which are employed in the present study, began in February 2004 (F10.7 $\sim$ 115.5) and ended March 2006 (F10.7 $\sim$ 81.6). Therefore, the moderate solar flux parameterization (F10.7 = 130) employed in the baseline MGCM-

MTGCM simulations presented in this study produces solar EUV and UV heating that is somewhat large for the observed time period. However, simulations conducted with solar minimum conditions (F10.7 = 70) (Simulation 6) produce only slightly improved thermal structure in the upper altitudes investigated here (see Figure 2.5 green curve). At an altitude of 125 km, simulations conducted with solar minimum fluxes produce temperatures that are 10 K cooler than those conducted with solar moderate fluxes. Therefore, this explanation is not chiefly responsible for the pattern found in the temperature profile comparisons, namely the over-warming seen above the mesopause.

A more likely explanation for the high nighttime temperatures in the model above ∼105-110 km is underestimated CO_2 15-μm cooling rates. This situation would result if simulated nightside atomic O abundances (poorly constrained) were too small (e.g., *Forget et al.*, 2009; *Huestis et al.*, 2008). MGCM-MTGCM simulations conducted with enhanced O abundances (150% of presently accepted values) (Simulation 7), result in cooler temperatures by ∼5-10 K (not shown). Presumably, higher O abundances would yield even further cooling. The heavily debated uncertainty of the heating efficiency for the middle and upper atmosphere of Mars (e.g., *Fox et al.*, 1995; *Bougher et al.*, 2008) hinders the viability of using GCM calculations to constrain O abundances. Instead, nightside atomic O measurements are needed, which can then constrain CO_2 cooling rates.

The preliminary inter-model comparison results presented here indicate that the thermal balances calculated in both the MGCM-MTGCM and the LMD GCM may be missing some important physical process(es) that is (are) preventing both models from reproducing the mesopause temperature and altitude observed on the nightside at southern tropical latitudes during southern winter. As described above, in the case of the MGCM-MTGCM, this may be due to global winds that are too strong. We suggest that these winds may be modified with the incorporation of gravity wave

effects into the MGCM-MTGCM, which would serve to weaken the global winds and therefore decrease the magnitude of the nightside dynamical heating terms.

Finally, winter polar warming signatures cannot be identified in the present study due to sparse data coverage at high latitudes.

CHAPTER III

A Characterization of Middle-Atmosphere Polar Warming at Mars and Middle-Atmosphere Constraints for GCMs

3.1 Context and Objectives

Polar warming (PW) is a poorly characterized feature of the martian atmosphere. It consists of a temperature enhancement over mid-to-high latitudes during winter, spring, and fall, resulting in a reversal of the meridional temperature gradient expected from radiative equilibrium alone .

PW at Mars is in some ways similar to the reversal of the meridional temperature gradient observed in the terrestrial atmosphere above $\sim$ 70 km during solstices (*Holton*, 1982). In the terrestrial case, the winter-pole mesopause is 70-80 K warmer than the summer-pole mesopause (*Holton*, 1982). This reversed meridional temperature gradient is maintained dynamically through the thermally direct global circulation that has ascent and adiabatic cooling over the summer polar region and subsidence (adiabatic warming) over the winter polar region, as first theorized by *Kellogg and Schilling* (1951). In the martian case, the global mean meridional circulation is a thermally direct response to the diabatic forcings caused by: (a) differential insolation, and (b) absorption of solar infrared radiation by suspended dust (*Schneider*,

1983; *Wilson*, 1997; *Forget et al.*, 1999), which tends to be preferentially distributed over southern latitudes. Based on model simulations, *Santee and Crisp* (1993) predicted a meridional circulation for the martian mesosphere similar to that proposed for the terrestrial mesosphere by *Leovy* (1964), namely ascending air at low latitudes, poleward flow above 40 km altitude, and subsidence over the poles. Simulations by *Wilson* (1997) and *Forget et al.* (1999) determined that angular momentum is not conserved at mid- to high latitudes. Later *Hartogh et al.* (2005) and *Medvedev and Hartogh* (2007) showed that the middle atmosphere circulation away from low latitudes is maintained by eddy forcing. Recently, *McCleese et al.* (2008b) proposed two seasonal circulation patterns (Figure 3.1) to explain the two thermal structure modes (solstitial and equinoctial) found in MCS observations (see Figure 1.13). Notably, both of the proposed circulations feature a descending branch that slants poleward with height. *Kuroda et al.* (2009) demonstrated that during dust storms this poleward extension of the meridional circulation is driven almost equally by thermal tides, planetary waves, and resolved gravity waves.

PW was first detected at Mars by *Deming et al.* (1986) through ground-based spectroscopy observations of the disk spanning $\sim$ 50-80 km altitude. These observations importantly permitted the first identification of this phenomena at Mars. Subsequent ground-based and spacecraft observations (e.g., *Smith et al.*, 2001) have added important information. They have not, however, provided the spatial nor the temporal resolution needed to characterize the details of PW at Mars.

Consequently, several important aspects of martian PW climatology remain unknown. One aspect that is unknown is its spatial location. Vertically, where does PW manifest? How does the vertical range of PW vary? Latitudinally, where does PW occur? How does the latitudinal range of PW vary with pressure and season?

Another aspect of PW that is un-characterized is its magnitude. What is the typical maximum magnitude of PW? How does the maximum PW magnitude vary

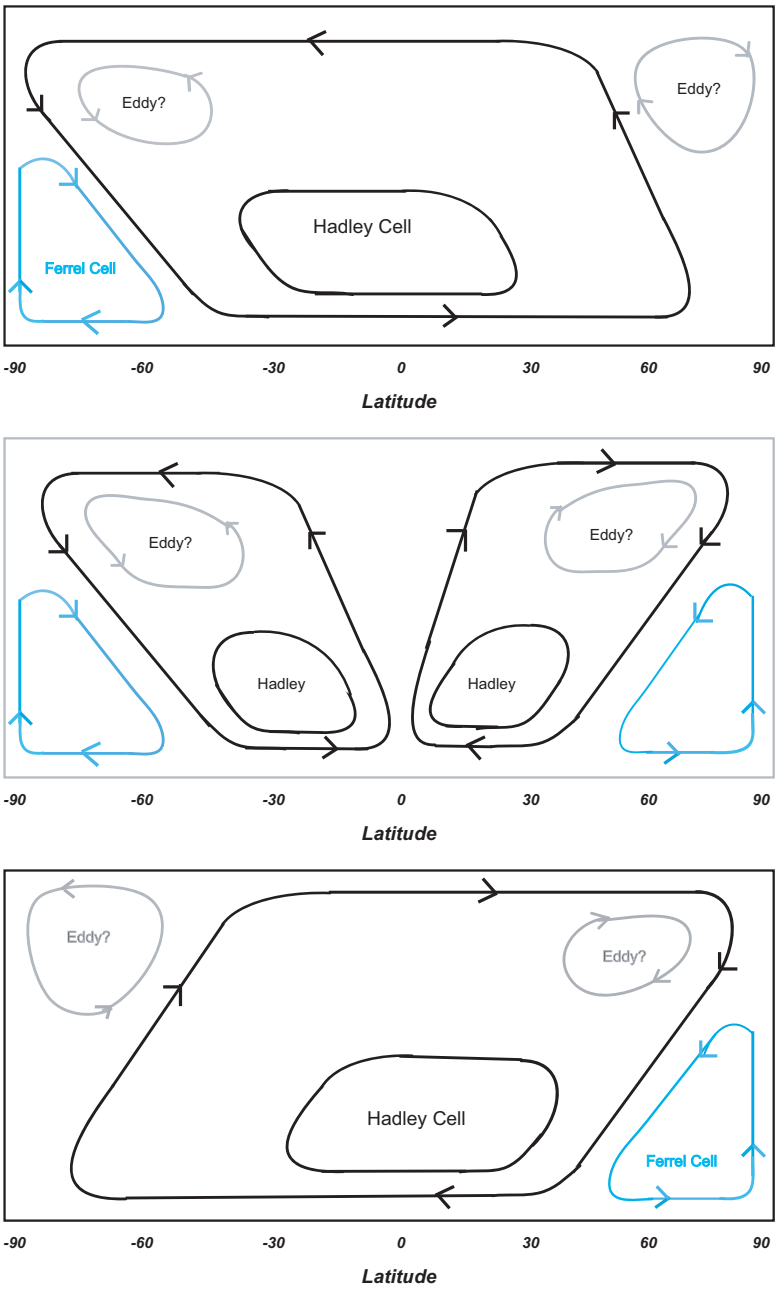

Figure 3.1: Mean meridional circulations suggested by previous investigators for: southern winter (top), equinox (middle), and northern winter (bottom). (Adapted from *McCleese et al.*, 2008b).

with LT? How does it vary with hemisphere and season? At what pressure does PW magnitude maximize vertically? How does the pressure at which PW maximizes vary with LT? How does it vary with season?

Fortunately, in the past 14 years, several spacecraft-based datasets have been collected that can be used to address the questions above. Instruments that sample a variety of atmospheric quantities have orbited or are presently orbiting the planet, compiling an aggregate of data applicable to these problems. The MCS dataset (see Section 3.3.1), in particular, provides an unprecedented wealth of information about the thermal structure of the lower and middle atmosphere (from the surface to ∼80-90 km). Four other datasets (from SPICAM and from the accelerometer (ACC) that flew on NASA's MGS, ODY, and MRO missions) extend the thermal record upward into the lower thermosphere. Taken together, these five datasets sample the thermal structure of the martian atmosphere from near the surface (p ∼600 Pa) to heights of 160 km (p ∼1x10^{-6} Pa), around the globe, over all seasons during several martian years at various positions in the solar cycle. The coverage afforded by these datasets makes it now possible to address the outstanding climatological questions raised above. Reporting a quantitative climatology of the PW phenomenon is the first objective of this study.

The present study is intended to describe the PW observed in these datasets. Any ideas shared about possible reasons for the trends described here are simply for the sake of discussion and not intended to conclusively diagnose the processes responsible for generating the observed trends. Rather the results presented here are intended to make a modeling study with that aim (diagnosing the processes responsible for the trends observed) feasible and well-constrained by the available observations.

As such, the second objective of this study is to provide constraints for numerical calculations of atmospheric fields in the middle atmosphere (p = 10 to 1x10^{-4} Pa, corresponding roughly to 30 to 120 km altitude). Numerical models are powerful

laboratories for atmospheric science. For example, they are typically used to interpret and synthesize existing datasets and provide predictions of quantities not yet observed. In order to be entrusted with these applications, models must be validated and constrained as best possible. That is, they must: (a) reliably reproduce observed atmospheric fields and their spatial and temporal variations, and (b) limit solutions to unobserved quantities to values physically reasonable given observed quantities. In the case of the middle-atmosphere, observations of PW can be used to: (a) validate modeled temperature fields and their spatial and temporal variations, and (b) constrain modeled winds and global circulation patterns (not directly observed).

Since mass, momentum, and energy can be transported across the entire atmosphere, GCMs of the atmosphere need to support such transport as well and therefore must be validated and constrained in all regions of the atmosphere. Observations of (and constraints for) the lower atmosphere (p >1 Pa, corresponding roughly to heights <50 km) and upper atmosphere (p <1x10^{-4} Pa, corresponding roughly to $\sim$ 120 km altitude up to the exobase) are comparatively plentiful and several whole-atmosphere models have been validated and constrained accordingly (*González-Galindo et al.*, 2009a,b; *Moudden and Forbes*, 2008; *Richardson et al.*, 2007; *Pawlowski et al.*, 2010; *Bougher et al.*, 2011b). Until now, however, multidimensional models of the martian atmosphere have experienced a pronounced shortage of constraints for their middle-atmosphere calculations, save those provided by the SPICAM datasets (*Forget et al.*, 2009; *McDunn et al.*, 2010). As noted by *Hartogh et al.* (2007), this shortage of middle-atmosphere observations makes it impossible to validate modeled polar warmings. It also limits confidence in calculations of unconstrained fields, such as winds. In response to this need, the final contribution of this chapter is a set of tabulated MCS temperatures for the validation and constraint of GCM middle-atmosphere calculations.

In Section 3.2, we define a metric for quantifying PW. In Section 3.3, we describe

the MCS, SPICAM, and ACC temperature datasets. In Section 3.4, we describe our data averaging strategy. In Section 3.5, we present the PW quantification results and discuss the observed middle-atmosphere PW, including its spatial, diurnal, seasonal, and interannual trends and variabilities. In Section 3.6, we present quantitative constraints for GCM middle-atmosphere calculations. Finally, in Section 3.7, we summarize the findings from this work.

3.2 Quantitative PW Index

To date, a community-wide quantitative metric of martian PW has not existed. Metrics previously employed, and the concept of PW they produced, have been limited by the amount and resolution of the data available. For example, early studies (*Deming et al.*, 1986) were limited to ground-based observations of the Mars disk over 50 to 80 km altitude and consequently were restricted to examining the inter-hemispheric (pole-to-pole) temperature difference at solstices. As higher-vertical resolution information became available, vertical temperature inversions over high-latitudes were examined (*Théodore et al.*, 1993; *McCleese et al.*, 2008a). As 3-D GCMs (providing much higher-resolution "sampling" of their simulated atmospheres than any existing instrument) have been invoked, the concept of PW has evolved further and is now thought of as a reversal of the latitudinal temperature gradient expected from radiative equilibrium considerations alone (*Wilson*, 1997; *Forget et al.*, 1999; *Medvedev and Hartogh*, 2007; *Bougher et al.*, 2006; *Forget et al.*, 2009; *González-Galindo et al.*, 2009a,b). Temporal sampling has also affected the concept of PW, initially causing it to be understood as strictly a winter solstice phenomenon, referred to in the literature as "Winter Polar Warming (WPW)." In fact, PW is not confined to winter latitudes but also manifests during equinoxes over both hemispheres, as first modeled by *Forget et al.* (1999) and later observed by *Smith et al.* (2001) and *McCleese et al.* (2010).

Given the wealth of data and the high resolution afforded by the MCS dataset

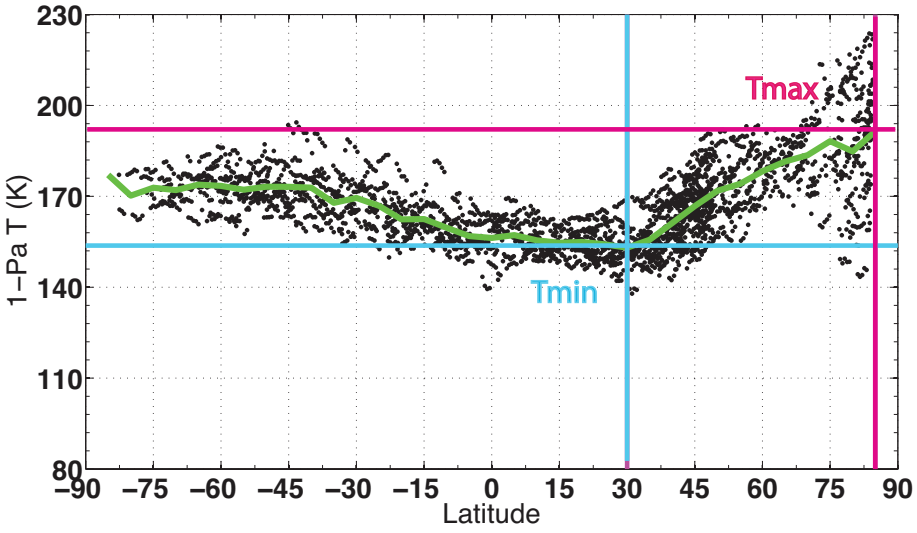

Figure 3.2: Example demonstrating the procedure for computing the metric defined in Equation 3.1. The black points represent individual MCS observations on the $p = 1$ Pa surface during this northern winter season. The green curve corresponds to the longitudinally averaged temperatures. First, T_{max} is located (indicated by the red lines). Then, moving equatorward from Lat_{Tmax}, T_{min} is identified (indicated by the blue lines). $\Delta_p T$ values are then calculated for T_{Lat} (points on the green curve between Lat_{Tmax} and Lat_{Tmin}).

(see Section 3.3), it is now possible to quantitatively characterize middle-atmosphere PW over nearly 3 martian years. For this task we have chosen the following metric to quantify the PW in each hemisphere on each pressure surface

$$\Delta_p T = (T_{Lat} - T_{min})_p, \tag{3.1}$$

where T_{Lat} is the longitudinally averaged temperature (see Section 3.4) at latitude Lat on pressure surface p, and T_{min} is the minimum longitudinally averaged temperature equatorward of the maximum longitudinally averaged temperature, T_{max} (Figure 3.2). Other formulations which are possible and have been used for a warming metric

include

$$\Delta_p T = (T_{max} - T_{equator})_p, \tag{3.2}$$

where $T_{equator}$ is the longitudinally averaged temperature at the equator,

$$\Delta_p T = (T_{winter\,pole} - T_{summer\,pole})_p, \tag{3.3}$$

where $T_{winter\,pole}$ and $T_{summer\,pole}$ are the longitudinally averaged temperatures at the winter and summer pole, respectively,

$$\Delta_p T = (T_{max} - T_{fixed\,latitude})_p, \tag{3.4}$$

where $T_{fixed\,latitude}$ is the longitudinally averaged temperature at a fixed chosen latitude, and the meridional gradient of the longitudinally averaged temperature over the latitudes of enhanced temperature

$$\nabla_p T = \frac{(T_{max} - T_{min})_p}{(Lat_{Tmax} - Lat_{Tmin})_p}. \tag{3.5}$$

The advantages of Equation (3.1) are that it: (1) indicates the magnitude of the dynamically enhanced temperatures as a function of pressure and latitude, (2) provides a quantitative constraint for modelers, (3) suggests the poleward extent of the descending branch of the mean meridional cell at each pressure (i.e., Lat_{Tmax}), (4) is not inherently biased toward identifying higher magnitude-PW at equinoxes (which would occur with Equation (3.2), for instance), or at solstices (which would occur with Equation (3.3), for instance), and (5) is easily comparable to definitions used in recent studies (*Bougher et al.*, 2006; *Hartogh et al.*, 2007; *Forget et al.*, 2009; *González-Galindo et al.*, 2009a,b). Disadvantages of Equation (3.1) are that it: (1) does not readily lend itself to comparison with the quantifications of PW employed in early studies (e.g., *Deming et al.*, 1986; *Théodore et al.*, 1993) (which could be

achieved with Equation (3.5)), and (2) offers no obvious indication of the strength of the mean meridional circulation (which might be obtainable from using Equation (3.3) during solstices and Equation (3.2) during equinoxes, for instance). Despite these disadvantages, we believe Equation (3.1) to be the most illustrative and useful metric for our objectives.

3.3 Temperature Datasets from p = 10 to 1x10^{-4} Pa from Spacecraft

In most planetary studies, overlap of separate instrument datasets is uncommon. Studies of the martian middle atmosphere are no exception. Differences in observation technique, orbit, and mission timing lead to differences in the observed spatial domain, spatial resolution, diurnal phase, seasonal phase, and solar cycle phase. In a very real sense, each instrument observes a distinctly different atmosphere. These factors significantly limit the ability to perform meaningful cross-dataset comparisons. Table 3.1 shows the nominal coverage afforded by the (independent) datasets used in this study. There is little vertical overlap by these datasets (MCS and SPICAM overlap between pressures of 1x10^{-1} and 1x10^{-3} Pa and SPICAM and the accelerometers overlap between pressures of 1x10^{-3} and 1x10^{-4} Pa), but there is substantial latitudinal overlap. There is no temporal overlap, as each dataset observes a different MY. However, there is seasonal overlap and comparisons across datasets can be made with the recognition that they observed during different years.

Our primary tool for characterizing middle-atmosphere PW is the MCS dataset. Where available, the other four datasets ("auxiliary datasests"), having the virtue of extending the thermal record above the vertical range of MCS, are used to augment the primary investigation, with due attention given to the fact that the sampled atmospheres in some way differ from that sampled by MCS.

Table 3.1: Nominal domains for the temperature datasets used in this study.

Instrument	# Profiles	MY	L_s (°)	F10.7-cm at Earth	local time (LT) (hours)	Latitude (°N)	Pressure (Pa)
MCS	>2e+6	28-30	0-360	70-110	1-5 13-17	-85 to 85	1e+1 to 4e-3
SPICAM	616	27	0-360	70-130	mostly 18-06	mostly fall and winter	1e-1 to 1e-4
MGS-ACC-1	∼200	23	180-300	70-90	11-18.5	35 to 6	1e-3 to 1.26e-4
MGS-ACC-2	∼600	24	30-95	130-150	17-15 1-2	50 to -80 -80 to -30	1e-3 to 1.26e-4
ODY-ACC	∼300	25	260-310	175-200	18-17 2-3	70 to 80 80 to 20	2e-3 to 1.26e-4
MRO-ACC	∼450	28	35-109	80-100	20-18 2-3	-80 to -85 -80 to 12	2e-3 to 1.26e-4

3.3.1 MCS

The MCS instrument is a passive infrared radiometer that measures thermally emitted radiation in both limb and on-planet geometries. From these measurements, vertical profiles of pressure and temperature are retrieved using a modified Chahine method and the Curtis-Godson approximation (*Kleinböhl et al.*, 2009, 2011). MCS obtains measurements at ∼20 altitudes per instantaneous field of view (i.e., per profile). Retrieved pressures and temperatures are then interpolated to a consistent set of 105 pressure levels ranging from near the surface up to 4.8 x 10^{-3} Pa (∼80-90 km altitude). The highest altitude at which pressures and temperatures are retrieved (hereafter referred to as the profile's "topside") depends on pointing (i.e., which part of the atmosphere is covered by the MCS detector array) and on temperature at high altitudes (corresponding to signal-to-noise). During MY 28, L_s = 181-258°, a pointing restriction prevented MCS from tracking the limb, resulting in lower-than-usual topsides (∼ 50 km altitude) over southern latitudes and higher-than-usual topsides (∼ 90 km altitude) over northern latitudes. The depth to which pressure and temperature retrievals (limb only) are possible depends upon atmospheric opacity. However, in the latest version of the retrieval (Version 3), which is used for this study, on-planet views can be simultaneously retrieved with limb views and, if an on-planet view is available, the temperature profile typically reaches down to the surface. The vertical

resolution of the individual retrievals is ∼5 km with uncertainties on the order of 2 K (*Kleinböhl et al.*, 2009, 2011).

Version 3 of the MCS temperature retrievals incorporates three major improvements over Version 1. The first improvement, as mentioned above, is the use of on-planet views, when available, in conjunction with limb views to compute surface temperature. This has two effects, namely eliminating the overly-cold surface temperatures found in previous versions of the retrieval, and permitting retrievals down to the surface where on-planet views are available. The second improvement is a less-restrictive criteria for opacity along the line of sight. This results in improved coverage during dusty conditions at the expense of higher-altitude bottom-sides on the retrievals during these periods. The third improvement is the inclusion of full scattering in the radiative transfer code (*Kleinböhl et al.*, 2011). This improves the accuracy of the retrievals, particularly during dusty conditions.

MRO entered its science-phase orbit on 24 September 2006 (MY 28, $L_s = 111°$). MCS has operated nearly continuously since then and, in its 2.5 martian years of operations so far, has accumulated more than 2 million profiles. Sparse coverage during the dust seasons (Figure 3.3a), particularly during the global dust storm of 2007 (MY 28, L_s = 265-300°), is due to airborne dust obscuring the instrument's view. Global dropouts (e.g., MY 28, L_s = 165-180°) are the result of instrument stowing, which led to limb-staring, which in turn led to inferior calibration. The sun-synchronous nature of MRO's orbit determines that MCS repeatedly observes the atmosphere at two local times (3 AM and 3 PM), except near the poles, where the LT observed varies rapidly as the spacecraft passes over the pole itself (Figure 3.3b). MCS observes nearly all latitudes during each orbit and the longitude observed varies as the planet rotates beneath the orbiter.

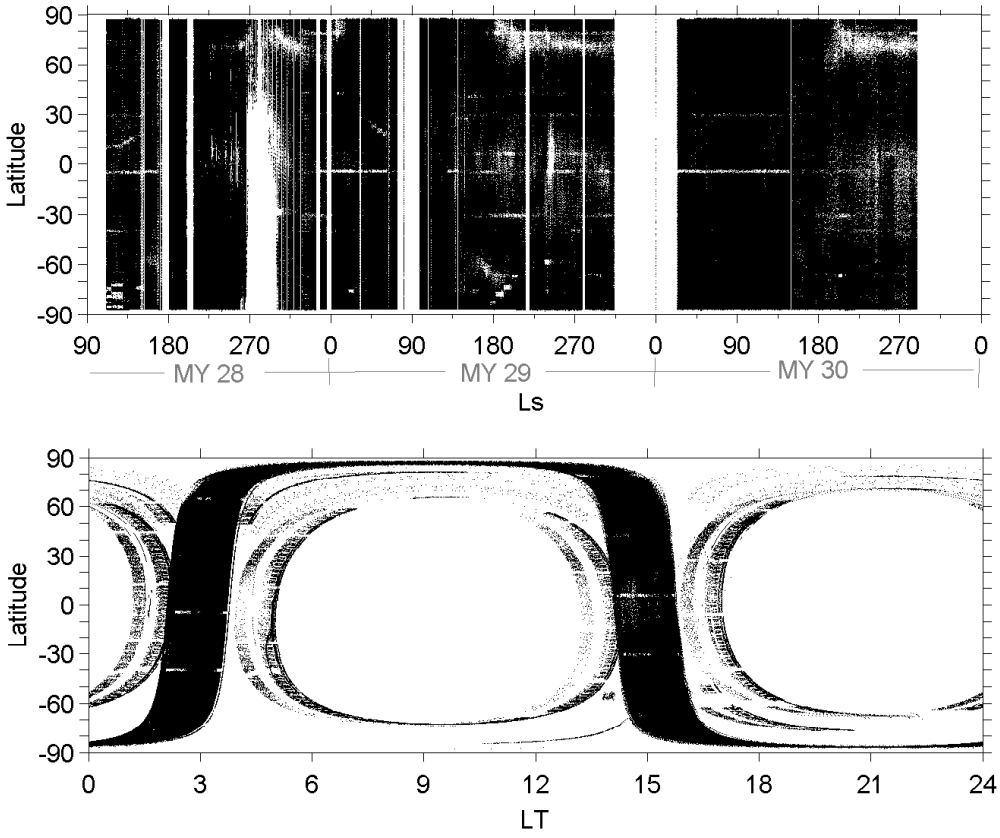

Figure 3.3: Seasonal (top) and local time (bottom) distribution of MCS Version 3 temperature retrievals.

3.3.2 SPICAM

The SPICAM instrument and its datasets are described in Section 2.2. The only difference is that in this study we consider SPICAM temperature retrievals (based on the assumed 175 K top temperature) between p = 1 x 10^{-1} Pa and 1x10^{-4} Pa ($\sim$70-120 km altitude), so as to avoid introducing confusion from the assumed top temperature.

3.3.3 Accelerometers

Fortunately for atmospheric science, aerobraking campaigns at Mars (MGS, ODY, and MRO) not only served their operational function of circularizing the spacecraft's highly elliptical capture orbit into one more favorable for science mapping, they also provided, for the first time, systematic *in situ* observations of the lower thermosphere (*Keating et al.*, 1998, 2003; *Tolson et al.*, 1999, 2000, 2005, 2008; *Bougher et al.*, 1999b, 2006; *Withers et al.*, 2003a,b; *Withers*, 2006). The accelerometers utilized in aerobraking operations archived *in situ* measurements of deceleration at: (a) periapsis (the pressure and altitude of which vary from one orbit to the next), (b) a reference pressure (1.26 nbar), and (c) 10-km altitude increments on the inbound and outbound legs of each orbit. Neutral density and neutral density scale heights were derived from these deceleration measurements. Using the derived density scale heights and the procedure described by *Withers* (2006), we calculate neutral temperatures on a pressure coordinate. For simplicity, in these calculations we assume a uniform mean molecular mass, μ = 43.49 Daltons (*Magalhães et al.*, 1999; *Withers*, 2006). Independent calculations from the MTGCM (see Section 2.3) of μ for the conditions of the various aerobraking operations (see Table 3.1) provide confidence that this assumption is reasonable for $p \geq$ 1.26 nbar, except within 10° of the pole. Therefore, we restrict our considerations of ACC-derived temperatures to $p \geq$ 1.26 x 10^{-4} Pa ($\leq$ 120 km altitude).

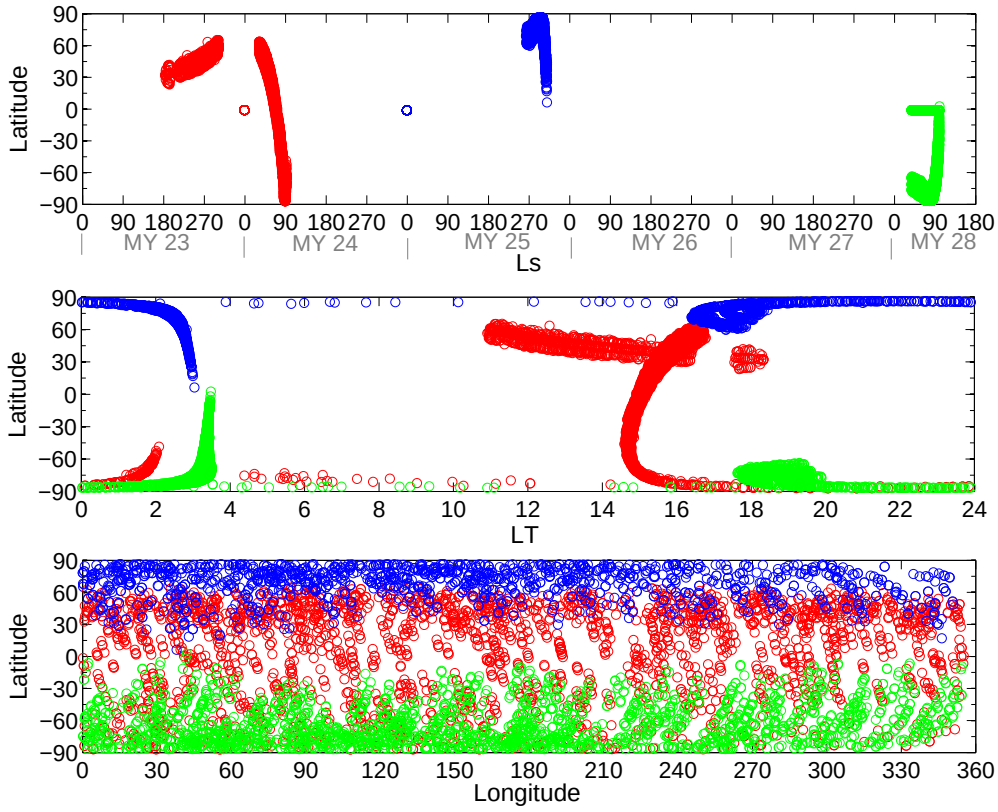

Figure 3.4: Seasonal (top), local time (middle), and horizontal (bottom) distribution of accelerometer-derived temperatures at p >1.26 nbar. Red points represent MGS-ACC observations, green points represent ODY-ACC observations and blue points represent MRO-ACC observations.

The accelerometers on each aerobraking spacecraft sampled the lower thermosphere at different latitudes, LTs, seasons, and years (see Table 3.1). Taken together ∼1500 orbits were obtained, sampling nearly all latitudes. The sampling afforded at $p \geq 1.26\text{x}10^{-4}$ Pa is shown in Figure 3.4. MGS/ACC sampled southern winter, northern summer, northern fall, and northern winter, while ODY/ACC sampled northern winter, and MRO/ACC sampled southern winter (Figure 3.4 top frame). Most ACC observations sampled the nightside, though some MGS/ACC observations sampled the dayside (Figure 3.4 middle frame). MGS/ACC sampled mid-northern latitudes, tropical latitudes, and southern latitudes, ODY/ACC sampled high-northern latitudes, and MRO/ACC sampled southern latitudes (Figure 3.4 bottom frame).

3.4 Data Averaging

Prior to calculating the polar warming metric from the observed temperatures, we consolidate the data on each pressure surface by longitudinal averaging. We begin by binning temperatures according to cardinal seasons (i.e., L_s=0 $\pm$ 5°, 90 $\pm$ 5°, 180 $\pm$ 5°, and 270 $\pm$ 5°) and LT ("nightside" = 0100 to 0500, "dayside" = 1300 to 1700). Auxiliary temperatures are binned in broader LT bins ("nightside" = 1900 to 0500 and "dayside" = 0700 to 1700), in order to improve the sampling. We further bin the temperatures on each pressure surface by latitude (0° $\pm$ 2.5°, 5° $\pm$ 2.5°, etc.) and then average the temperatures in each bin. Longitudinally averaged temperatures with propagated error $\geq$ 7 K are discarded. This criterion is selected in accordance with the MCS temperature retrieval technique, which relaxes the profile to isothermal when the error exceeds 5% (*Kleinböhl et al.*, 2009) (typically this occurs near 80 km altitude, where the global-average temperature is approximately 140 K). The polar warming metric, $\Delta_p T$, is then calculated from the remaining bin-averaged temperatures. Any $\Delta_p T \geq 15$ K is considered to be a notable PW feature and is tabulated and plotted. The standard deviation for each bin describes the variability about the calculated mean and, therefore, quantifies how representative $\Delta_p T$ values calculated from that mean are of the range of $\Delta_p T$ values that could be computed from individual bin-component temperatures. The standard deviation is $<$ 15 K for all bins except a a few isolated bins during MY 28 northern winter whose standard deviation are as high as 25 K.

Figures showing the un-averaged temperatures and the longitudinally averaged curves produced by this technique are provided for each of the studied seasons in Appendix A. The longitudinally averaged temperatures are provided in tabular form in Appendix B.

3.5 PW Quantification Results and Discussion

Figures 3.5 and 3.9 provide a succinct picture of the structure of the observed PW, as diagnosed using Equation 3.1, and how it varies in space and time. Tabulated results are provided in Appendix C, as quantitative constraints for GCMs.

The discussion in Sections 3.5.1- 3.5.4 focuses on the nightside results (Figure 3.5). A summary of the differences found on the dayside is given in Section 3.5.5.

3.5.1 Vertical Range of PW

The vertical range of $\Delta_p T \geq 15$ K (hereafter, simply PW) varies with latitude, hemisphere, season, and MY. The greatest pressure at which PW manifests will be referred to as the bottom extent and the smallest pressure, the top extent.

During the typically benign dust year of MY 30 (Figure 3.6), the bottom extent of PW occurred between $p = 3$ to 7 Pa ($\sim$ 35 - 45 km altitude) and the top extent occurred between $p = 6$ x 10^{-2} to 8 x 10^{-3} Pa ($\sim$ 75 - 90 km altitude), depending on latitude and season (see Figure 3.5). Typically, the lowest bottom extent of PW occurred at middle latitudes (45 to 75°), with lower and higher latitudes exhibiting slightly higher bottom extents. The highest top extent of PW occurred at high latitudes and fell off toward lower latitudes. Typically, the bottom extent was slightly lower (i.e., PW manifested to slightly greater pressures) in the southern hemisphere than in the northern hemisphere, and the top extent was slightly higher (i.e., PW manifested to slightly smaller pressures) in the northern hemisphere than in the southern hemisphere. These top extents corroborate past modeling studies that found a model domain up to at least 90 km altitude was necessary to capture the full mean meridional circulation and simulate middle-atmosphere PW (*Wilson*, 1997; *Forget et al.*, 1999). In both hemispheres, the vertical range (bottom extent to top extent) of PW was broadest during the $L_s = 180°$ equinox followed by their respective local winters, and narrowest during the $L_s = 0°$ equinox.

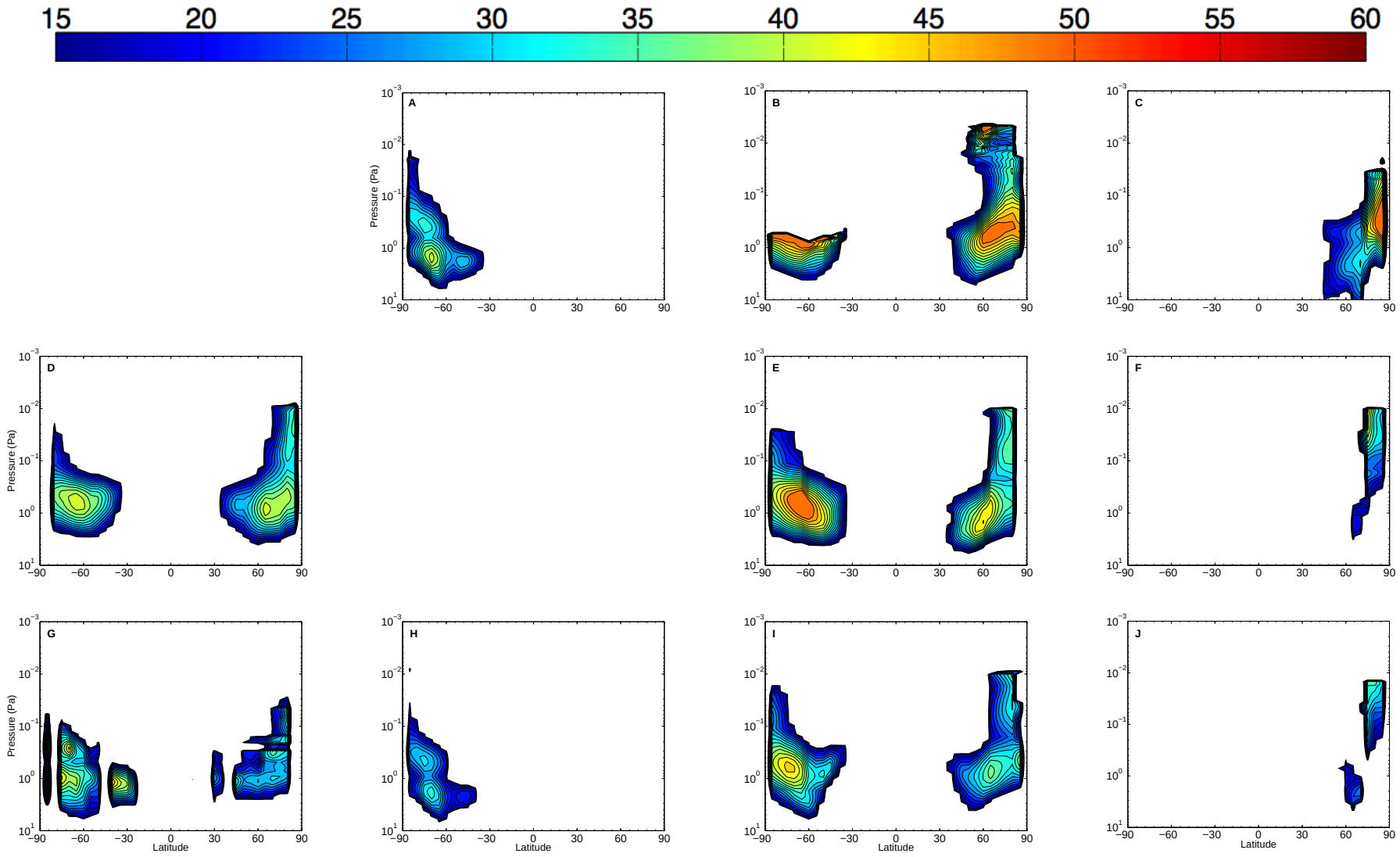

Figure 3.5: Pressure-latitude cross-sections of nightside PW ($\Delta_p T \geq 15$ K) at cardinal seasons. The colorbar is in K. Contours are drawn every 2 K, beginning at 15 K. The top row is MY 28, $L_s = 115°$, 180°, and 270° (A, B, and C, respectively). The middle row is MY 29, $L_s = 0°$, 180°, and 270° (D, E, and F, respectively). The bottom row is MY 30, $L_s = 0°$, 90°, 180°, and 270° (G, H, I, and J, respectively).

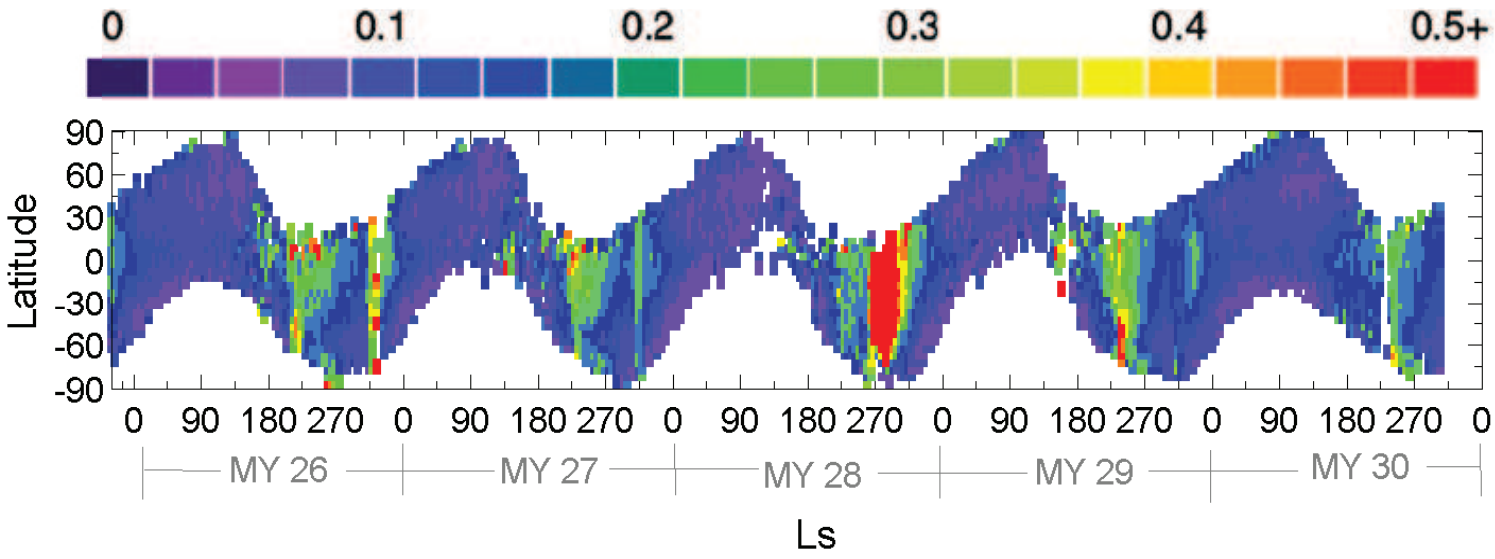

Figure 3.6: Dust optical depth (1075 cm^{-1}) scaled to 6.1-mbar surface from the THEMIS instrument onboard ODY. Purple is $\tau = 0.0$ and red is $\tau \geq 0.5$.

The bottom and top extents of PW at each season of other MYs were similar to those of MY 30. One exception to this occurred during MY 28, $L_s = 180°$. At this time the top extent in the northern hemisphere was $p = 5$ x 10^{-3} Pa (note that due to an instrument pointing restriction, southern hemisphere data did not extend to $p < 5$ x 10^{-1} Pa during this season, see Section 3.3.1). This apparent vertical expansion is most likely due to the extended vertical coverage over northern high latitudes during this period (see Section 3.3.1). The data coverage did not extend this high during any of the other seasons examined.

SPICAM and accelerometer temperatures reveal patches of PW (not shown, but tabulated in Appendix C) with top extents of $p = 1$x10^{-4} Pa during southern winter, northern winter, and in the northern hemisphere during $L_s = 180°$.

3.5.2 Latitudinal Range of PW

The latitudinal range of PW varies with pressure, hemisphere, season, and MY. The lowest latitude at which PW manifests will be referred to as the equatorward extent and the highest latitude, the poleward extent.

During MY 30, PW manifested between $\sim 30°$ and 80-85° latitude, depending on pressure and season (see Figure 3.5). At the greatest pressure of manifestation (i.e., at the bottom extent), PW occurred at middle latitudes (45° to 75°). The latitudinal range of PW expanded in both the poleward and equatorward directions with decreasing pressure during equinoxes and southern winter until reaching the pressure of broadest latitudinal extent, which generally occurred at greater pressure ($p = 4$ to 0.5 Pa) during the $L_s = 0°$ equinox and southern winter, and at smaller pressure ($p = 0.5$ to 0.3 Pa) during the $L_s = 180°$ equinox. With further decreasing pressure, the poleward extent of PW was maintained while the equatorward extent retreated poleward such that at $p < 0.1$ Pa PW rarely manifested below 60° latitude. Northern winter exhibited a different latitudinal structure, with both the poleward

and equatorward extents shifting only poleward with decreasing pressure (and never extending below 55° latitude at any pressure), resulting in a much narrower latitudinal channel of PW ($\sim$ 10°-20° in width at every pressure) than was exhibited during southern winter or in either hemisphere during either equinox. At each season, the shape of the PW channel as a function of pressure and latitude is suggestive of a descending branch that moves equatorward with increasing pressure (i.e., with the flow), in agreement with the circulation patterns proposed by *McCleese et al.* (2008a) (see Figure 3.1). In addition, the absence of high-latitude PW at the greatest pressures of PW manifestation supports *McCleese et al.* (2008a)'s theory of Ferrel cells over the high latitudes of each hemisphere (see Figure 3.1). Specifically, the latitudinal structure of the PW observed by MCS suggests the Ferrel cell over the northern winter pole is taller (i.e., extends to higher altitudes or smaller pressures) than that over either pole during other cardinal seasons (Figure 3.7).

The general latitudinal structure of PW at equinoxes and southern winter of other MYs was similar to that exhibited at those seasons of MY 30 (see Figure 3.5). The main difference is that the equatorward extension of PW persisted to smaller pressures (higher altitudes) before retreating during MY 28 and MY 29 equinoxes than during MY 30 equinoxes. The general latitudinal structure of PW at northern winter, on the other hand, showed more significant interannual variability. Specifically, MY 28 northern winter exhibited the equatorward extension, followed by retreat, with decreasing pressure that other seasons did, but that MY 29 and MY 30 northern winters did not, reaching latitudes as low as 45°. This suggests that whatever is responsible for suppressing the width of the PW channel during typical northern winters (i.e., those having regional but not global dust storms) is alleviated or overwhelmed during global dust storm conditions.

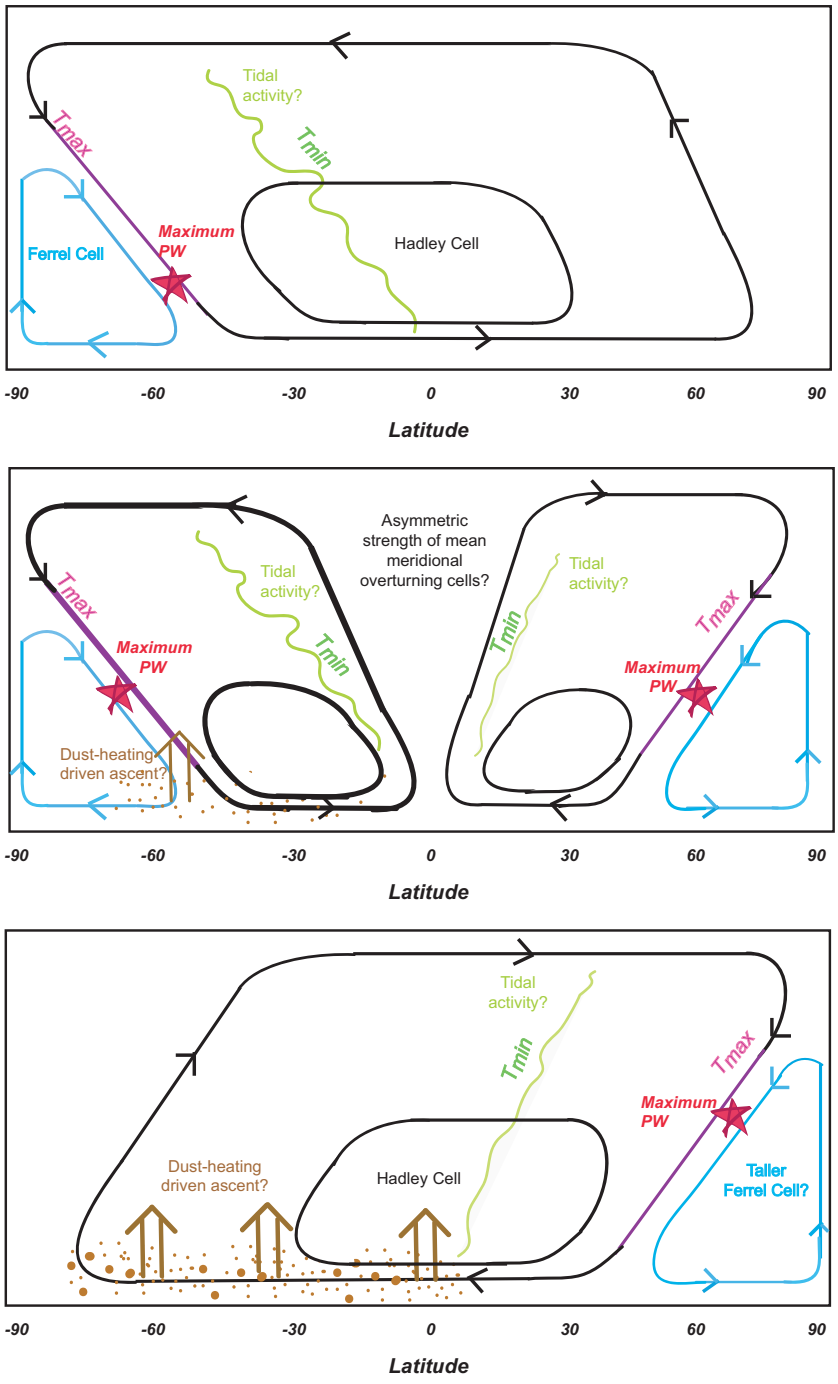

Figure 3.7: Forcings that may partially explain PW magnitude and location, for: southern winter (top), equinox (middle), and northern winter (bottom). These possible forcings include: (1) dust-heating driven ascent, which may strengthen the mean meridional circulation during northern winter and equinox, (2) stronger tidal activity in the southern tropics than the northern tropics, which may produce an equinoctial circulation that is asymmetric in strength, and (3) a taller Ferrel cell during northern winter than during other seasons. Modeling studies are needed to verify or refute these hypotheses.

3.5.3 PW Structure and Magnitude

The structure and magnitude of PW varied with pressure, latitude, hemisphere, season, and MY.

Each pressure surface exhibited a single maximum in PW magnitude (per hemisphere). This maximum typically occurred at middle latitudes at lower altitudes (p > 0.5 Pa) and moved poleward with height (see Figure 3.5).

In the southern hemisphere, the maximum PW on each pressure surface was larger during equinoxes than during local winter. In the northern hemisphere, the maximum PW on pressure surfaces greater than 0.1 Pa was larger during equinoxes than during local winter, whereas on pressure surfaces less than 0.1 Pa it was comparable at equinoxes and local winter.

During equinoxes, the maximum PW on pressure surfaces greater than 0.1 Pa was greater in the southern hemisphere than in the northern hemisphere. The reverse held true for pressure surfaces less than 0.1 Pa. This hemispheric asymmetry during equinoxes suggests asymmetry in the mean meridional circulation.

Low and middle latitudes ($< 60°$) exhibited one vertical maximum, typically between $p = 0.8$ Pa and 3 Pa (see Figure 3.5). High latitudes ($> 60°$), on the other hand, exhibited two vertical maxima (except during northern local winter) with the lower one (i.e., that at greater pressure) being of larger magnitude than the higher one. Typically these maxima occurred lower in the atmosphere ($p = 1$ to 3 Pa and $p = 0.3$ to 0.7 Pa) in the southern hemisphere than in the northern hemisphere ($p =$ 0.4 to 0.6 Pa and $p = 0.01$ to 0.08 Pa). During MY 28, Ls = 180°, when the pointing restriction (see Section 3.3.1) allowed observations of higher-than-usual altitudes, a third vertical maxima was detected around $p = 0.005$. Unlike at other cardinal seasons, during northern winter the high latitudes exhibited a single vertical maximum, typically between $p = 0.01$ Pa and 0.05 Pa.

3.5.4 Maximum PW

We define a season's maximum PW magnitude (hereafter, maximum PW) to be the largest $\Delta_p T$ value within the latitude-pressure domain of a given hemisphere. We can track the pressure, latitude, and magnitude of maximum PW to help characterize those components of the circulation that generate PW.

The pressure where northern-hemisphere maximum PW occurred varied from p = 0.005 to 1.5 Pa (see Figure 3.8 middle frame). In general, it occurred at greatest pressure ($p = 0.4$ to 1.5 Pa, corresponding roughly to 50-60 km altitude) during local fall and smallest pressure ($p \sim 0.01$ Pa, corresponding roughly to 85 km altitude) during local winter. A notable exception to this occurred during MY 28, $L_s = 180°$, when the maximum PW occurred at the smallest pressure of any season ($p = 0.005$ Pa). Once again, this anomaly must be caused by something other than dust-heating since there were no significant dust events at this time. Over the three martian years observed, the interannual variability of the pressure where northern-hemisphere maximum PW occurred was large for equinoxes (up to three orders of magnitude) and small for local winter (up to one order of magnitude). In general, the altitude where northern-winter maximum PW occurred is similar to what was modeled by *Forget et al.* (1999) ($\sim$ 50-70 km) and greater than was modeled by *Wilson* (1997) ($\sim$ 40 km).

The latitude where northern-hemisphere maximum PW occurred varied from 60° to 85° and exhibited no seasonal or interannual trends (Figure 3.8 bottom frame).

The value of northern-hemisphere maximum PW varied from 36 K to 55 K (Figure 3.8 top frame). In general, it was largest at local fall and local winter and smallest at local spring. The values of the northern-winter maximum PW are comparable to what was modeled by *Wilson* (1997) ($\sim$ 40 K) and smaller than what was modeled by *Forget et al.* (1999) ($\sim$ 70-80 K), while the values of the northern-equinoctial maximum PW are larger than was modeled ($\sim$ 15-25 K (*Forget et al.*, 1999)). Over

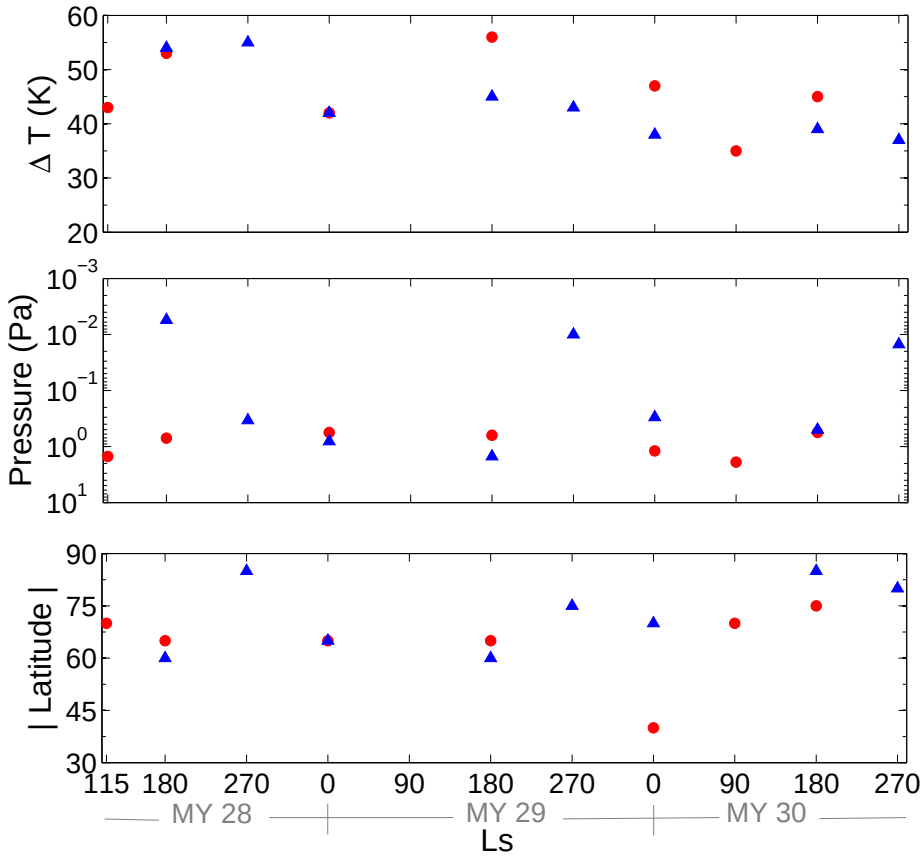

Figure 3.8: Features of nightside maximum PW: magnitude (top), pressure (middle), and latitude (bottom). Red circles represent southern-hemisphere features and blue triangles represent northern-hemisphere features.

the three martian years observed, the interannual variability of the value of northern-hemisphere maximum PW was large for local fall and local winter (up to 15-19 K) and small for local spring ($\leq$ 5 K), in qualitative agreement with the interannual variability of the dust optical depth (τ) for each of these seasons over this three year period (see Figure 3.6), suggesting that dust-heating driven ascent is a significant forcing mechanism for the dynamics that generate PW. Interestingly, however, the seasonal variability of the value of northern-hemisphere maximum PW is small within each of the three years observed ($<$ 5 K), despite the large seasonal variability of τ (up to 0.5) within each year, suggesting that additional forcings also play a significant part in determining the magnitude of maximum PW (e.g., Figure 3.7).

The pressure where southern-hemisphere maximum PW occurred varied from $p =$ 0.4 to 2 Pa (see Figure 3.8 middle panel). In general it occurred at greater pressure ($p = 2$ Pa, corresponding roughly to 45 km altitude) during local winter, and smaller pressure ($p = 0.7$ to 0.4 Pa, corresponding roughly to 55-60 km altitude) during local fall and local spring. Over the three martian years observed, the interannual variability of the pressure where southern-hemisphere maximum PW occurred was small (approximately half an order of magnitude) both at local winter and at equinoxes. The altitude where southern-winter maximum PW occurred was slightly smaller than what has been modeled ($\sim$ 50-80 km) (*Forget et al.*, 1999; *Medvedev and Hartogh*, 2007; *Hartogh et al.*, 2007).

The pressure where southern-hemisphere maximum PW occurred during any given equinox (except MY 28, $L_s = 180°$) was similar to that where northern-hemisphere maximum PW occurred, indicating that the shape of the equinoctial circulation was largely symmetric about the equator (see Figure 3.7). In contrast, the pressure where southern-winter maximum PW occurred was greater (by 1 to 2 orders of magnitude) than that where northern-winter maximum PW occurred, suggesting that the descending branch of the solstitial circulation penetrated to greater pressures during

southern winter than during northern winter.

The latitude where southern-hemisphere maximum PW occurred varied from 40° to 75° and exhibited no seasonal or interannual trends (see Figure 3.8 bottom panel).

The value of southern-hemisphere maximum PW varied from 34 K to 56 K. In general it was largest at equinox and smallest at local winter. The values of the southern-winter maximum PW are similar to what was modeled by *Medvedev and Hartogh* (2007) and *Hartogh et al.* (2007) ($\sim$ 40 K) and larger than what was modeled by *Forget et al.* (1999) ($\sim$ 10 - 15 K), while the values of the southern-equinoctial maximum PW are larger than was modeled ($\sim$ 15-25 K (*Forget et al.*, 1999)). Over the three martian years observed, the interannual variability of the value of southern-hemisphere maximum PW was small for local fall ($\leq$ 5K) and modest for local winter and spring (8-11 K). Similarly to the northern-hemisphere, this is in qualitative agreement with the interannual variability of τ for each of these seasons.

The value of southern-hemisphere maximum PW was comparable to that of northern-hemisphere maximum PW for the first two equinoxes observed. For subsequent equinoxes, the value of southern-hemisphere maximum PW was 7 to 14 K larger than that of northern-hemisphere maximum PW. The reason for this interannual variability is not clear, however the pattern of the later equinoxes observed does suggest a circulation pattern that is asymmetric in strength about the equator and has a stronger cell over the southern hemisphere (see Figure 3.7, middle panel). Greater tidal forcing in the southern tropics (*Bell et al.*, 2007; *Lee et al.*, 2009; *González-Galindo et al.*, 2009a,b) may partially explain such an asymmetry.

Comparing solstices, the value of the MY 28 northern-winter maximum PW was 12 K larger than that year's southern-winter maximum PW, in agreement with past studies that found that dust-heating is an important forcing in enhancing the dynamics that generate PW. Interestingly, the value of the MY 30 southern-winter maximum PW magnitude was comparable to the value of the northern-winter maximum PW,

providing further support for the hypothesis that additional forcings (beyond the enhanced circulation associated with dust-heating driven ascent) are also important in generating PW.

3.5.5 Diurnal Variability

The dayside PW features exhibited structure and trends similar to those described above for the nightside PW features (see Figure 3.9). The precise location and magnitude of maximum warming, however, differed from nightside to dayside.

The dayside southern-hemisphere maximum PW occurred at smaller pressure (by $\sim$ 0.3 to 1.2 Pa) than the nightside maximum PW. In contrast, the dayside northern-hemisphere maximum PW occurred at similar or greater pressure than the nightside maximum PW (by as much as 0.6 Pa).

The dayside southern-hemisphere maximum PW generally occurred at higher latitudes (by 5-15°) than the nightside maximum PW. A similar pattern was not found in the northern hemisphere.

The dayside southern-hemisphere maximum PW was generally smaller in magnitude than the nightside maximum PW (by 7-10 K during local fall and by 13-23 K during local spring) except during southern winter, when they were comparable. The dayside northern-hemisphere maximum PW was generally smaller than the nightside maximum PW (by 4-17 K) except during northern winter of MY30, when they were comparable. In both hemispheres, the largest night-day difference in maximum PW occurred the perihelion season (L_s = 180° - 270°).

3.5.6 Meridional Temperature Gradient

An alternate measure of PW that was used in early studies is the meridional temperature gradient, $\nabla_p T$ (see Equation (3.5)). In the MCS data, northern-hemisphere maximum $\nabla_p T$ ranged from 0.9 to 2.9 K/°. It was largest during local winter (1.5

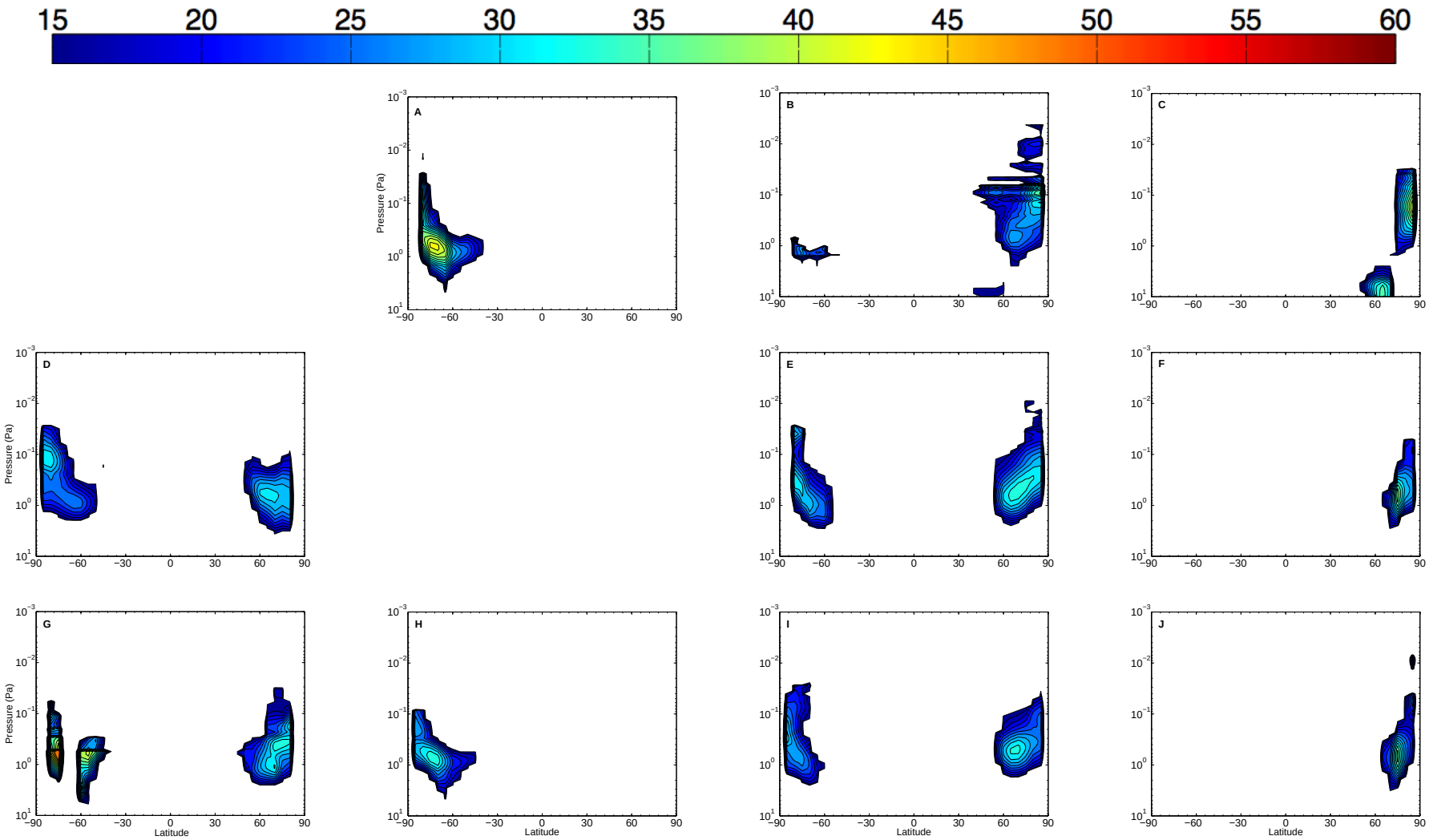

Figure 3.9: Same as Figure 3.5, for the dayside.

to 2.9 K/°), followed by local fall (0.9 to 2.1 K/°), and smallest during local spring (0.8 to 1.0 K/°). MCS southern-hemisphere maximum $\nabla_p T$ was smaller than that in the northern hemisphere and ranged from 0.3 to 1.0 K/°. It was largest during local spring and fall (0.6 to 1.0 K/°) and smallest during local winter (0.5 to 0.6 K/°). The southern-winter value observed by MCS is comparable to that found in ground-based observations for the 50-85 km altitude range (0.4 to 0.9 K/°) (*Deming et al.*, 1986). Moreover, the MCS southern-hemisphere maximum meridional gradient tended to occur at altitudes similar to the 50-85 km range observed by (*Deming et al.*, 1986), while the MCS northern-hemisphere maximum meridional gradient tended to occur higher in the atmosphere ($\sim$ 85-100 km).

3.6 Middle-Atmosphere Constraints for GCMs

Lookup tables containing the results of the longitudinally averaged MCS temperatures at 5° latitude intervals and half-decade intervals of log-pressure are provided in Appendix B. These tables can easily be used to validate middle-atmosphere GCM temperature calculations as well as constrain calculations of PW and the global circulation.

3.7 Summary

In this chapter we define a quantitative polar warming metric, apply it to nearly 3 full martian years of MCS temperatures as well as auxiliary temperatures from SPICAM and accelerometer datasets, and characterize how PW varies with pressure, hemisphere, LT, season and MY. In summary, we return to the questions raised at the beginning of this chapter:

Vertically, where does PW manifest? PW manifests between $p = 3$ - 7 Pa and $p =$ 6x10^{-2} to 5x10^{-3} Pa. How does the vertical range of PW vary with LT, season, and

martian year? PW manifests slightly lower in the atmosphere (greater pressures) in the southern hemisphere and slightly higher in the atmosphere (smaller pressures) in the northern hemisphere.

Latitudinally, where does PW occur? PW manifests between $\sim 30°$ and 80°-85° latitude. How does the latitudinal range of PW vary with latitude and season? During equinoxes and southern winter PW occurs at mid-latitudes at the greatest pressures of manifestation, and then expands in both the poleward and equatorward directions with decreasing pressure until reaching its broadest latitudinal extent (typically at a pressure between $p = 0.3$ and 4 Pa). Then, with further decreasing pressure the latitudinal range shrinks as the equatorward extent retreats poleward. During northern winter (except during a global dust storm), the latitudinal range of PW tends to remain very narrow (10-20° in width) and moves poleward with height.

What is the maximum PW magnitude? Maximum PW ranges from 32 to 56 K. How does the maximum PW magnitude vary with LT? It tends to be larger on the nightside than on the dayside (by up to 23 K), indicating stronger subsidence on the nightside. How does the maximum PW magnitude vary with hemisphere and season? During non-global dust storm years, maximum PW for each hemisphere tends to be greatest during $L_s = 180°$, suggesting the circulation is strongest during this season. Furthermore, in more than half of the equinoxes observed, southern maximum PW was larger than northern maximum PW, indicating asymmetry in the strength of the circulation during these equinoxes. Additionally, in the absence of global dust storm conditions, southern winter maximum PW tends to be comparable to northern winter maximum PW, suggesting that forcings other than the dust-heating enhancement of the mean meridional circulation may contribute to PW.

At what pressure does the PW magnitude maximize vertically? The pressure at which PW maximizes varies widely from $p = 1.9$ to 5.5 x 10^{-3} Pa. How does the pressure at which PW maximizes vary with LT? Generally, nightside maximum

PW occurs at similar pressures in the northern and southern hemispheres during equinoxes, and at greater pressures during southern local winter than during northern local winter (by one to two orders of magnitude). Southern maximum PW occurs at greater pressures on the nightside than on the dayside, and northern maximum PW occurs at smaller pressures on the nightside than on the dayside. How does the pressure at which PW maximizes vary with season? Southern maximum PW tends to be highest (smallest pressures) during local spring and lowest (greatest pressures) during local winter, while northern maximum PW tends to be highest during local winter (nightside) and local spring (dayside) and lowest during local fall.

CHAPTER IV

An Investigation into the Physical Mechanisms that Generate Middle-Atmosphere Polar Warming

4.1 Objective

The characterization of high latitude dynamical warming presented in the previous chapter begs investigation into the processes responsible for such departures from radiative equilibrium. Prior to the characterization of PW presented in Chapter 3, investigations into the forcings responsible for PW found that PW was produced in simulations of the middle atmosphere without needing to include momentum deposition from breaking gravity waves (*Wilson*, 1997; *Forget et al.*, 1999). As a result, these studies concluded that contributions by gravity wave momentum deposition (GWMD) were insignificant for producing PW, and that this phenomenon was driven primarily by the mean meridional circulation. Furthermore, since the mean meridional circulation is intensified by dust-heating during the perihelion season, these studies showed that PW should be stronger during the perihelion season than aphelion season (*Wilson*, 1997; *Forget et al.*, 1999). As shown in Chapter 3, however, this is not observed in the MCS dataset except in the case of a year having a global dust storm (GDS).

In this chapter we use the Mars Weather Research and Forecasting General Circulation Model (MarsWRF) GCM (*Richardson et al.*, 2007) to show that the mean

meridional circulation and its intensification with perihelion dust heating is indeed important for reproducing PW, but go on to demonstrate that the forcing produced by latitudinally and seasonally varying column dust opacity and a Conrath vertical distribution is not sufficient for capturing the precise magnitude and distribution of PW observed. We also demonstrate that GWMD is in fact important for reproducing the precise magnitude and distribution of PW and its evolution throughout the martian year, as initially suggested by *Barnes* (1990). In Section 4.2, we describe the MarsWRF framework and explain why this model is well-suited to the present study. In Section 4.3, we describe the different dust conditions employed for the numerical experiments performed in this study as well as the implementation of a gravity wave momentum deposition parameterization. In Section 4.4, using the MarsWRF model, we demonstrate the sensitivity of middle-atmosphere PW to the varying intensification of the mean meridional circulation caused by latitudinal and seasonal variations in horizontal dust opacity. We also introduce into the model a simple GWMD parameterization that captures the effect of topographically forced (stationary, phase speed = 0) gravity waves and allow them to propagate through, and deposit momentum in, the middle atmosphere. This scheme is adopted from the MGCM (see Section 2.3) where it has been tested (e.g., *Bougher et al.*, 2011a). With this added functionality, we demonstrate that the inclusion of GWMD refines the model's ability to reproduce the location, magnitude, and seasonal variability of the observed PW and therefore that GWMD is significant for the circulation and thermal structure of the middle atmosphere. Finally, in Section 4.5, we discuss the implications of these findings.

4.2 MarsWRF Framework

The MarsWRF GCM (hereafter, simply MarsWRF) is a 3-dimensional multi-scale model based upon the WRF model developed by NCAR, National Oceanic and Atmospheric Administration (NOAA), the United States Department of Defense

(DoD) and several universities for terrestrial weather forecasting and research. WRF was adapted to Mars by *Richardson et al.* (2007) and is employed as a finite-difference grid-point GCM for the global martian atmosphere from the surface to $\sim$ 120 km (e.g., *Johnson et al.*, 2008; *Guo et al.*, 2009, 2010; *Mischna et al.*, 2011; *McDunn et al.*, 2011). It can be applied to scales ranging from mesoscale to planetary. This is valuable for Mars, where local-to-global coupled dynamical processes can be important. For example, dust storms start as local disturbances and sometimes evolve into regional and even global storms. Another example of a local-to-global coupled dynamical process is gravity waves, which originate locally and have global effects.

The "Eulerian mass" grid-point dynamical core implemented in MarsWRF is that of the Advanced Research WRF, or WRF-ARW. It solves the flux form of the fully-compressible, conservative Euler equations (*Skamarock et al.*, 2008). Though the model is capable of solving the full nonhydrostatic equations, we follow the convention of using it in hydrostatic mode. The formulation of the equations solved will be presented in the next section.

The model's prognostic variables are the zonal wind, u, meridional wind, v, potential temperature, θ, and column-integrated mass per unit area, μ/g, where $\mu = p_{h\,sfc}$-$p_{h\,top}$, $p_{h\,sfc}$ and $p_{h\,top}$ are the hydrostatic component of the pressure at the surface and at the top of the domain, respectively, and g is the acceleration due to gravity (set to $g = 3.711$ m s^{-2}). The diagnostic variables are pressure, p, and inverse density, $\alpha = 1/\rho$, where ρ is the mass density.

The vertical coordinate is the terrain following mass coordinate defined by (*Laprise*, 1992)

$$\eta = \frac{p_h - p_{h\,top}}{\mu}, \tag{4.1}$$

where p_h is the hydrostatic component of the pressure. η equals 1 at the surface and decreases monotonically to 0 at the top of the domain. The vertical domain extends from the surface to p_{top}= 1 x 10^{-4} Pa (approximately 120 km altitude) and contains

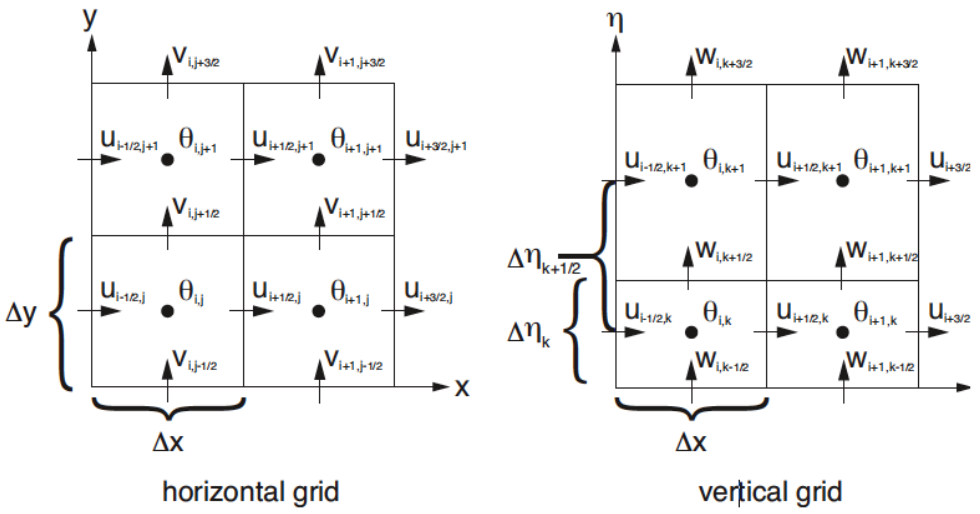

Figure 4.1: Schematic of the Arakawa-C grid spatial discretization used in MarsWRF. From *Skamarock et al.* (2008).

57 vertical layers (greater vertical resolution near the surface). In hydrostatic mode, η equates to the traditional σ coordinate (*Jacobson*, 1999).

The spatial discretization follows an Arakawa C-grid (*Arakawa and Lamb*, 1977) in which thermodynamic variables (e.g., θ, μ/g, and p) are stored at grid-box centers (i.e., *mass* points), and velocities are staggered by a half grid length (i.e., u, v, and w points, where $w = \mathrm{d}\eta/\mathrm{dt}$ is the vertical velocity) (Figure 4.1) (*Skamarock et al.*, 2008). The pole points (i.e., $\pm$ 90°) are v point singularities (Figure 4.2) and $v = 0$ at the pole always. Flux and gradients across the poles are disallowed by setting the grid volume face areas at the pole equal to zero (*Skamarock et al.*, 2008). Advection of material across the pole is achieved by zonal transport in the cells adjacent to the pole (*Richardson et al.*, 2007). For Coriolis and curvature term computations that require a value of v at the pole point (i.e., at the u and w points half a grid length from the pole), v is set equal to the value next to the pole point.

To maintain numerical stability, the timestep, Δt, is limited by the Courant-Friedrichs-Lewy (CFL) conditions $u\Delta\mathrm{t}/\Delta\mathrm{x}$ and $v\Delta\mathrm{t}/\Delta\mathrm{y}$ where Δx and Δy are the zonal and meridional grid lengths in computational space (km). Typical angular

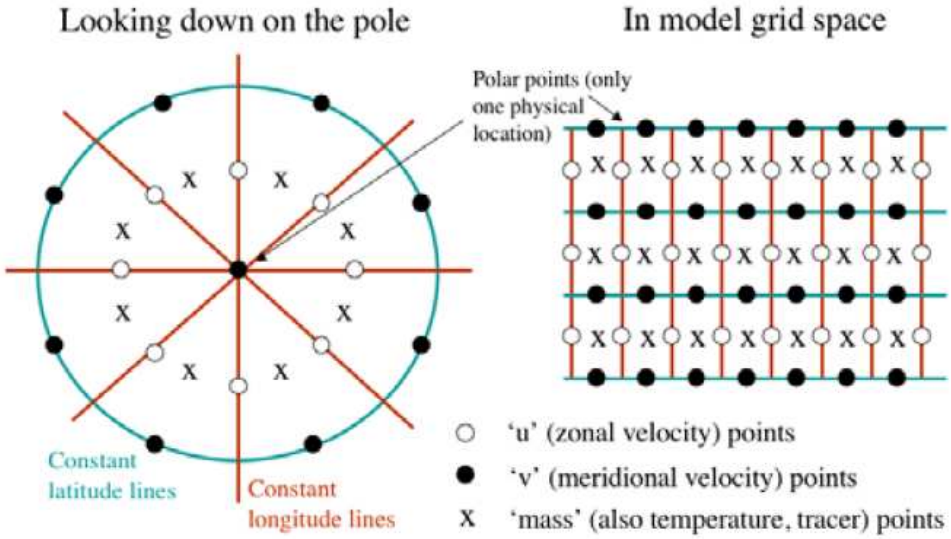

Figure 4.2: Schematic of the spatial discretization used for the polar region in MarsWRF. From *Richardson et al.* (2007).

resolution in computational space is 5° latitude x 5° longitude ($\Delta x \sim 300$ km, $\Delta y \sim 300$ km at the equator). *Richardson et al.* (2007) show that simulations with moderate resolution (5° x 5°) produce results not significantly different from those produced with high resolution (1.333° x 1.4°). Therefore, we run the model with moderate resolution so as to maximize the allowable timestep. This permits us to run the model with a 30 second timestep.

To maintain stability, a low-pass Fourier filter is applied to grid cells poleward of 45° to filter out high-frequency components of column mass, horizontal winds, temperature, and tracers. The wavenumber cutoff is a function of the cosine of latitude, ϕ (*Richardson et al.*, 2007)

$$\kappa_{max} = (N/2)\cos\phi, |\phi| > 45°, \tag{4.2}$$

where N is the number of points in the x direction ($N = 72$, for the resolution used in the present study).

4.2.1 Dynamical Formulation

The dynamical core solves the fluid dynamic conservation equations. The zonal and meridional momentum equations take the following formulations (*Richardson et al.*, 2007)

$$\frac{\partial}{\partial t}\left(\frac{\mu u}{g m_y}\right) = -m_x \frac{\partial}{\partial x}\left(\frac{\mu u}{g m_y} u\right) - m_x \frac{\partial}{\partial y}\left(\frac{\mu v}{g m_x} u\right) - \frac{1}{m_y}\frac{\partial}{\partial z}\left(\frac{\mu w}{g} u\right) - \frac{m_x}{m_y}\frac{\partial p}{\partial x} + \frac{\mu}{g m_y}\left(F_{u_{cor}} + F_{x_{phy}}\right), \tag{4.3}$$

$$\frac{\partial}{\partial t}\left(\frac{\mu v}{g m_x}\right) = -m_y \frac{\partial}{\partial x}\left(\frac{\mu u}{g m_y} v\right) - m_y \frac{\partial}{\partial y}\left(\frac{\mu v}{g m_x} v\right) - \frac{1}{m_x}\frac{\partial}{\partial z}\left(\frac{\mu w}{g} v\right) - \frac{m_y}{m_x}\frac{\partial p}{\partial y} + \frac{\mu}{g m_x}\left(F_{v_{cor}} + F_{y_{phy}}\right), \tag{4.4}$$

where F_{ucor} and F_{vcor} represent Coriolis and curvature forcing terms (see Equations 4.10 and 4.11), F_{xphy} and F_{yphy} represent turbulent mixing and parameterized physics (see Section 4.2.2), and

$$(m_x, m_y) = \frac{(\Delta x, \Delta y)}{\text{distance on Mars}}, \tag{4.5}$$

are the map scale factors. The conservation of energy equation solved by the model takes the form

$$\frac{\partial}{\partial t}\left(\frac{\mu T}{g}\right) = -m_x m_y \frac{\partial}{\partial x}\left(\frac{\mu u}{g m_y} T\right) - m_x m_y \frac{\partial}{\partial y}\left(\frac{\mu v}{g m_x} T\right) - \frac{\partial}{\partial z}\left(\frac{\mu w}{g} T\right) + \frac{\mu}{g}\left(F_A + F_D\right), \tag{4.6}$$

where T is temperature and F_A and F_D represent the adiabatic and diabatic heating rates, respectively. The conservation of mass equation takes the form

$$\frac{\partial}{\partial t}\left(\frac{\mu}{g}\right) = -m_x m_y \left[\frac{\partial}{\partial x}\left(\frac{\mu u}{g m_y}\right) + \frac{\partial}{\partial y}\left(\frac{\mu v}{g m_x}\right)\right] + \frac{\partial}{\partial z}\left(\frac{\mu w}{g}\right). \tag{4.7}$$

To diagnose hydrostatic pressure, the model uses the definition of the vertical coordinate (Equation 4.1). To diagnose the inverse density, the model solves the equation of state

$$p = p_0 \left(\frac{R_d \theta}{p_0 \alpha} \right)^{\gamma}, \tag{4.8}$$

where p_0 is a reference base pressure (set to 610 Pa), R_d is the gas constant (set to 191.17 $\mathrm{JK^{-1}kg^{-1}}$) and $\gamma = c_p/c_v = 4/3$ is the ratio of heat capacities at constant pressure and at constant volume (set to 764.7 $\mathrm{JK^{-1}kg^{-1}}$ and 573.53 $\mathrm{JK^{-1}kg^{-1}}$, respectively). Finally, to diagnose the geopotential, $\Phi = gz$, the hydrostatic equation is solved

$$\frac{\partial \Phi}{\partial \eta} = -\mu \alpha, \tag{4.9}$$

and w is diagnosed from the definition of the geopotential.

The Coriolis and curvature effects, treated in the right hand side of equations 4.3 and 4.4, are given by (*Skamarock et al.*, 2008)

$$F_{u_{cor}} = \frac{\mu}{g m_y} \left(fV + \frac{uv}{r} \tan\phi - \frac{uw}{r} \right), \tag{4.10}$$

$$F_{v_{cor}} = -\frac{\mu}{g m_x} \left(fu + \frac{u^2}{r} \tan\phi + \frac{vw}{r} \right), \tag{4.11}$$

where $f = 2\Omega \sin\phi$ is the Coriolis parameter, Ω is the planet's rotation rate (set to 7.08822 x 10^{-5} $\mathrm{s^{-1}}$), and r is the planet's radius (set to 3.38992 x 10^3 km).

Advection is solved in the model as a flux divergence (the first three terms on the RHS of Equations 4.3, 4.4, and 4.6). In order to calculate this, the value of the advected variable is needed at the locations where the advecting winds are stored. To obtain this, an interpolation is used (2^{nd} - 6^{th} order, selected at runtime) (*Skamarock et al.*, 2008). For horizontal advection we use a 5^{th} order upwind-biased interpolation, illustrated here with the generic scalar q. The index $i \pm 1$ denotes the value of q stored

at a *mass* point and $i \pm 1/2$ denotes the value of q interpolated to the u or v point (as needed, depending on the wind component doing the advecting). In other words, for advection by u, an x-direction interpolation is applied to obtain q at the u points (e.g., $q_{i-1/2}$) and for advection by v, a y-direction interpolation is applied to obtain q at the v points (e.g., $q_{j-1/2}$) (*Skamarock et al.*, 2008)

$$\begin{aligned} q_{i-1/2} = \frac{37}{60}\left(q_i + q_{i-1}\right) - \frac{2}{15}\left(q_{i+1} + q_{i-2}\right) + \frac{1}{60}\left(q_{i+2} + q_{i-3}\right) + \\ \text{sign}\left(u\right)\frac{1}{60}\left[\left(q_{i+2} - q_{i-3}\right) - 5\left(q_{i+1} - q_{i-2}\right) + 10\left(q_i - q_{i-1}\right)\right], \end{aligned} \tag{4.12}$$

where sign (u) denotes the sign of the zonal wind component. For vertical advection, we use a 3^{rd} order upwind-biased interpolation to obtain the value of q at the w points (e.g., $q_{k-1/2}$)

$$\begin{aligned} q_{k-1/2} = \frac{7}{12}\left(q_k + q_{k-1}\right) - \frac{1}{12}\left(q_{k+1} + q_{k-2}\right) + \\ \text{sign}\left(u\right)\frac{1}{12}\left[\left(q_{k+1} - q_{k-2}\right) - 3\left(q_k - q_{k-1}\right)\right]. \end{aligned} \tag{4.13}$$

The model uses a 3^{rd} order Runge-Kutta (RK3) time-integration for low-frequency modes. This applies 3 predictor-corrector steps to advance a prognostic variable from time t to time $t + \Delta t$. The sequence is illustrated here with the generic prognostic variable Ψ, where $\partial\Psi/\partial \mathrm{t} = R(\Psi)$, (*Skamarock et al.*, 2008)

$$\Psi^* = \Psi^t + \frac{\Delta t}{3} R(\Psi^t), \tag{4.14}$$

$$\Psi^{**} = \Psi^t + \frac{\Delta t}{2} R(\Psi^*), \tag{4.15}$$

$$\Psi^{t+\Delta t} = \Psi^t + \Delta t R(\Psi^{**}), \tag{4.16}$$

where the superscripts t, * , **, and $t+\Delta t$ indicate time levels. High-frequency modes, such as acoustic waves, are treated in a sub-time-step loop (at interval $\Delta\tau$) with an

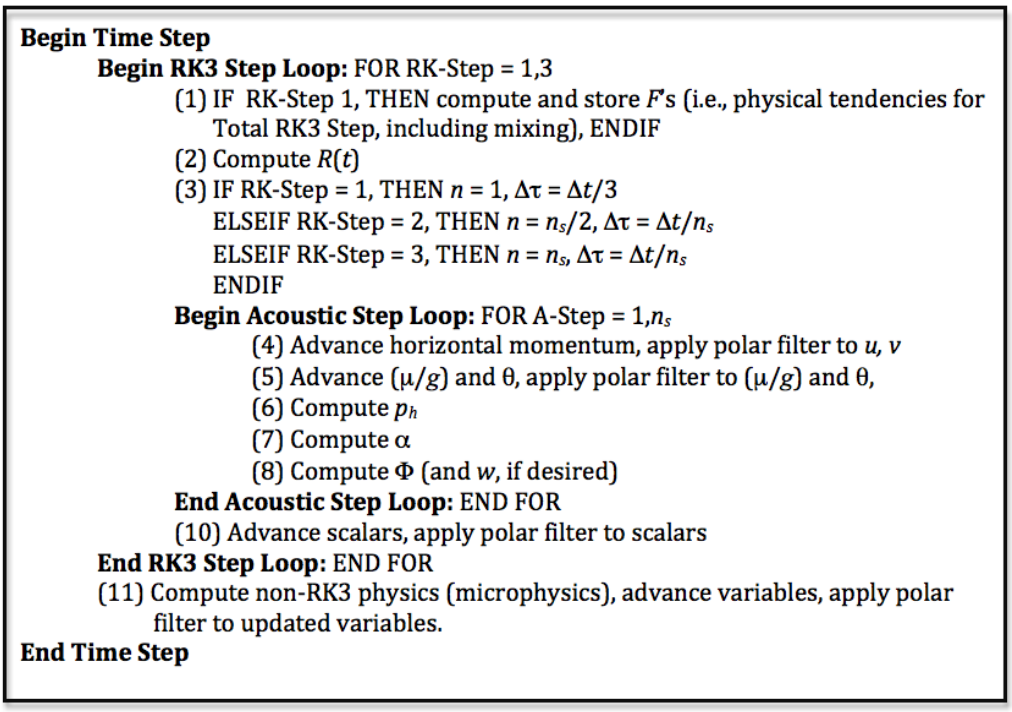

Figure 4.3: Time integration sequence used in MarsWRF. n is the number of acoustic timesteps for a substep of the RK3 integration, and n_s is the ratio of the RK3 time step to the acoustic timestep for the second and third RK3 substeps. Adapted from *Skamarock et al.* (2008).

explicit 2^{nd} order time-integration. The time integration sequence is illustrated in Figure 4.3.

4.2.2 Physics

Sub-grid scale physical processes are parameterized in the model. For Mars, these include radiative transfer through the dusty, CO_2 atmosphere and the seasonal CO_2 condensation to and sublimation from the polar caps. Sub-grid scale horizontal and vertical diffusion are also handled using parameterization schemes. In Section 4.3.2, we discuss the inclusion of wave drag.

Solar forcing in the model varies with space, local time, and season. The radiative transfer scheme accounts for the absorption of: near-IR solar radiation by CO_2, solar radiation by dust, and 15-μm thermal radiation by CO_2. It also accounts for scattering

by dust of solar radiation and thermal radiation outside the 15-μm band. Finally, it accounts for emission of 15-μm thermal radiation by CO_2 (*Richardson et al.*, 2007).

The wideband model previously used in MarsWRF was that used by the Oxford-LMD Mars GCM (*Forget et al.*, 1999), with the addition of nLTE treatment via tabulated cooling rates from *López-Valverde et al.* (1998) above $\sim$ 60 km. MarsWRF was recently improved to include the *k*-distribution method of radiative transfer developed for the Geophysical Fluid Dynamics Laboratory (GFDL) Mars GCM by *Mischna* (2004) (e.g., *Johnson et al.*, 2008), which accounts for vertical nonhomogeneities in the atmosphere and treats overlapping gas absorption features (*Liou*, 2002). This radiation code has been validated against other techniques of radiative transfer (Line-by-Line Radiative Transfer Model (LBLRTM) and Discrete-Ordinate Model of Radiative Transfer (DISORT)) as well as the radiative code employed in the Ames MGCM (M. Mischna, personal communication, April 4, 2012).

Dust opacity distributions in the model can be prescribed with a latitudinally and seasonally fixed τ (integrated dust opacity, see Section 2.4), or with a parameterization developed to match MGS-TES year 1 (see Figure 2.3) or Viking observations (corresponding to the time-varying spatial distribution of atmospheric dust based on the "MGS scenario" and "Viking scenario" developed for the Mars Climate Database (*Lewis et al.*, 1999)). Dust is distributed vertically in a Conrath profile using a latitudinally and seasonally fixed value of ν= 0.03 (Conrath parameter, see Equation 2.1). In the simulations performed for this study we use a variety of latitudinal dust distributions (see Table 4.1 and Section 4.3.1).

The condensation and sublimation of CO_2 is determined by calculating the surface heat balance at each time step (*Richardson et al.*, 2007). In the southernmost grid row, surface temperatures are set to the CO_2 frost point to represent the residual CO_2 frost cap observed over the south pole. When cooling below the condensation point is predicted, it is assumed to be due to CO_2 condensation. Likewise, when

Table 4.1: Inputs for simulations examined in this study.

Simulation	Latitudinal opacity	ν	GWMD (comment)
1	Fixed 0.1 ("clear")	3e-2	no
2	Fixed 0.5	3e-2	no
3	TES 1	3e-2	no
4	TES 1	3e-2	yes (VAR=(400 m)^2, $\kappa = 2.5\text{x}10^{-5}\text{m}^{-1}$)
5	TES 1	3e-2	yes (VAR=MOLA, $\kappa = 2.5\text{x}10^{-5}\text{m}^{-1}$)
6	TES 1	3e-2	yes (VAR=MOLA, $\kappa = 2.5\text{x}10^{-7}\text{m}^{-1}$)

heating above the condensation point is predicted in the presence of CO_2 ice on the surface, it is assumed to be due to CO_2 sublimation. In the atmosphere any cooling below the condensation point results in CO_2 precipitating onto the surface. When such changes to the atmospheric pressure occur, the surface pressure is updated and tracer mass mixing ratios are adjusted. Detailed CO_2 ice microphysics is not included in the model.

Sub-grid scale horizontal and vertical diffusion are handled using parameterization schemes developed for Earth with only the diffusivities changed. The deformation of the local wind field (i.e., the 2-D Smagorinsky approach (*Smagorinsky*, 1963)) is used to calculate the 2nd order horizontal diffusion tendencies on coordinate surfaces (*Richardson et al.*, 2007). Vertical diffusion can be treated with a specified (constant) vertical diffusion coefficient, or with a planetary boundary layer (PBL) scheme, which parameterizes heating- and mechanically induced turbulence (*Richardson et al.*, 2007). For the first two runs presented in this study (see Table 4.1) vertical diffusion is handled by the Medium Range Forecast model PBL (MRF-PBL) parameterization, which is a 2.5 order closure scheme (e.g., *Mellor and Yamada*, 1982; *Hong and Pan*, 1996).

Physical parameterizations are called from different locations within the time stepping (i.e., within the acoustic time stepping, RK3 time stepping, or at the end of the time loop) as required for stability and conservation (*Richardson et al.*, 2007).

4.2.3 Implementation

The model is run with 4 acoustic time steps per model time step. The physics routines are called every model time step.

The model is run on a supercomputer at the Jet Propulsion Laboratory, making use of 30 processors in distributed memory, parallel processing. The typical CPU duration for the 10°-L_s runs described later in this study is $\sim$ 3600 CPU hours, giving a wall clock duration of $\sim$ 120 hours.

A 10-sol "spin-up" period is used in every case to initialize the model and results are studied only after at least 10 sols into a simulation.

4.2.4 Testing and Advantages

MarsWRF is a competitive martian GCM. Its ability to reproduce the zonal mean temperature and zonal wind fields as well as the strength of the mean meridional overturning has been validated against previously published martian GCMs, such as the LMD Mars GCM and the GFDL Mars GCM (*Wilson et al.*, 2006; *Richardson et al.*, 2007; *Mischna and Wilson*, 2008). It has also demonstrated the ability to reproduce TES temperature observations (*Richardson et al.*, 2007).

MarsWRF's original (validated) vertical domain consisted of 40 vertical levels from the surface to $\sim$ 80 km altitude. Recently, the model top was lifted to $\sim$ 120 km altitude. To avoid losing vertical resolution, this required the addition of vertical levels (now 57). It also required the inclusion of nLTE 15μm cooling and nLTE near-IR heating rates in the radiative transfer routine. This work was performed by Dr. Steven Nelli (then at the University of Michigan) and Dr. Michael Mischna at the Jet Propulsion Laboratory. The results from MarsWRF up to p = 0.01 Pa (e.g., Figure 4.4) compare favorably with observations from SPICAM (see Section 2.2) and the MGCM-MTCM and the LMD GCM. Between p = 0.01 Pa and p = 3x10^{-4} Pa, MarsWRF over-predicts the SPICAM temperatures, similar to the tendency of other

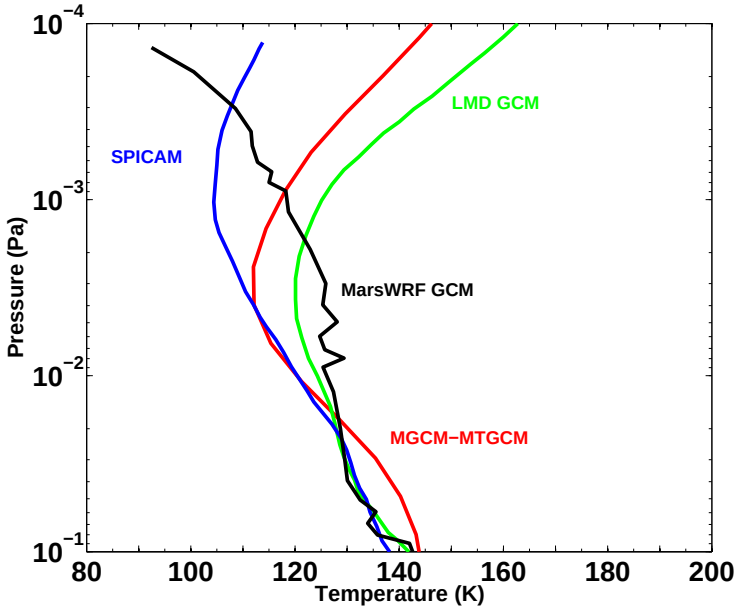

Figure 4.4: Figure 2.9 reproduced with the inclusion of the averaged simulated profile from MarsWRF using TES 1 dust opacities. These average temperature profiles are for the aphelion season at southern (winter) tropical latitudes on the nightside of the planet (L_s = 90-120°, LAT = 16°S-17°S, LT = 2.6-4.8).

GCMs, but it's vertical structure differs both from the SPICAM observations and from the predictions of other GCMs. At p <3x10^{-4} Pa, the model under-predicts the SPICAM temperatures. In fact, the model does not predict a clear mesopause in the simulated domain. However, below p = 5x10^{-3} Pa (i.e., where PW was observed by MCS, see Chapter 3) MarsWRF appears to perform in family with some of the most common GCMs employed for the middle atmosphere. This gives us confidence that MarsWRF can be used to explore the drivers of middle-atmosphere polar warming.

The advantages of MarsWRF over some other martian GCMs include that it is a seamless model from the surface to $\sim$ 120 km altitude. This allows the model to explore physical processes that originate in the lower atmosphere and impact the middle atmosphere, such as dust storms and upward propagating waves and tides. In addition it renders the model applicable to aerobraking predictions and subsequent analysis of the data obtained during aerobraking operations. It also means the model

is well suited to predicting EDL conditions for spacecraft that land on Mars. Another advantage of MarsWRF is that it makes use of a generalized map projection. This permits nested domains which allows for the examination of multi-scale processes and interactions, such as dust storms and gravity waves. It also allows for rotation of the numerical pole. Here we use the model without rotation of the numerical pole; however rotation may allow examination of geographical polar processes without the influence of polar filtering or polar boundary conditions. All of these features make this model well suited to studying the polar warming phenomenon at Mars.

4.3 Numerical Experiment Conditions

We perform six numerical experiments (see Table 4.1) to explore the relative importance of dust-heating and GWMD in reproducing the observed polar warming.

4.3.1 Dust Prescriptions

The experiments use three different prescriptions of horizontal dust opacity[1]: (1) latitudinally and seasonally fixed $\tau = 0.1$ (representing a "clear" background atmosphere), (2) latitudinally and seasonally fixed $\tau = 0.5$ (representing the global annual average dust opacity), and (3) latitudinally and seasonally varying TES year 1 opacities (see Figure 2.3). For every experiment we use Conrath $\nu = 0.03$, representing moderate dust mixing depths (see Figure 2.4 and Table 2.2).

4.3.2 Gravity Wave Momentum Deposition Parameterization

Gravity waves are launched by terrain irregularities (as well as convection, shear, and other mechanisms), including subgrid-scale orography. Such waves transport energy and mean-flow horizontal momentum vertically (*Nappo*, 2002) but are not re-

[1] A description of how dust is treated in numerical models and of the variables τ and ν is provided in Section 2.4.1.

solved in most GCMs, including MarsWRF. To account for the effects of gravity waves launched by subgrid-scale orography (i.e., stationary waves with phase speed, $c = 0$ m s^{-1}), we implement in the model a parameterization that reproduces the effects of GWMD. This parameterization is based upon the work of *Palmer et al.* (1986), using the gravity wave saturation theory of *Lindzen* (1981). This scheme was developed by Dr. Jim Murphy at New Mexico State University for use in the Ames MGCM and the Michigan Mars-Global Ionosphere Thermosphere Model (M-GITM) and has been implemented successfully in both models. For each grid cell, the parameterization calculates wave stress in the surface layer

$$\tau_s = \rho_0 \kappa N u_0 \mathrm{VAR}, \tag{4.17}$$

where ρ_0 is the density in the surface layer, κ is a tunable parameter that accounts for various wavenumbers, $N = (\mathrm{g}\partial \ln\theta/\partial \mathrm{z})^{1/2}$ is the Brunt-Väisälä frequency, u_0 is the zonal wind in the surface layer, and VAR is the variance of the subgrid-scale orography. Wave stress in each layer above the surface can be written

$$\tau(z) = \rho_0 \kappa N U_0 \delta h^2, \tag{4.18}$$

where U_0 is the component of the wind parallel to the surface wind, and δh is the amplitude of the vertical displacement of a material (i.e., isentropic) surface caused by the wave. Assuming $\tau = \tau_s$, Equation 4.18 is used to evaluate δh. The minimum Richardson number[2] that can be achieved under the action of gravity waves is calculated by

$$Ri_{min} = Ri \frac{1 - (N\delta h/U)}{\left[1 + Ri^{1/2}\,(N\delta h/U)\right]^2}, \tag{4.19}$$

[2]The Richardson number is a measure of the flow's stability with respect to small scale waves. When $Ri \gg 1$, the flow is buoyancy-driven. When $Ri \ll 1$, the flow is unstable with respect to shear instability (*Wallace and Hobbs*, 1977).

where $Ri = \mathrm{N}^2/(\mathrm{du/dz})^2$ is the background Richardson number. The saturation hypothesis says that if Ri_{min} <1/4, then the wave has reached saturation and breaking occurs (i.e., stress is deposited). *Palmer et al.* (1986) show that for a layer where breaking occurs, δh needs to be re-computed using $Ri_{min} = 1/4$ and evaluating equation 4.19. This simplifies to

$$\delta h_{sat} = \epsilon u/N, \tag{4.20}$$

where

$$\epsilon = Ri^{-1/2}\left(1 + 2Ri^{1/2}\right)\left[2Ri^{1/4}\left(1 + 2Ri^{1/2}\right)^{-1/2} - 1\right]. \tag{4.21}$$

The stress for a layer where saturation occurs can then be written

$$\tau_{sat} = \epsilon^2 \rho \kappa U^3/N. \tag{4.22}$$

This procedure gives a vertical profile of gravity-wave induced stress which is used to update the zonal velocity profile. This process parameterizes the flux deposition due to wave breaking only.

However, recent work by *Eckermann et al.* (2011) shows that IR-radiative damping of gravity waves increases with height in the middle atmosphere and is the dominant dissipation process for gravity waves with vertical wavelengths (λ_z) $\lesssim$ 10-15 km. This means that these gravity waves are dissipated by IR-damping rather than by breaking and therefore they do not deposit as much momentum flux at the high altitudes as previously predicted. The parameterization developed by Murphy applies the theory of *Eckermann et al.* (2011) to account for IR-radiative damping of small-scale gravity waves and avoid such over-prediction of momentum flux deposition.

Our experiments here are performed using the following values for the parameters in the GWMD routine: (1) VAR = $(400\ \mathrm{m})^2$ (corresponding to sinusoidal topography with horizontal wavelength = 250 km (*Palmer et al.*, 1986)) and $\kappa = 2.5\mathrm{x}10^{-5}\mathrm{m}^{-1}$ (in agreement with the value used for terrestrial studies), (2) VAR defined by the

standard deviation in topography as observed by MOLA and $\kappa = 2.5\text{x}10^{-5}\text{m}^{-1}$, and (3) VAR defined by the standard deviation in topography as observed by MOLA and $\kappa = 3.0\text{x}10^{-7}\text{m}^{-1}$ (best fit value found by *Collins et al.* (1997)). In all our experiments here, we use $\lambda_z = 7.5$ km. Future experiments will further explore the parameter space of κ and λ_z to find the set of values that provides the "best fit" for Mars based on the polar warming observed by MCS. Here we consider only a monochromatic wave. A full spectrum of gravity waves is likely important and will need to be addressed in the future. Parameterizations accounting for gravity waves having a variety of phase speeds have been developed by *Alexander and Dunkerton* (1999) for the Earth and by *Medvedev et al.* (2011a) for Mars. These may represent a method for improving upon the present study. The results we present here are initial results intended to demonstrate the new GWMD capability with MarsWRF. We have deliberately chosen this as a stopping point for this thesis work with the intention of fine-tuning this capability in the future to make it more physically realistic for the conditions at Mars (these may include, for example, using a variety of horizontal and vertical wavelengths, a spectrum of phase speeds, and incorporating temperature-dependency into the radiative-damping treatment).

4.4 Results

For each simulation we calculate the simulated PW using our technique from Chapter 3 (Equation 3.1). We focus our analysis of the simulation results on the cardinal seasons.

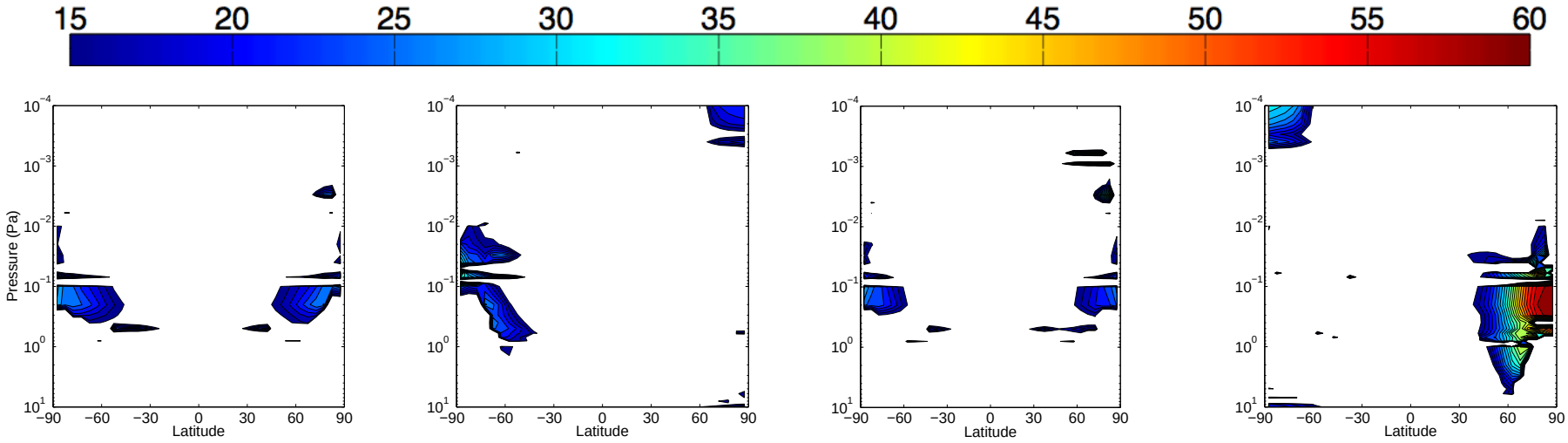

Figure 4.5: Pressure-latitude cross-sections of nightside PW ($\Delta_p T \geq 15$ K) from Simulation 1 (see Table 4.1). The colorbar is in K. Contours are drawn every 2 K, beginning at 15 K. From left to right: $L_s = 0°$, 90°, 180°, and 270°.

4.4.1 Simulation 1

4.4.1.1 Southern Hemisphere

The simulated PW in the southern hemisphere (Figure 4.5) does not extend as low in the atmosphere as the observed PW (see Figure 3.5). The latitudinal shape is consistent with observations, having the broadest latitudinal extent at high pressures and tapering toward the pole with decreasing pressure; however there are latitudinal and vertical gaps in PW in the simulation that are not present in the observations. The simulated PW magnitudes are smaller than observations during equinoxes, most significantly at $L_s = 180°$. Conversely, the simulated PW magnitudes are comparable to observations during local winter. This simulation locates the maximum dynamical warming slightly higher in the atmosphere than it is observed. It also fails to reproduce the observed seasonal pattern of southern hemisphere PW, namely an annual maximum[3] during the $L_s = 180°$ period, followed by $L_s = 0°$, and finally the annual minimum during the $L_s = 90°$ period. Instead it produces the annual maximum during $L_s = 90°$ and annual minima during the equinoxes.

4.4.1.2 Northern Hemisphere

The simulated PW in the northern hemisphere (see Figure 4.5) covers a vertical range similar to the observed PW during local winter (see Figure 3.5), but fails to extend as low in the atmosphere as the observed PW during equinoxes. As in the southern hemisphere, the latitudinal shape is consistent with observations during equinoxes, despite the gaps. During local winter, however, the shape is markedly different, displaying a shape most similar to that observed during MY 28, when the atmospheric dust opacity was much greater than $\tau = 0.1$. The simulated PW magnitudes are smaller than observations during equinoxes and larger than observations

[3]In these discussions we use the terms "annual maximum" and "annual minimum" to refer to the maximum and minimum of the four cardinal seasons. Intermittent seasons are not analyzed here.

during local winter (67 K vs. ∼40 K during MY 29 and MY 30 and 55 K during MY 28). This simulation fails to capture the observed seasonal pattern of northern hemisphere PW, namely annual maxima during $L_s = 180°$ and $L_s = 0°$ and an annual minimum during $L_s = 270°$, instead locating the annual maximum during $L_s = 270°$. The northern-hemisphere small-pressure PW produced by this simulation is consistently smaller than observed (see Tables C.6 and C.5).

4.4.1.3 Global

This simulation fails to capture the hemispheric asymmetry in PW magnitude (i.e., greater PW in the southern hemisphere than in the northern hemisphere) observed during most equinoxes (see Figure 3.5). In addition, it fails to reproduce the observed seasonal trend of comparable winter PW magnitudes at the two solstices (see Figure 3.5).

4.4.1.4 Discussion

Overall these results show that the "clear" atmosphere is capable of producing PW during $L_s = 270°$ that is of even greater magnitude that typically observed. It is also capable of producing weak PW during $L_s = 0°$, 90°, and 180° over latitudinal and vertical domains generally similar to where it is observed, but that the magnitude is far too small. In general, a "clear atmosphere" is insufficient for capturing the precise magnitude, vertical location, and seasonal variability of PW, in agreement with past studies that found the intensification and poleward expansion of the meridional circulation caused by dust heating was necessary for reproducing polar warming (e.g., *Wilson*, 1997; *Forget et al.*, 1999). This motivates our next numerical experiment forced with latitudinal dust opacities that are representative of the annual global average ($\tau = 0.5$).

4.4.2 Simulation 2

4.4.2.1 Southern Hemisphere

The simulated PW in the southern hemisphere (Figure 4.6) covers a broader vertical range than the PW observed (see Figure 3.5) or simulated with a "clear atmosphere" (see Figure 4.5), extending through the top of the modeled domain during equinoxes. The latitudinal shape is consistent with observations, having the broadest latitudinal extent at high pressures and tapering toward the pole with decreasing pressure. The gaps that were present in the "clear atmosphere" simulation have disappeared. The simulated PW magnitudes are smaller than observations during equinoxes, most significantly at $L_s = 180°$. Conversely, the simulated PW magnitudes are greater than observations during local winter. This simulation locates the maximum dynamical warming higher in the atmosphere than it is observed. It also fails to reproduce the observed seasonal pattern of southern hemisphere PW, namely an annual maximum during the $L_s = 180°$ period, followed by $L_s = 0°$, and finally the annual minimum during the $L_s = 90°$ period. Instead it produces the annual maximum during $L_s = 90°$ and annual minima during the equinoxes. The small-pressure (p <0.01 Pa) PW produced by this simulation is smaller than observed during local winter (see Tables C.3 and C.2)(observations are not available for comparison during equinoxes); however it is consistent with the seasonal pattern observed and at greater pressures (i.e., $L_s = 180°$, $L_s = 0°$, $L_s = 90°$).

4.4.2.2 Northern Hemisphere

The simulated PW in the northern hemisphere (see Figure 4.6) also covers a broader vertical range than the PW observed (see Figure 3.5) or simulated with a "clear atmosphere" (see Figure 4.5), and extends through the top of the model domain during equinoxes. As in the southern hemisphere, the latitudinal shape is

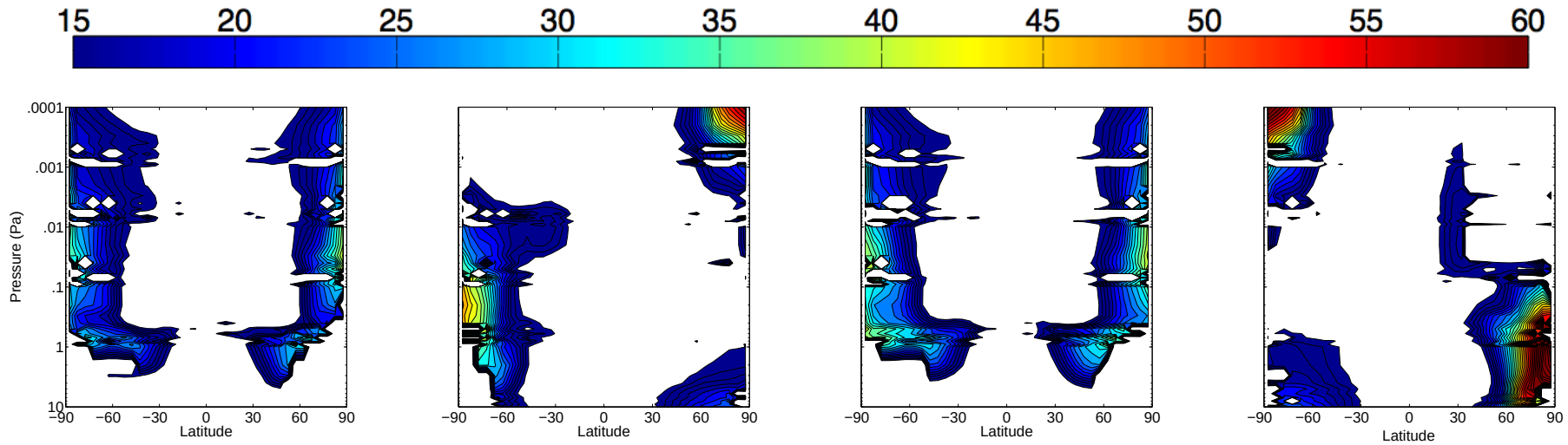

Figure 4.6: Same as Figure 4.5, except for Simulation 2 (see Table 4.1).

consistent with observations during equinoxes. During local winter, however, the shape is markedly different, displaying a broad latitudinal extent at large pressures and tapering equator-ward with decreasing pressure instead of poleward (as the observed PW does). The simulated PW magnitudes are comparable to observations during equinoxes and much larger than observations (102 K vs. ∼40 K) during local winter. In addition, this simulation locates the maximum dynamical warming much lower in the atmosphere that it is observed (∼40 km vs. ∼80 km). This simulation fails to capture the observed seasonal pattern of northern hemisphere PW, namely annual maxima during $L_s = 180°$ and $L_s = 0°$ and an annual minimum during $L_s = 270°$, instead locating the annual maximum during $L_s = 270°$.

4.4.2.3 Global

This simulation still fails to capture the hemispheric asymmetry in PW magnitude (i.e., greater PW in the southern hemisphere than in the northern hemisphere) observed during most equinoxes (see Figure 3.5). It also still fails to reproduce the observed seasonal trend of comparable winter PW magnitudes at the two solstices (see Figure 3.5).

4.4.2.4 Discussion

Overall these results show that a horizontally uniform and seasonally fixed dust opacity is sufficient for generating PW in the middle atmosphere and for reproducing its observed latitudinal shape. However, it is insufficient for capturing the precise magnitude, vertical location, and seasonal variability of PW. This suggests that seasonal and spatial variations in dust opacity may play an important role in controlling the finer details of the PW phenomenon, namely its magnitude, the vertical location of its maximum, and its seasonal cycle. This motivates our next numerical experiment forced with horizontal dust opacities that are more representative of the MCS

observing period. For this, we make use of MarsWRF's TES 1 dust option, as this functionality already exists in the model and the dust opacity magnitude and its evolution during TES 1 is fairly representative of the MY 29 and MY 30 dust conditions (see Figures 2.3 and 3.6).

4.4.3 Simulation 3

Since the dust conditions of TES 1 are most similar to MY 29 and MY 30, we compare these simulations with the bottom two rows of Figure 3.5.

The most striking feature of the PW simulated with TES 1 dust opacities (Figure 4.7) is how similar the shape and distribution of PW is to that simulated with a horizontally uniform and seasonally fixed $\tau = 0.5$ (see Figure 4.6). Rather than repeat the text from above, we focus here on the differences (improvements and worsenings of ability to reproduce the observed PW) compared to the simulations forced with $\tau = 0.5$.

4.4.3.1 Southern Hemisphere

The simulated PW in the southern hemisphere (Figure 4.7) covers a similarly broad vertical range to that simulated with uniform $\tau = 0.5$. The latitudinal shape produced in Simulation 3 more closely represents the observed PW than the Simulation-2 PW in that the latitudinal width at small pressures is narrower during equinoxes. During local winter however, the latitudinal shape produced by Simulation 3 is worse. The simulated PW magnitudes are smaller at all three cardinal seasons than those from Simulation 2, leaving the local winter magnitudes in better agreement with the observations and the equinox magnitudes under-estimated. The vertical location of the simulated maximum remains unimproved. The seasonal pattern of southern hemisphere PW is improved, now locating the annual maximum during the $L_s = 180^\circ$ period. However it still produces greater magnitude PW during local winter

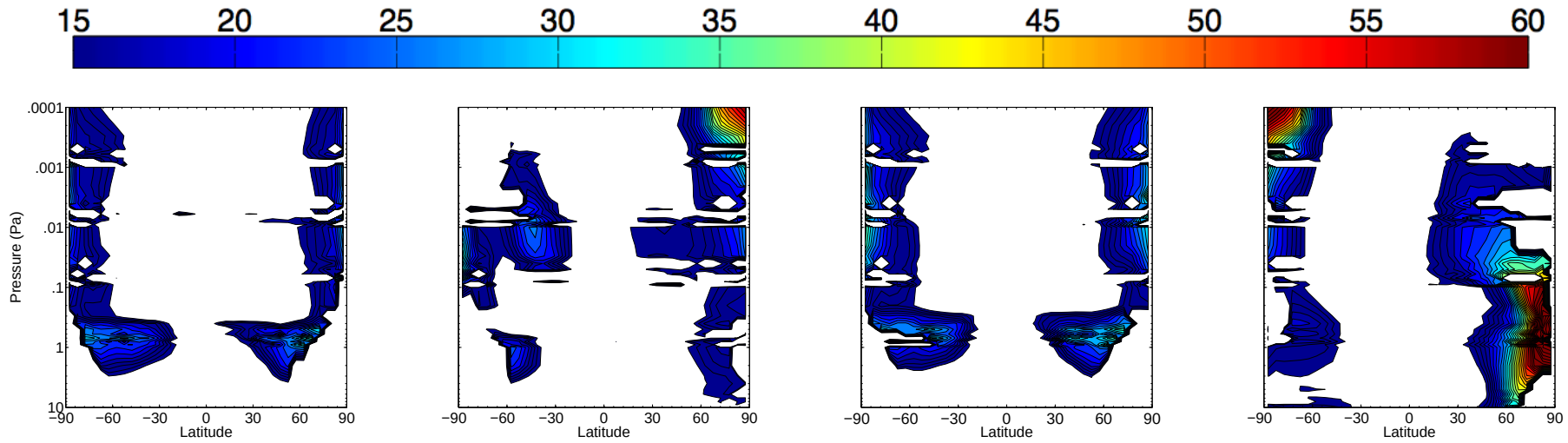

Figure 4.7: Same as Figure 4.5, except for Simulation 3 (see Table 4.1).

than during $L_s = 0°$, inconsistent with the observations. The magnitude of southern-hemisphere small-pressure (p <0.01 Pa) PW produced by this simulation remains unchanged (i.e., it continues to be smaller than the observations).

4.4.3.2 Northern Hemisphere

The simulated PW in the northern hemisphere (Figure 4.7) covers a similarly broad vertical range to that simulated with uniform $\tau = 0.5$. As in the southern hemisphere, during equinoxes the latitudinal shape of PW produced by Simulation 3 more closely represents the observed PW than that produced by Simulation 2. During local winter, the latitudinal shape also improves slightly, narrowing in latitude at large pressures and broadening poleward (compared to Simulation 2) at small pressures. The simulated PW magnitudes are smaller at all three cardinal seasons than those from Simulation 2, leaving the local winter magnitudes in better agreement with the observations, though still over-estimated (84 K vs. $\sim$ 40 K), and the equinox magnitudes slightly under-estimated. The vertical location of the northern hemisphere PW is improved slightly at all seasons, moving to greater pressures during equinoxes and smaller pressures during local winter. The seasonal pattern of northern hemisphere PW remains unimproved, still producing an annual maximum during local winter. The magnitude of the northern-hemisphere small-pressure PW produced in this simulation is unchanged from that produced in Simulation 2.

4.4.3.3 Global

This simulation still fails to capture the hemispheric asymmetry in PW magnitude (i.e., greater PW in the southern hemisphere than in the northern hemisphere) observed during most equinoxes. It also still fails to reproduce the observed seasonal trend of comparable winter PW magnitudes at the two solstices.

4.4.3.4 Discussion

Overall these results show that a latitudinal and seasonal distribution of dust opacity that is similar to, but not precisely representative of, the atmospheric conditions at the time of observations refines the latitudinal shape of PW in the direction of better agreement with observations, slightly refines the magnitude of PW in the direction of better agreement with observations, and slightly refines the vertical location of maximum PW in the direction of better agreement with observations. However, it remains insufficient for capturing the precise magnitude, vertical location, and seasonal variability of PW. This suggests that either: (1) fine detail in the seasonal and spatial variations of dust opacity (e.g., the differences between the opacity magnitude and evolution during MY 29/MY 30 and during MY 24) is important, (2) the latitudinal and seasonal details of the vertical distribution of dust aerosol (i.e., heating agent) are important, (3) another physical process, such as GWMD is important, or some combination of (1) - (3) is important for controlling the fine details of the PW phenomenon, namely its magnitude, the vertical location of its maximum, and its seasonal cycle. Suggestion 3 motivates our next numerical experiment, forced once again with the TES 1 dust option while including the GWMD parameterization described in Section 4.3.2. (1 and 2 are the subject of a proposed postdoctoral project.)

4.4.4 Simulation 4

As with the previous simulation, we focus our comparison here on the observed PW from MY 29 and MY 30.

4.4.4.1 Southern Hemisphere

The simulated PW in the southern hemisphere (Figure 4.8) covers a narrower vertical range than the PW simulated without GWMD (see Figure 4.7), with the topmost extent of PW occurring near 0.005 to 0.01 Pa. This is in better alignment with the

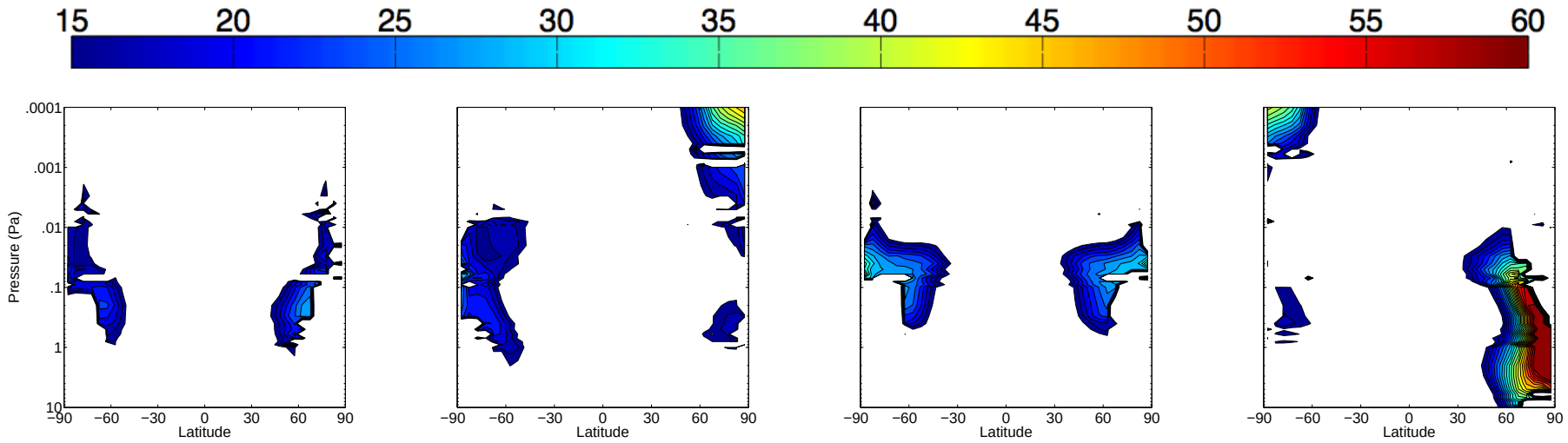

Figure 4.8: Same as Figure 4.5, except for Simulation 4 (see Table 4.1).

observations than Simulation 3 and indicates that the strongest wave breaking occurs above these pressures (above $\sim$ 85 km). With the inclusion of GWMD, the latitudinal shape of the simulated PW has changed. In particular it has become narrower at the greatest pressures of manifestation, losing its poleward extent. At equinoxes, the simulated PW magnitudes are slightly larger than those from Simulation 3, leaving them in better agreement with the observations, but still underestimated. During local winter, the simulated PW magnitude does not change significantly and remains underestimated. The vertical location of the simulated PW maximum has improved slightly from Simulation 3. The seasonal pattern of southern hemisphere PW produced by this simulation is consistent with the observed trend, locating the annual maximum during the $L_s = 180°$ period, followed by $L_s = 0°$, with local winter exhibiting the smallest magnitude.

4.4.4.2 Northern Hemisphere

As in the southern hemisphere, the simulated PW in the northern hemisphere (Figure 4.8) covers a narrower vertical range than the PW simulated without GWMD (see Figure 4.7). The topmost extent of PW occurs near 0.01 Pa, consistent with the observations. The inclusion of GWMD alters the latitudinal shape of the PW simulated at equinoxes. In particular it has become narrower at the greatest pressures of manifestation, losing its poleward extent. The GWMD treatment used here does not affect the latitudinal shape of the PW simulated at local winter. It does modify the magnitude of the simulated PW in the direction of better agreement with the observations. Specifically, at equinoxes, the magnitude increases slightly from Simulation 3. At local winter, the magnitude decreases slightly from that produced by Simulation 3. However, the equinox magnitudes are still slightly under-estimated and the local winter magnitudes are still significantly over-estimated (80 K vs. $\sim$ 40 K). The vertical location of the northern hemisphere PW at equinoxes improves slightly,

moving to greater pressures. It does not change significantly during local winter. The seasonal pattern of northern hemisphere PW remains unimproved, still producing an annual maximum during local winter.

4.4.4.3 Global

This simulation does generate a slight (3 K) asymmetry in PW magnitude (i.e., greater PW in the southern hemisphere than in the northern hemisphere) during the $L_s = 180°$ equinox. While this is not as strong as the asymmetry observed during most equinoxes, it is an improvement over Simulations 1-3. The opposite is true for the $L_s = 0°$ equinox. At this season this simulation generates greater PW in the northern hemisphere than in the southern hemisphere, opposite the trend seen in the observations. The inclusion of GWMD does not improve the simulation with regard to the observed seasonal trend of comparable winter PW magnitudes at the two solstices.

4.4.4.4 Discussion

Overall these results show that the inclusion of GWMD does improve the representation of PW in the middle atmosphere, particularly during the equinoxes and during southern winter. The improvements noted above indicate that the treatment of GWs used here produces GWMD in the right locations, but perhaps the magnitude is not sufficient. Tuning this routine to better reproduce the observations may help us understand which vertical and horizontal wavelengths have the strongest impact on the martian middle atmosphere during these seasons. That the treatment of GWs used here does not significantly improve the simulation of PW at northern winter may indicate one of several things: (1) this treatment is producing GWMD in the wrong (compared to the observed atmosphere) vertical location at this season, (2) this treatment is producing GWMD that is of insufficient magnitude at this season,

or (3) another process is affecting the PW magnitude and distribution during this season.

4.4.5 Simulation 5

4.4.5.1 Southern Hemisphere

The simulated PW in the southern hemisphere (Figure 4.9) covers a broader vertical range than the PW simulated with GWMD forced by uniform topography (see Figure 4.8), extending through the top of the model domain, but not extending as low in the atmosphere during equinoxes. This is a move away from the observed vertical range. During local winter, the vertical extent of PW simulated here is similar to that simulated with uniform topography and matches the observations fairly well. At equinoxes and at local winter, the simulated PW magnitudes are larger than those from Simulation 4, leaving them in better agreement with the observations. In fact, the local winter PW magnitude is now overestimated (56 K vs. the observed 40-45 K). The vertical location of the simulated PW maximum has remained unimproved from Simulation 4, with this simulation still placing the maximum PW too high in the atmosphere. The seasonal pattern of southern hemisphere PW produced by this simulation is now inconsistent with the observed trend, locating the annual maximum during the $L_s = 90°$ period, followed by $L_s = 180°$, with $L_s = 0°$exhibiting the smallest magnitude.

4.4.5.2 Northern Hemisphere

As in the southern hemisphere, the simulated PW in the northern hemisphere (Figure 4.9) covers a broader vertical range during equinoxes than the PW simulated with GWMD forced by uniform topography (see Figure 4.8), extending through the top of the model domain, but not extending as low in the atmosphere as it is observed. As in the southern hemisphere, this is a move away from the observed vertical range.

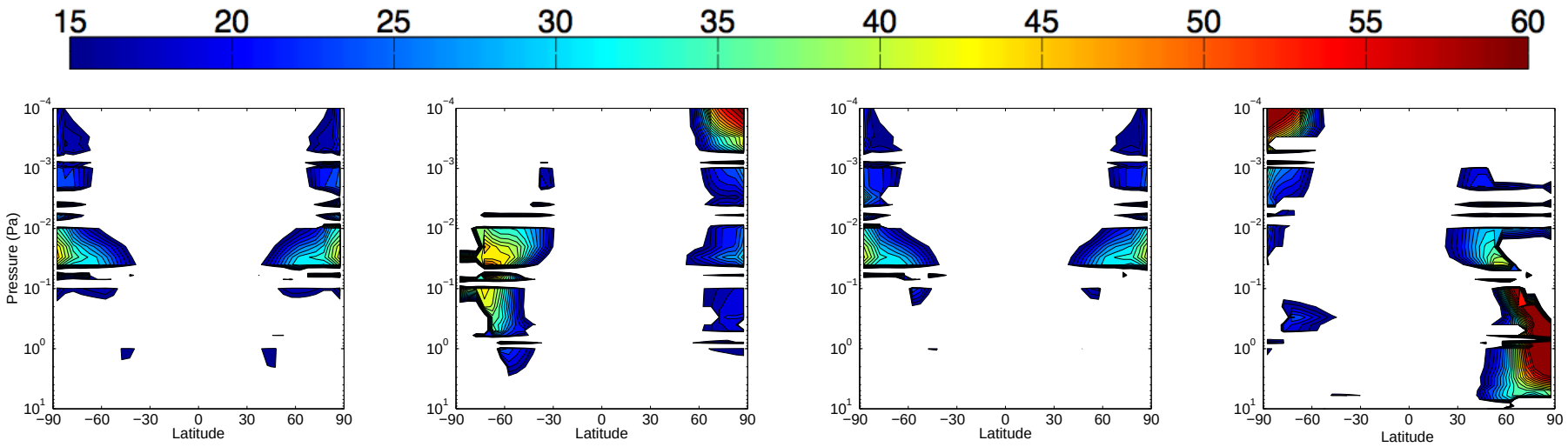

Figure 4.9: Same as Figure 4.5, except for Simulation 5 (see Table 4.1).

During local winter, the vertical extent of PW simulated here is broader than that simulated with uniform topography and extends higher into the atmosphere than the observations. This simulation results in an increase in the magnitude of the simulated PW during equinoxes compared to Simulation 4 (moving them in the direction of better agreement with the observations). At local winter, the PW magnitude remains unchanged from that produced by Simulation 4 (still overestimated). The vertical location of the northern hemisphere PW remains unimproved from Simulation 4 (too high during equinoxes and too low during local winter, compared to the observations). The seasonal pattern of northern hemisphere PW remains unimproved, still producing an annual maximum during local winter.

4.4.5.3 Global

This simulation does generate a slightly greater (6 K) asymmetry in PW magnitude (i.e., greater PW in the southern hemisphere than in the northern hemisphere) during the $L_s = 180^\circ$ equinox. Though this is not as strong as the asymmetry observed during most equinoxes, it is an improvement over Simulation 4. During the $L_s = 0^\circ$ equinox, this simulation generates PW of similar magnitude in both hemispheres. Forcing GWMD with observed topography improves the simulation with regard to the observed seasonal trend of comparable winter PW magnitudes at the two solstices; northern winter PW is still larger than souther winter PW, but the magnitudes are more similar than in Simulations 1-4.

4.4.5.4 Discussion

Overall these results show that forcing GWMD with observed topography rather than uniform topography does improve the magnitude of PW in the middle atmosphere. However, it worsens the representation of the vertical distribution of PW, particularly during the equinoxes and during northern winter. This indicates that

the GWMD is being applied too low in the atmosphere during equinoxes and too high in the atmosphere during northern winter. This motivates our final experiment in which we perform an initial sensitivity test as to the effect of a smaller κ value on the calculated PW. For this we use *Collins et al.* (1997)'s "best fit" value $\kappa = 3.0\text{x}10^{-7}$ m^{-1}.

4.4.6 Simulation 6

4.4.6.1 Southern Hemisphere

The simulated PW in the southern hemisphere (Figure 4.10) covers a narrower vertical range than the PW simulated with GWMD forced with the terrestrial best fit κ (see Figure 4.9), with only minimal PW at pressures less than 0.01 Pa. This is a move toward the observed vertical range. However, the simulated PW still fails to extend as low in the atmosphere as it is observed. The vertical extent of PW simulated here during local winter matches the observations reasonably well. At equinoxes and at local winter, the simulated PW magnitudes are smaller than those from Simulation 5 (by 3-8 K), leaving them in slightly worse agreement with the equinox observations and slightly better agreement with the local winter observations. The vertical location of the simulated PW maximum has remained unimproved from Simulation 5, with this simulation still placing the maximum PW too high in the atmosphere. The seasonal pattern of southern hemisphere PW produced by this simulation remains inconsistent with the observed trend, locating the annual maximum during the $L_s = 90°$ period, instead of during $L_s = 180°$.

4.4.6.2 Northern Hemisphere

As in the southern hemisphere, the simulated PW in the northern hemisphere (Figure 4.10) covers a broader vertical range than the PW simulated with GWMD forced with the terrestrial best fit κ (see Figure 4.9), with only minimal PW at pres-

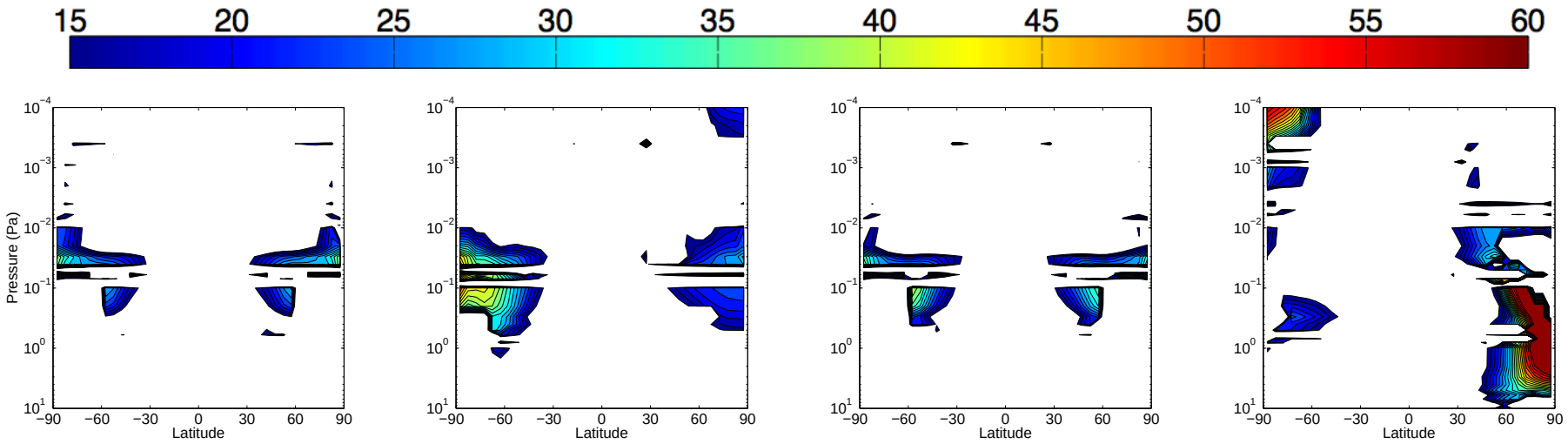

Figure 4.10: Same as Figure 4.5, except for Simulation 6 (see Table 4.1).

sures less than 0.01 Pa. Again, this is a move toward the observed vertical range. However, the simulated PW still fails to extend as low in the atmosphere as it is observed during equinoxes. As in the southern hemisphere, this simulation results in smaller magnitude PW at all seasons, which leaves the equinox PWs slightly underestimated and moves the local winter PW in the direction of better agreement with the observations (though still overestimated). The vertical location of the northern hemisphere PW remains unimproved from Simulation 5 (too high during equinoxes and too low during local winter, compared to the observations). The seasonal pattern of northern hemisphere PW remains unimproved, still producing an annual maximum during local winter.

4.4.6.3 Global

This simulation continues to generate a slight asymmetry in PW magnitude (i.e., greater PW in the southern hemisphere than in the northern hemisphere) during the $L_s = 180^\circ$ equinox (like the observations), and during the $L_s = 0^\circ$ equinox it continues to generate PW of similar magnitude in both hemispheres (unlike the observations). Forcing GWMD with the *Collins et al.* (1997) best fit κ improves the simulation with regard to the observed seasonal trend of comparable winter PW magnitudes at the two solstices; northern winter PW is still greater than souther winter PW, but the magnitudes are more similar than in Simulations 1-5.

4.4.6.4 Discussion

Overall these results show that forcing GWMD with the *Collins et al.* (1997) best fit κ for Mars rather the terrestrial best fit κ does improve the representation of the vertical distribution of PW as well as its magnitude and seasonal patterns. Though the magnitude of the simulated PW is improved, it remains significantly overestimated during northern winter. Additionally, the maximum PW is still too high in the

atmosphere during northern winter, compared to the observations. Moreover, the simulated PW still fails to extend as low in the atmosphere as it is observed during equinoxes. These findings indicate that GWMD is still being applied too low in the atmosphere during equinoxes and too high in the atmosphere during northern winter. This lays the foundation for future "tuning" of the GWMD routine implemented here, particularly exploring a wider range of κ values and exploring different λ_z values (which will affect the radiative damping of the gravity wave).

4.5 Discussion

The results from the first three experiments conducted in this investigation reveal that simulations forced with a "clear" atmosphere result in PW that is too weak during equinoxes and southern winter, and PW during northern winter that is similar to that observed during the GDS of MY 28. A simulation forced with globally uniform $\tau = 0.5$ at all seasons creates PW in the middle atmosphere that is similar to observations in terms of vertical and latitudinal range and shape. A simulation forced with dust opacities more representative of the latitudinal and seasonal variability of dust loading in the atmosphere at the time of the MCS observations slightly improves the shape as well as the magnitude of the simulated PW. However these results further reveal that a simulation forced only with dust opacities that are generally, but not precisely, representative of the MCS observation period (Simulation 3) is insufficient for producing the details of the PW phenomenon observed by MCS, specifically its magnitude, vertical distribution, and seasonal cycle.

The final three experiments conducted here reveal that GWMD is significant in generating the observed magnitude and distribution of PW during equinoxes and during southern winter. They also reveal that forcing gravity waves with the observed distribution of topography at Mars, rather than a uniform topography field, is necessary to capture the magnitude of PW observed during equinoxes and southern

winter. A sensitivity test using a smaller κ value shows that the "best fit" κ found by *Collins et al.* (1997) improves the vertical distribution of PW during equinoxes. Further tuning of the κ parameter is needed and will lead to insights into the wave characteristics that dominate at Mars during these seasons. Finally, the experiments conducted here reveal that GWMD, at least as treated here, does not significantly improve the northern winter PW simulations. This may indicate that a more rigorous "tuning" of this GWMD parameterization is needed, or that a more thorough treatment of GWs is needed for this season, or perhaps that another process contributes significantly to the PW structure observed during northern winter.

As indicated in the preceding paragraphs, there remain several outstanding questions in terms of the forcing behind the observed PW. We have itemized the outstanding parameter space to be explored in Table 4.2. In as far as the simulations presented here capture the observed trends, they shed some insight on these questions. For instance, what drives the magnitude of PW ($\Delta_p T$)? The large magnitude of PW generated during northern winter in Simulation 1 indicates that PW at this season is generated first and foremost by the thermally direct meridional circulation set up by the differential insolation at this season. That noteworthy PW is not generated at other seasons in this "clear" atmosphere simulation indicates that the thermally direct meridional circulation set up by differential insolation is not the primary driver of PW during these seasons. The large increase in PW magnitude during $L_s = 270°$ between Simulation 1 and Simulations 2 and 3 indicates that the seasonal variation in dust-heating and the resulting forcing on the mean meridional circulation does significantly impact the magnitude of the simulated PW. However, the fact that the very large magnitude PW produced during $L_s = 270°$ in the Simulation 2 is not replicated at the other seasons suggests that the enhanced circulation generated by a moderate column dust opacity itself is not enough to produce these large magnitudes of PW. A key ingredient for generating the forcing on the mean circulation that dust heating

may generate is the amount of incoming radiation available to be absorbed. The seasonal variation in solar forcing is the primary difference in forcing between the different seasons examined in Simulation 2. Judging by the difference in the magnitude of the PW simulated near perihelion and that simulated at the other seasons, this is a significant factor. That said, the magnitude of PW and its seasonal variability is not well-reproduced by these simulations, indicating that these considerations of dust heating's intensification and poleward expansion of the meridional circulation cannot explain the observed annual maximum PW at $L_s = 180°$ (instead of at $L_s = 270°$ as simulated). The comparison between the $L_s = 0°$-$180°$ PW produced by Simulations 2 and 3 indicate that, all else being equal (including solar forcing), larger column dust opacity (and greater latitudinal spread of dust) does lead to greater PW. Simulations 4-6 indicate that GWMD refines PW magnitude during equinoxes and southern winter, but does not significantly impact the PW magnitude during northern winter (at least as treated here).

What drives the hemispheric asymmetry in PW magnitude (larger in the southern hemisphere) observed during most equinoxes? Simulation 4 indicates that GWMD may partially explain the hemispheric asymmetry found in the observations and Simulations 5 and 6 reveal that gravity waves forced by the observed topography at Mars rather than a uniform topographic field may explain the asymmetry even better. It has been found that asymmetry in the solstitial (*Richardson and Wilson*, 2002) and equinox (*Tasahashi et al.*, 2003) circulations is sustained by the dichotomy in surface elevation (*Richardson and Wilson*, 2002). Perhaps this could further explain the asymmetric PW observed but not captured in the simulations. To test this, a simulation conducted with a the effects of topography removed should be performed (see Table 4.2). Another possibility is that sometimes vigorous dust lifting occurs near the south polar cap boundary during the $L_s = 180°$ equinox (see MY 26 in Figure 2.3). Dust-heating generated by such dust activity may intensify the circula-

Table 4.2: Parameter space yet to explore, in priority order.

Contemporaneous latitudinal distribution of dust opacity
Variety of dust mixing depths
Influences of the surface elevation dichotomy
κ (GWMD)
λ_z (IR damping of gravity waves)

tion in the southern hemisphere. Vigorous dust lifting near the south polar cap was not observed by THEMIS during MY 29 and MY 30, but this may be the result of poor sampling (caused by retrieval requirements) over the southern hemisphere during these seasons. If there was indeed vigorous dust lifting near the south polar cap during these equinoxes, this may not have been fully represented by the TES 1 opacity maps (see MY 24 in Figure 2.3). A final consideration is that the vertical distribution of dust aerosol (heating agent) varies with latitude and is not well-represented by a globally uniform ν, or perhaps is not even well represented by a Conrath profile (*Heavens et al.*, 2011b). As discussed by *Schneider* (1983), the vertical distribution of diabatic heating strongly influences the mean meridional circulation. Therefore an improved empirical prescription of the vertical distribution of dust at various latitudes and seasons may be needed to capture the latitudinal and seasonal variation of PW observed by MCS. This hypothesis can be tested in the near future by conducting simulations with a variety of dust mixing depths (see Table 4.2). This will give an indication as to whether or not the vertical distribution of aerosol does indeed have a strong influence on the simulated PW.

What drives the vertical distribution of PW, specifically the pressure at which it maximizes? In general, the circulation forcings examined here are incapable of capturing the precise vertical location where PW maximizes and how this location varies with season. The pressure where the simulated PW maximizes does not change significantly between Simulations 1, 2 and 3 and therefore does not seem to be tied to dust heating enhancement of the circulation (when the dust mixing depth is held

constant at $\nu = 0.03$). It also does not change significantly between Simulations 3 and 4-6 and therefore does not seem to be tied to the effects of GWMD on the circulation.

The discrepancies between the simulations and the observations provide insight into the magnitude of gravity wave drag needed to reproduce the observed thermal structure. The greater discrepancies at northern winter than at other seasons imply that gravity wave activity may be greater at northern winter than at other seasons. These simulations suggest the strongest wave drag may be needed during northern winter at pressures of 10 to 0.01 Pa to reduce the magnitude of the simulated PW. This will inform our choices as we tune the GWMD parameterization.

Tuning the GWMD treatment applied here (see Table 4.2) may lead to resolution to some of these outstanding questions. Furthermore, the GWMD parameterization used here accounts for wave drag affecting only the u component of the wind, not the full 3-component wind vector. Adjusting the parameterization to apply wave drag to the full wind vector will make the parameterization more realistic, and may improve simulations of PW. Furthermore, the GWMD parameterization used here uses one gravity wave. However, gravity waves are ubiquitous in the atmosphere and accounting for multiple waves at a variety of horizontal and vertical wavelengths as well as a variety of phase speeds is likely important (e.g., *Medvedev et al.*, 2011a). In such a case, wave interactions may also be incorporated and would make the parameterization more realistic still.

When a simulation that reproduces the observed distribution, magnitude and seasonality of PW has been achieved (i.e., when a "best fit" set of values for the κ and λ_z parameters has been found), we expect a decomposition of the simulated global winds will provide further insight into the relative role, during non-GDS conditions, of the different resolved eddy forcings (i.e., thermal tides and planetary waves) compared with the parameterized sub-grid scale gravity wave forcing, similar to the analysis performed for GDS conditions by *Kuroda et al.* (2009). Finally, based on their inter-

pretation of the MCS temperature and aerosol distributions, *Heavens et al.* (2011a) suggest that the middle and lower atmosphere circulations are partially kinematically coupled, sharing ascending branches and having separate (de-coupled) descending branches. Further modeling efforts aimed at reproducing the observed PW and diagnosing the physical mechanisms driving it may provide further insight into the degree of coupling between these circulations.

CHAPTER V

Conclusions

5.1 Summary of Findings and Contributions

While numerous advancements have been made in the level of scientific understanding of Mars's upper and lower atmospheres over the past several decades, insight into the mechanisms of the middle atmosphere has come at a slower pace due to the small number of datasets available for this region. Over the past 15 years this has begun to change, with renewed interest by NASA and European Space Agency (ESA) to send spacecraft to Mars. The result of these recent efforts is a growing database for Mars's middle atmosphere, enabling long-awaited and necessary studies characterizing the middle-altitude region, such as those presented in this thesis.

In Chapter 2, we characterized the middle atmosphere using the SPICAM temperature and density datasets. We learned that the nightside middle atmosphere is colder than found by previous EDL profiles. We found that the nightside mesopause is colder (105 K) and lower in the atmosphere (103 km) during southern winter at southern mid-latitudes, and warmer (115 K) and higher in the atmosphere (118 km) during southern summer at southern tropical latitudes. While the 80-km temperature is warmer (by 20 K) at southern summer tropical latitudes than that at southern winter mid-latitudes, the reverse is true at 130-km, where the southern summer tropical latitudes are 36 K colder than the southern winter mid-latitude temperatures. This

indicates differences in the heat balances between these seasons and locations at these altitudes.

Average SPICAM 80- to 100-km temperatures in the equatorial band (45°S - 45°N) exhibited an annual minimum during mid-to-late southern winter, and an annual maximum across the perihelion season, showing that temperatures at these altitudes are strongly influenced by lower atmosphere dust loading and seasonal solar heating variations.

Densities at all altitudes between 80 and 130 km responded immediately and strongly to the anomalous dust event that occurred around L_s = 140 ° of MY 27 and did not relax to their background state before the high-dust season began (around L_s = 250°). Density variance increased with altitude at nearly all seasons.

In the Chapter-2 study we also tested and constrained the coupled multi-dimensional MGCM-MTGCM code at middle altitudes and used the model to explore the importance of lower atmosphere dust heating for the structure at 80 to 130 km. The modeling results highlighted the the sensitivity of the middle-atmosphere density and thermal structure to variations in lower atmosphere dust loading and indicated that contemporaneous dust prescription within GCMs provide the greatest likelihood of accurately reproducing the density and thermal structure of the middle atmosphere on Mars. This was underscored by the difficulty displayed by the MGCM-MTGCM to reproduce the observed densities during the anomalous dust ramp-up period of MY 27 (L_s = 120°-200°) that was not detected by the contemporaneous THEMIS dust observations used to force the model but was detected in independent measurements by rovers on the surface.

In addition, we found that the MGCM-MTGCM accurately reproduced the observed temperature profiles below the mesopause, but that the modeled mesopause altitude was too low and its temperature too warm (by 5-10 K) compared to observations, similar to the behavior displayed by the LMD GCM (*Forget et al.*, 2009).

This may be related to nightside dynamical heating processes that require further refinement. In addition, CO_2 15-μm cooling rates may be too small, which would be consistent with underestimated atomic O abundances.

In Chapter 3, we used a quantitative metric to characterize middle-atmosphere PW in the available spacecraft datasets (primarily MCS). Over the three martian years of MCS data analyzed, PW manifested between p = 3 - 7 Pa and p = 6x10^{-2} to 5x10^{-3} Pa. It manifested slightly lower in the atmosphere (greater pressures) in the southern hemisphere and slightly higher in the atmosphere (smaller pressures) in the northern hemisphere.

PW manifested between $\sim$ 30° and 80°-85° latitude. In general, it expanded in both the poleward and equatorward directions with height until reaching its broadest latitudinal extent (typically at a pressure between p = 0.3 and 4 Pa). During northern winter the latitudinal range of PW tended to remain very narrow (10-20° in width) and moved poleward with height.

Maximum PW magnitudes ranged from 32 to 56 K. They tended to be larger on the nightside than on the dayside (by up to 23 K), indicating stronger subsidence on the nightside. During non-GDS years, maximum PW for each hemisphere tended to be greatest during L_s = 180°, suggesting the circulation was strongest during this season. Furthermore, in more than half of the equinoxes observed, southern maximum PW was larger than northern maximum PW, perhaps indicating asymmetry in the strength of the circulation during these equinoxes. As expected from previous studies, during a year that experienced a global dust storm (GDS), the magnitude of maximum PW was larger during northern winter solstice than southern winter solstice. Unexpectedly, during a non-GDS year, the magnitude of maximum PW during the two solstices was similar, suggesting that forcings other than the dust-heating enhancement of the mean meridional circulation may contribute to PW magnitudes.

The pressure at which PW maximized varied widely from p = 1.9 to 5.5 x 10^{-3}

Pa. Generally, the maximum PW occurred lower in the atmosphere (i.e., at larger pressure) during southern local winter than during northern local winter.

The work presented in Chapter 3 also resulted in tables of longitudinally averaged MCS temperatures and PW calculations (presented in the Appendices) that can be used to test GCM calculations of middle-atmosphere temperatures and constrain calculations of winds and the global circulation.

In Chapter 4, we attempted to reproduce the observed middle-atmosphere polar warming with limited success. Using MarsWRF we performed an initial investigation of the importance of the forcings generated by lower atmosphere dust heating and by an orographic gravity wave in producing the middle-atmosphere PW characterized in Chapter 3. For this we used MarsWRF with it's recently extended vertical domain (0-120 km).

The results of this investigation revealed that a "clear" atmosphere does not produce significant PW during equinoxes or during southern winter; however it does generate significant PW during northern winter. An atmosphere with a globally uniform $\tau = 0.5$ at all seasons (a forcing commonly used in GCMs to represent an annual global average level of "dustiness") produces PW in the middle atmosphere that is similar to observations in terms of vertical and latitudinal range and shape. Dust opacities more representative of the latitudinal and seasonal variability of dust loading in the atmosphere at the time of the MCS observations slightly improved the shape as well as the magnitude of the simulated PW. However, a simulation forced only with dust opacities that are generally, but not precisely, representative of the MCS observation period was found to be insufficient for producing the details of the PW phenomenon observed by MCS, specifically it's magnitude, vertical distribution, and seasonal cycle.

The results suggest that the seasonal variation in dust-heating and the resulting forcing on the mean meridional circulation significantly impacts the magnitude of

the simulated PW. All else being equal (particularly solar forcing), larger column dust opacity (and greater latitudinal distribution of dust) leads to larger PW magnitudes. However, a moderate column dust opacity itself is not enough to produce large magnitudes of PW during the aphelion season when the incident radiation is small.

The magnitude of PW and its seasonal variability is not well-reproduced by the simulations conducted in Chapter 4. They cannot explain the observed annual maximum PW magnitude at $L_s = 180°$ (instead of at $L_s = 270°$ as simulated). Nor can they completely explain the hemispheric asymmetry found in the observations during most equinoxes. Though the circulation forcings examined in Chapter 4 are incapable of reproducing the precise vertical location where PW maximizes and how this location varies with season, the results suggest that the vertical distribution of PW in the northern (but not the southern) hemisphere may be influenced by dust heating's effects on the circulation.

Lastly, the simulations in Chapter 4 demonstrate that gravity wave momentum deposition does strongly impact the thermal structure of the middle atmosphere. However, the precise characteristics of the waves responsible for refining the distribution and magnitude of polar warming produced by a dusty and gravity-wave free atmosphere toward the distribution and magnitude observed by MCS are inconclusive thus far. Fine tuning of the gravity wave parameterization is needed yet. The simulations in Chapter 4 suggest strong gravity wave drag is needed during northern winter at pressures of 10 to 0.01 Pa in order to bring the simulations into agreement with the observed PW magnitudes.

5.2 Future Work

The SPICAM instrument continues to be in operation and 2-3 additional MYs of SPICAM data is expected to be available for analysis in the near future. A follow-

up study to that presented in Chapter 2, using these additional MYs of SPICAM temperature and density observations will be valuable to evaluate the robustness of the work laid out in Chapter 2 and address interannual variations of the mesopause height and temperatures. Additionally, we are hopeful that this additional data from SPICAM will provide more high-latitude coverage with which to diagnose polar warming in the region above the MCS domain. Finally, these observations will serve as strong constraints for the energetics and dynamics of 3-D GCMs, including the MGCM-MTGCM, MarsWRF, and M-GITM.

It should also be noted that the effects of longitudinal variations of dust opacity upon the thermal structure of the middle atmosphere are virtually unexplored. Modeling studies examining the influence of longitudinally varying dust opacity upon the temperature and altitude of the mesopause are needed.

The observational characterization of PW presented in Chapter 3 and the initial modeling work presented in Chapter 4 motivates further investigation into the PW phenomenon and the driving forces behind the observed hemispheric, diurnal, seasonal, and interannual variations in PW. Such future work can take two paths: extending the observational analysis, and conducting further modeling experiments.

The work in Chapter 3 focused on describing PW at cardinal seasons. A full year analysis would permit investigation of the possibility that PW may lag the solar forcing. This work has been started for MY 28 (see Figures 5.1 and 5.2) and can be extended to MY 29 and MY 30. Additionally, MCS is still operational and as additional seasons of data are retrieved this study can be extended to further MYs. Such an extension may add robustness to the climatology presented in Chapter 3.

Further modeling experiments (summarized in Table 5.1) that would improve the dust treatment in the model include: (a) forcing the model with latitudinal dust opacities representative of the MCS observing period (from THEMIS or MCS), (b) exploring the influence of variations in dust mixing depth, and (c) addressing varia-

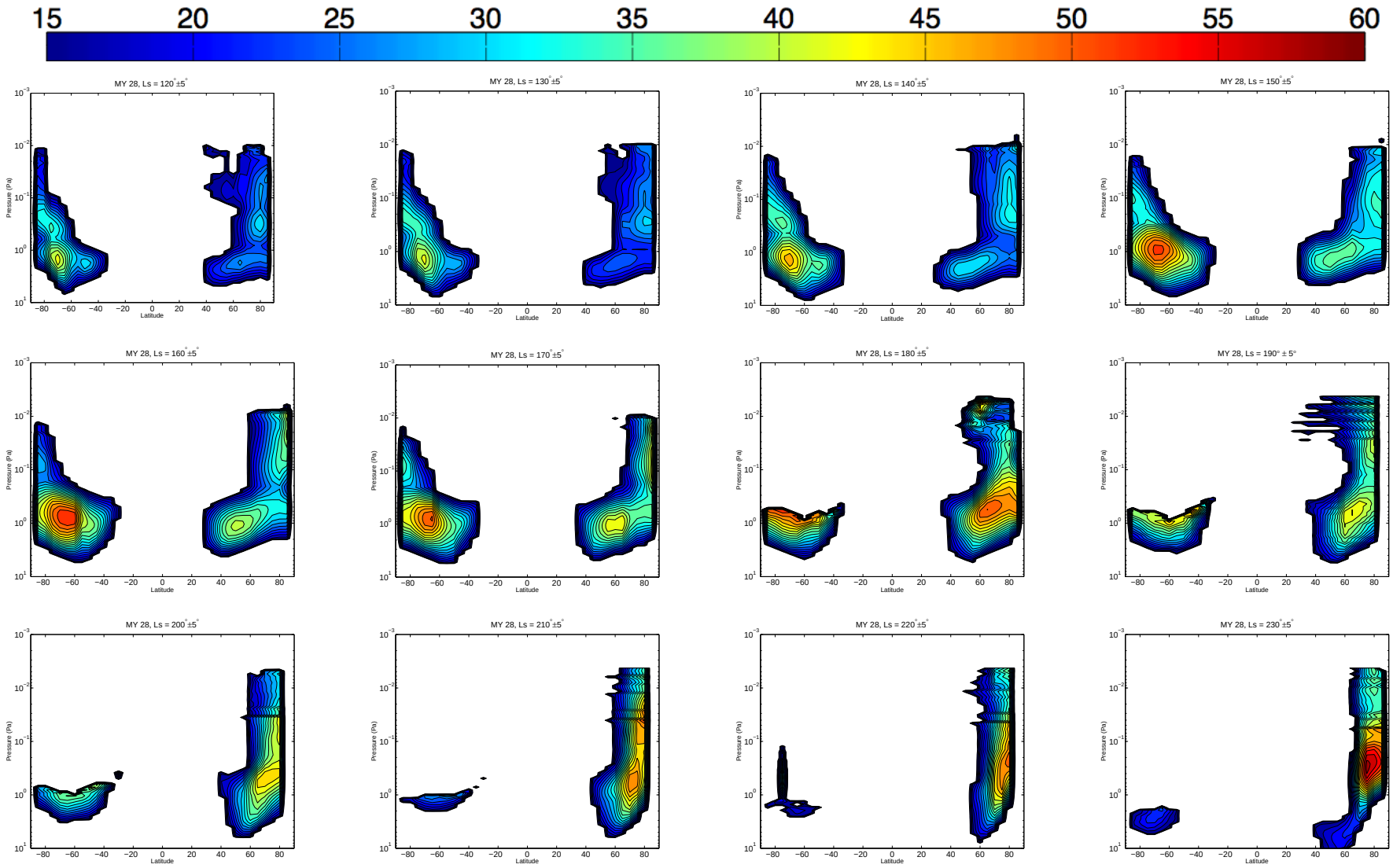

Figure 5.1: Same as Figure 3.5, except extended for a full seasonal analysis (every 10°-L_s interval) for MY 28. The colorbar is in K. Contours are drawn every 2 K, beginning at 15 K.

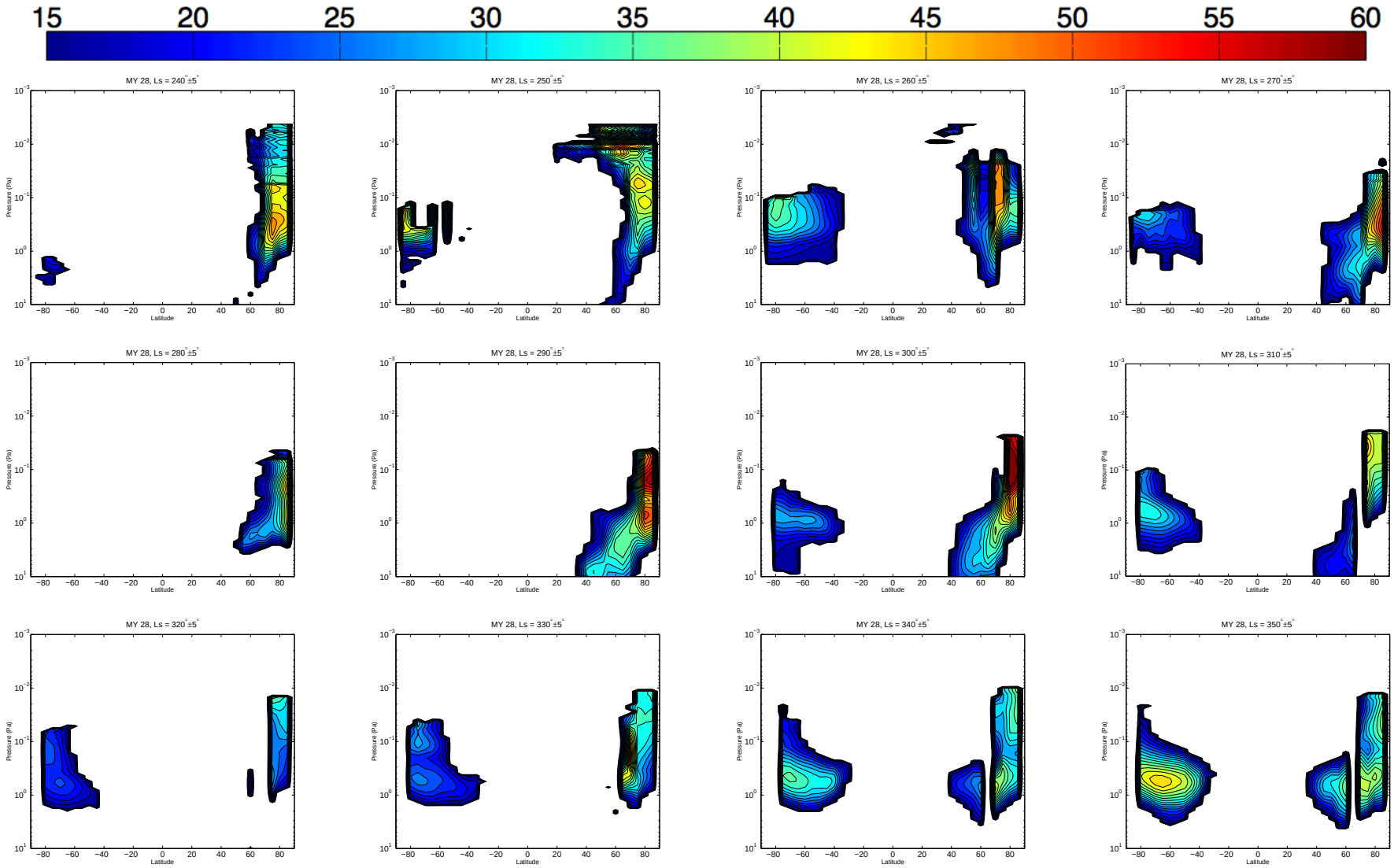

Figure 5.2: Continuation of Figure 5.1.

Table 5.1: Model inputs for further investigation of PW forcings.

Simulation	Latitudinal opacity	Vertical dust distribution	GWMD	κ (m^{-1})	λ_z (km)	Motivating Idea or Question
1	MY 28-MY 30	ν = 3e-2	yes	2.5 E-5	7.5	Contemporaneous latitudinal dust
2	MY 28-MY 30	ν = 3e-3 to 3e-4	yes	2.5 E-5	7.5	Influence of dust mixing depth
3	MY 28-MY 30	Empirical, based on *Heavens* (2010)	yes	2.5 E-5	7.5	Non-Conrath vertical distribution of aerosol important for PW?
4	MY 28-MY 30	same as Sim. 3	yes	variety	7.5	Which κ gives best fit?
5	MY 28-MY 30	same as Sim. 3	yes	based on Sim. 4	1.0-10.0	Which λ_z gives best fit?
6	MY 28-MY 30	same as Sim. 3	yes	based on Sim. 4	based on Sim. 5	Full-year analysis

tions in the vertical distribution of dust (described below). Other modeling experiments aimed at improving the treatment of GWMD involve fine-tuning the GWMD tunable parameters (κ and λ_z) to determine the values that give the best fit to the observations. Once a reasonable fit has been achieved the numerical investigation of PW forcings can be extended to a full year.

Heavens (2010) examines the vertical distribution of dust observed by MCS during the clear season and discovers that commonly over the tropics and occasionally over the poles there exists a vertical maximum in density scaled dust opacity high above the surface. They show that such observations are inconsistent with the vertical distribution of dust assumed by a Conrath profile (maximum optical depth occuring at or near the surface) (Figure 5.3). Upon finding that the vertical distribution of density scaled opacity is inadequately represented by a Conrath distribution (e.g., ν) during the aphelion season, *Heavens* (2010) developed the theory that the vertical distribution can be suitably described by a set of 6 parameters: the low level background dust, the dustiness of the dust "pulse" (i.e., the vertical maximum of density scaled opacity and that portion of the dust profile not accurately represented by a Conrath profile), the height of the pulse, the cutoff height of the pulse (i.e., the altitude at which the density scaled opacity goes to ~ 0), the vertical thickness of the pulse, and the cutoff length (i.e., the vertical distance required for the density scaled opacity to fall to ~ 0). Applying this technique to the dusty season will facilitate development of an improved representation of the vertical distribution of dust at all seasons for use in GCMs. Because the mean meridional circulation is significantly

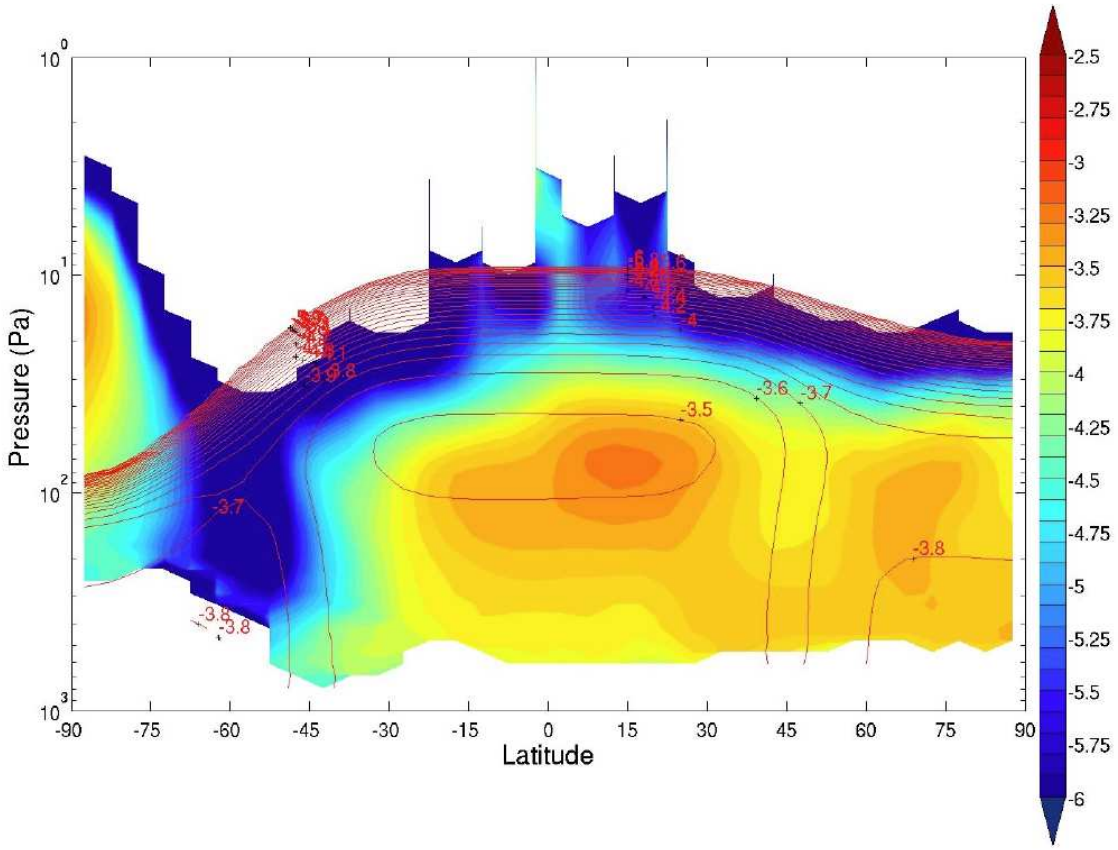

Figure 5.3: Nightside zonally averaged dust density-scaled opacity from the MY 28 clear season. MCS retrievals of dust density-scaled opacity are shown by the color contours ($\log_{10}$ scale). Mars Climate Database values based on the LMD GCM's modified Conrath scheme are shown by the red contours (again, $\log_{10}$ scale). From *Heavens* (2010).

affected by the vertical distribution of heating agent (dust), such work is expected to improve simulations of PW, particularly during the dusty season, which as we've shown in this thesis is the most challenging season to simulate observed PW trends.

Overall, the work presented in this thesis has provided a more comprehensive picture of the middle atmosphere. It has shown that the middle atmosphere is a coupling region between the lower atmosphere and the upper atmosphere and as such it influences the upper atmosphere that is available for atmospheric escape. This work has improved the understanding of the density and temperature in the 50-130 km region and how they vary with space and time, which is critical for the safety of landing spacecraft as well as aerobraking orbiters and as such protects the investment made on these expensive craft. Finally, this work has shown that a process that affects the middle atmosphere of Earth is also important for the middle atmosphere temperature structure at Mars, strengthening the notion that a comparative approach planetary atmospheric science is fruitful.

Finally, this thesis is but a beginning and underscores the need for continued monitoring of the temperature and dust opacity of the lower and middle atmosphere (0-90 km) in order to build a multi-annual climatology of the Martian atmosphere. For this, it is crucial that the EMCS instrument be flown on a future orbiter. The work in this thesis also highlights the need for continued monitoring of the density and temperature of the 70-130 km region in order to build a multi-annual climatology of the mesopause region. For this, continued stellar occultation observations are needed, such as those that will be performed by the Imaging Ultra Violet Spectrometer that will be carried on the MAVEN orbiter (to be launched in 2013).

APPENDICES

APPENDIX A

Figures of Raw and Averaged MCS Temperatures on Select Pressure Surfaces

The figures in this appendix show the raw MCS temperatures and their longitudinal averages for decade intervals of log pressure.

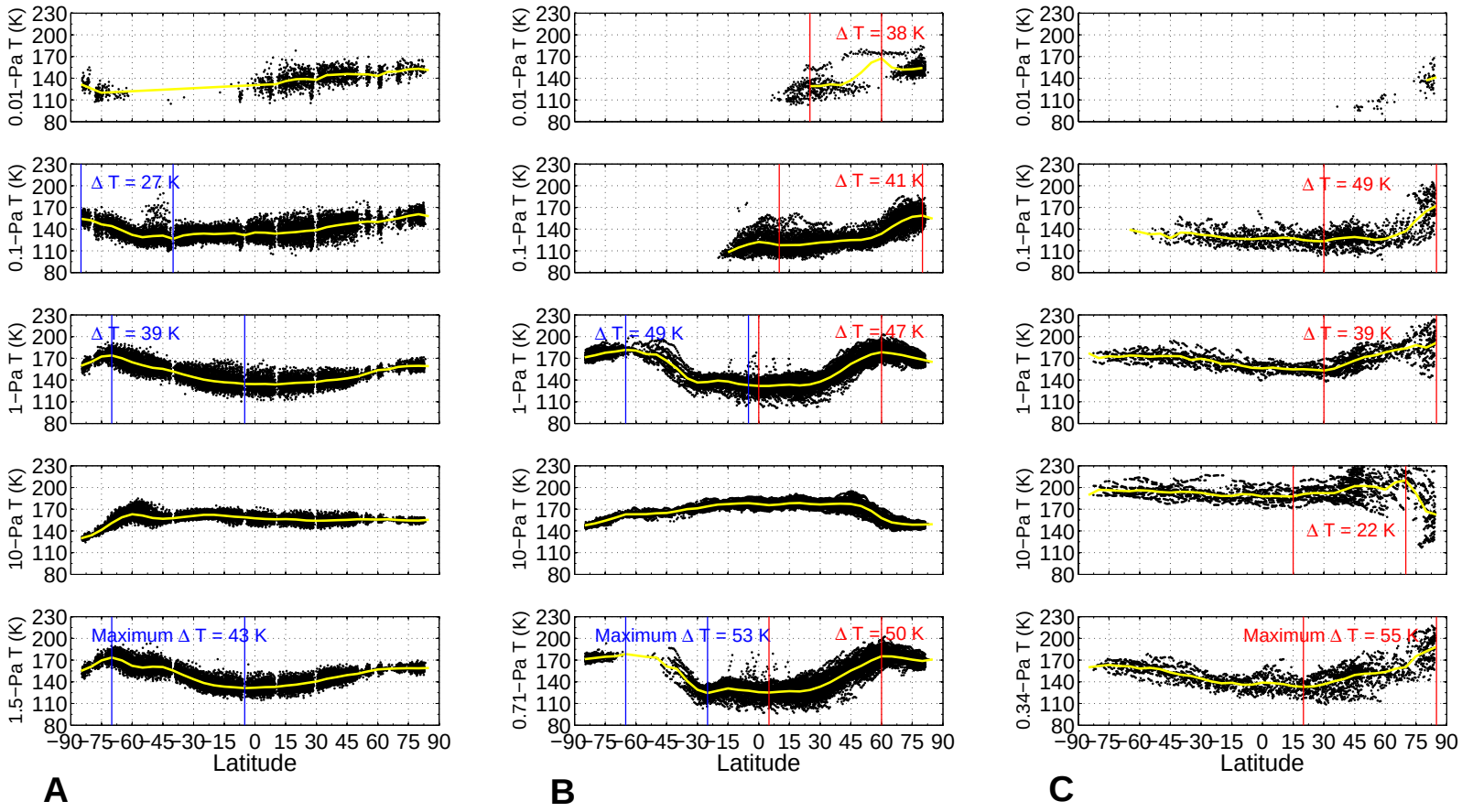

Figure A.1: Nightside MCS temperatures versus latitude on select pressure surfaces for MY 28: (a) near southern winter (L_s = 115°), (b) L_s = 180° equinox , and (c) northern winter (L_s = 270°). Black points depict temperatures from MCS. The yellow curve is the longitudinally averaged temperatures (in 5-degree latitude bins). The latitudes of T_{max} and T_{min} are traced by solid blue lines in the southern hemisphere and solid red lines in the northern hemisphere. Notable PW features ($\Delta_p T$ >15 K) are printed. The pressure surfaces displayed in the top 4 subpanels are consistent across all seasons (p = 10, 1, 0.1, and 0.01 Pa), while that displayed in the bottom subpanel varies with season to depict the pressure surface on which PW ($\Delta_p T$) maximizes vertically. During equinox, the pressure surface shown in the bottom subpanel is chosen based on the hemisphere that has the greater maximum $\Delta_p T$ during that season.

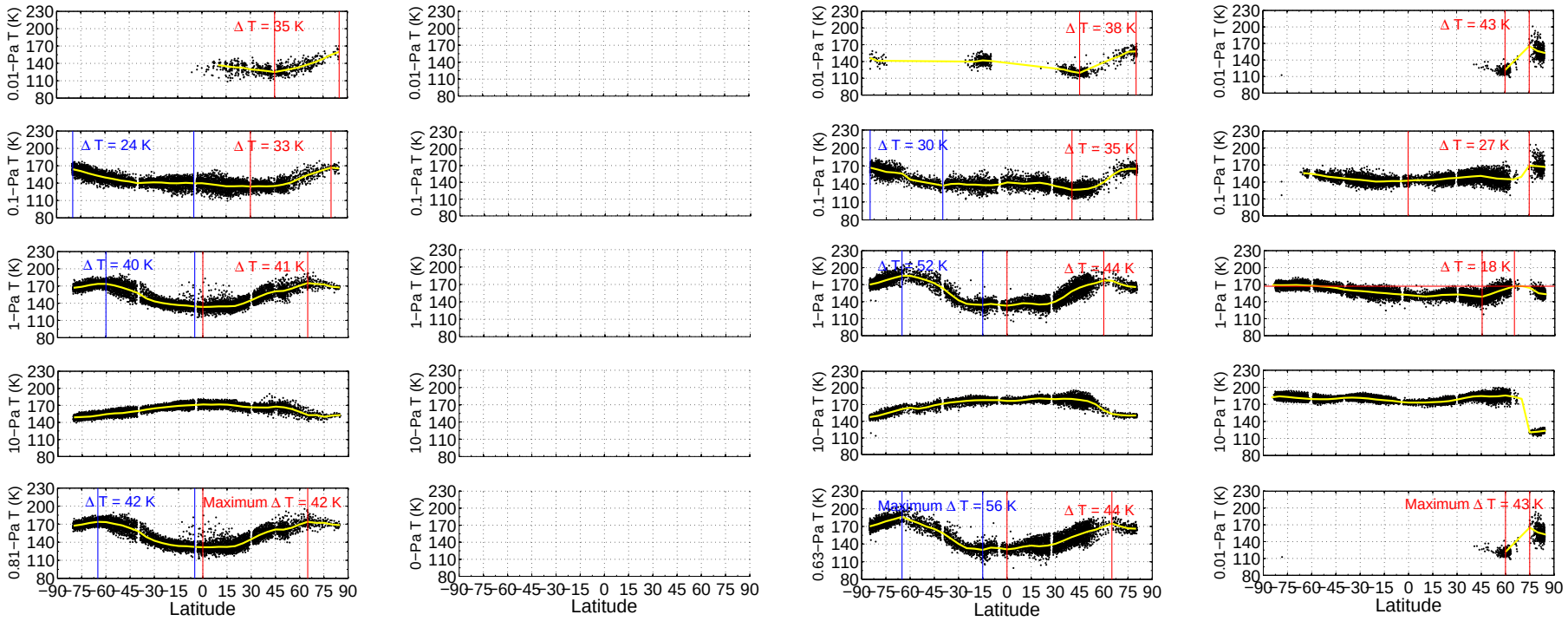

Figure A.2: Same as Figure A.1, for MY 29. From left to right: $L_s = 0°$, 90°, 180°, and 270°.

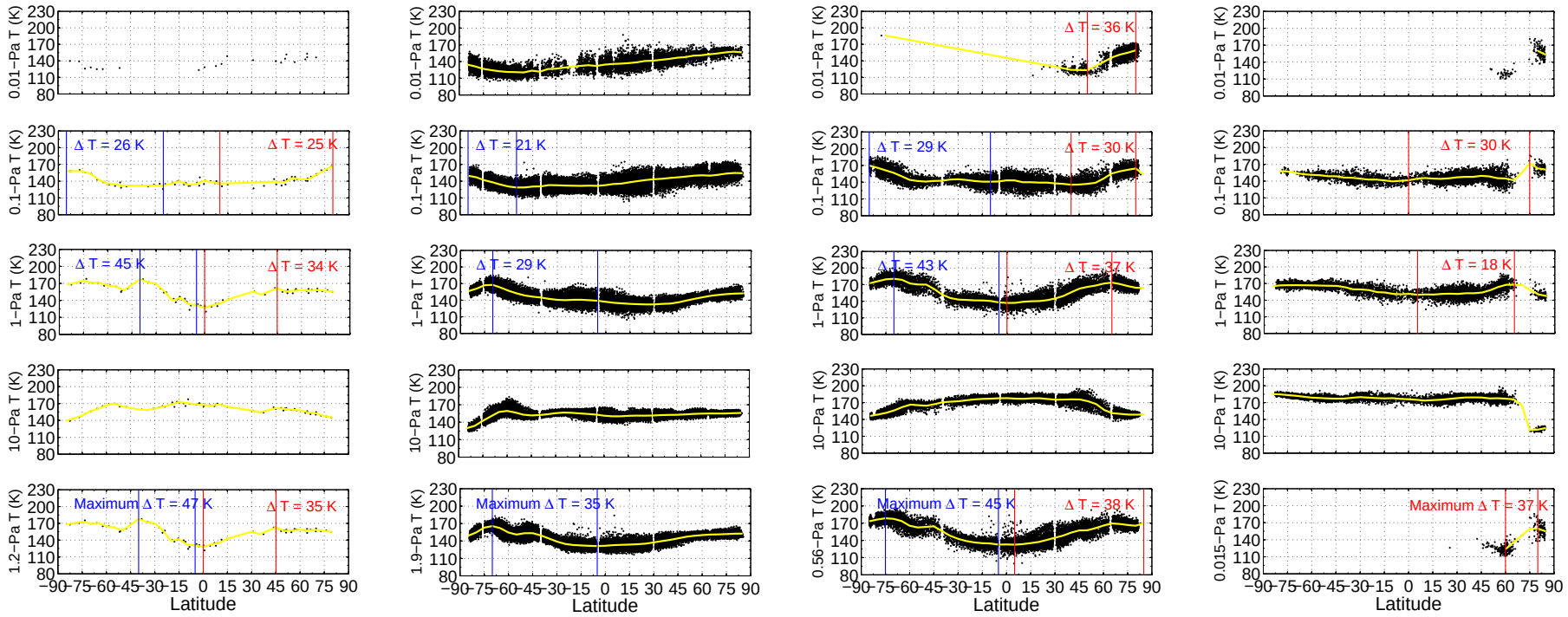

Figure A.3: Same as Figure A.1, for MY 30. From left to right: $L_s = 0°$, 90°, 180°, and 270°.

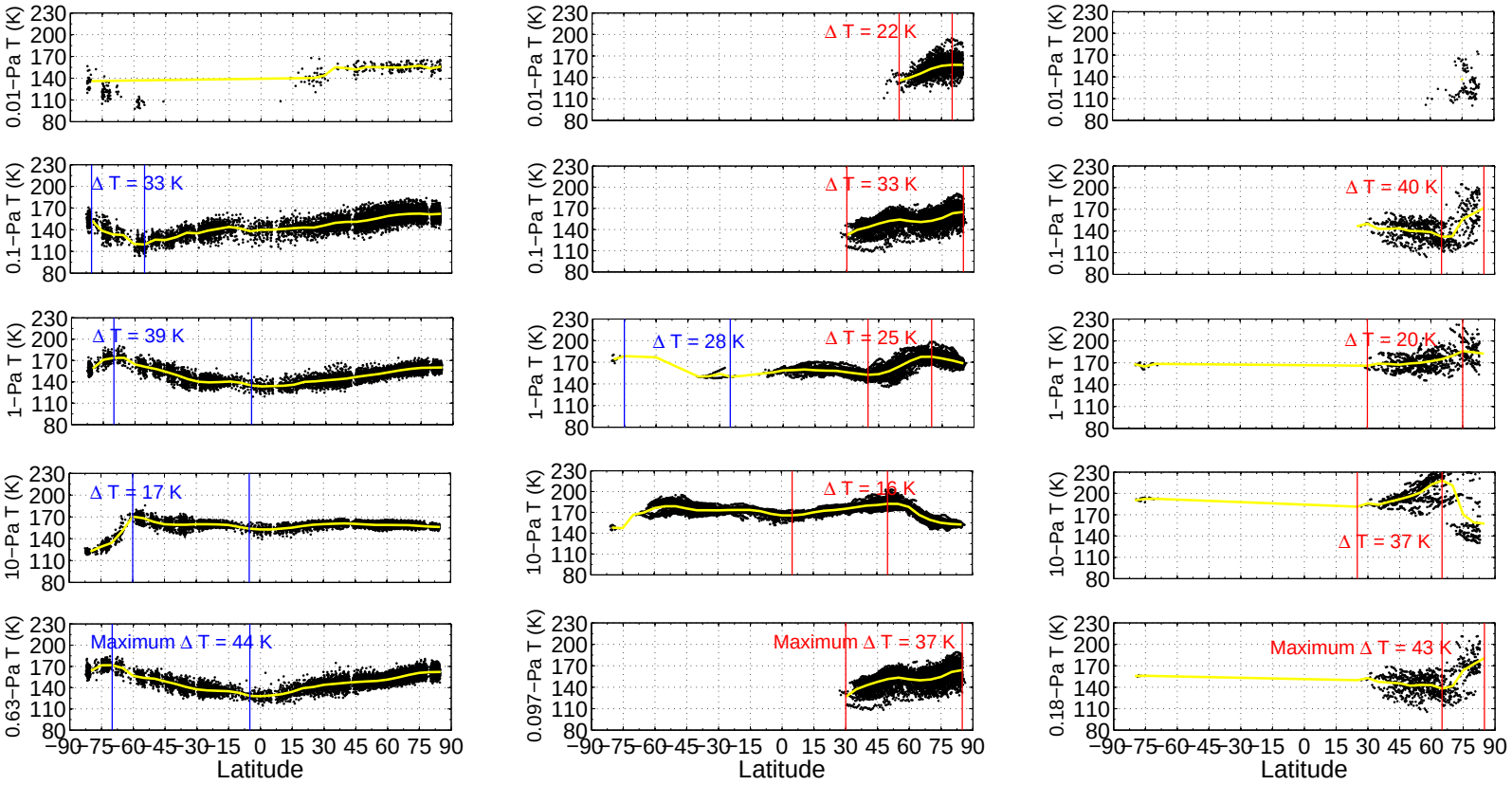

Figure A.4: Same as Figure A.1, for the dayside.

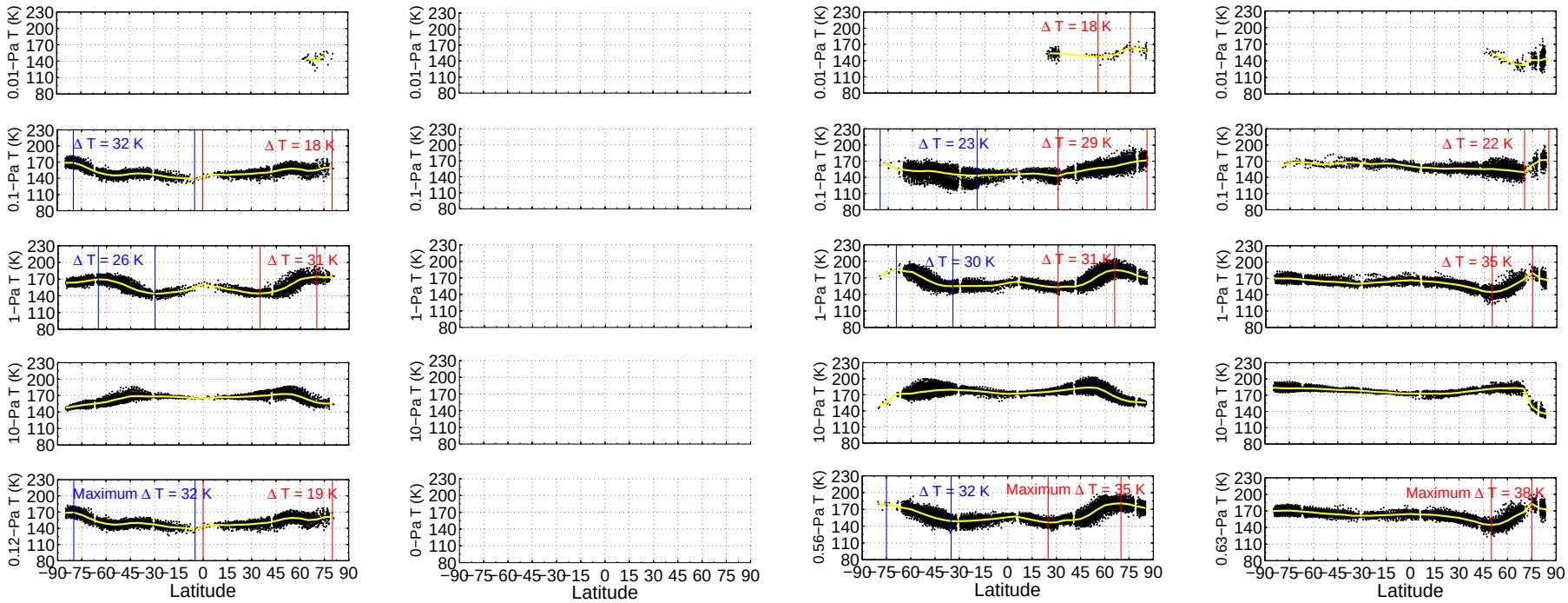

Figure A.5: Same as Figure A.2, for the dayside.

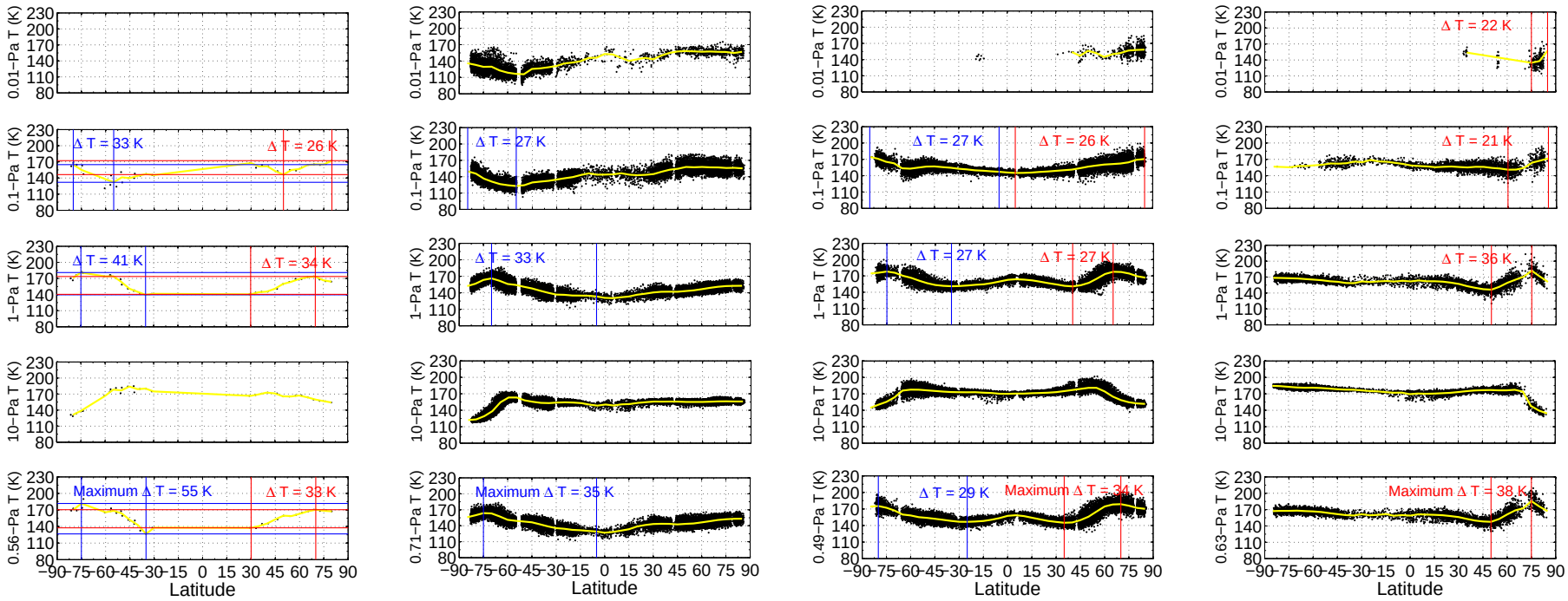

Figure A.6: Same as Figure A.3, for the dayside.

APPENDIX B

Tabulated Averaged MCS Temperatures

Lookup tables of bin-averaged MCS temperatures on select pressure surfaces at 5-degree latitude intervals are given here for the "nightside" (1-5 LT) bin and the "dayside" (13-17 LT) bin for each cardinal season. These tables can be used to: (1) test GCM calculations of middle-atmosphere temperatures, and (2) and constrain calculations of winds and gravity wave activity.

Table B.1: Nightside bin-averaged MCS temperatures on select pressure surfaces at 5-degree latitude intervals. Southern hemisphere.

p (Pa), Lat	-90	-85	-80	-75	-70	-65	-60	-55	-50	-45	-40	-35	-30	-25	-20	-15	-10	-5	0
MY 28, $Ls = \mathbf{115}^\circ$																			
5e-3																			
1e-2		132		120															
5e-2		145	142	134	133	129	126	124	126	127	123	129	131	131	131	131	133	129	134
1e-1		154	152	147	144	138	132	129	130	131	127	131	133	134	133	134	134	132	135
5e-1		164	169	173	173	170	163	154	146	142	140	140	141	143	144	146	146	145	143
1e+0		160	165	172	174	170	165	160	157	156	152	148	144	141	138	137	136	135	135
5e+0		136	141	152	163	169	165	160	157	154	153	152	151	150	149	148	148	147	147
1e+1		130	134	141	151	159	163	161	158	157	158	159	161	162	162	161	160	159	158
MY 28, $Ls = \mathbf{180}^\circ$																			
5e-3																			
1e-2																			
5e-2																		114	119
1e-1																108	115	119	122
5e-1												138	126	118	118	123	124	125	122
1e+0		171	174	178	179	182	181	176	175	167	156	142	137	137	139	138	135	133	132
5e+0		157	160	165	169	172	172	171	167	162	161	160	163	166	168	166	165	165	164
1e+1		148	150	154	158	163	163	163	164	165	167	170	171	174	176	177	178	178	177
MY 29, $Ls = \mathbf{0}^\circ$																			
5e-3																			
1e-2																			
5e-2			156	152	146	144	141	137	136	134	134	136	137	138	137	138	139	138	139
1e-1			164	161	157	153	150	147	144	143	140	141	141	141	140	140	141	140	140
5e-1			168	170	171	172	171	168	167	163	158	150	144	138	133	130	131	131	131
1e+0			167	169	172	174	174	171	167	162	158	148	144	140	138	137	136	134	134
5e+0			156	156	157	158	160	161	160	160	158	157	157	158	158	158	159	159	160
1e+1			149	150	150	152	154	156	156	158	160	163	165	166	168	169	170	171	172
MY 29, $Ls = \mathbf{90}^\circ$																			
5e-3																			
1e-2																			
5e-2																			
1e-1																			
5e-1																			
1e+0																			
5e+0																			
1e+1																			
MY 29, $Ls = \mathbf{180}^\circ$																			
5e-3																			
1e-2		146	141	141												140	142	141	
5e-2		160	157	154	151	147	137	135	135	134	133	135	137	138	139	140	139	138	140
1e-1		167	164	160	159	157	147	144	142	140	137	140	140	139	139	138	138	139	142
5e-1		170	174	178	181	184	176	172	166	161	1556	149	141	132	132	130	134	134	132
1e+0		170	173	177	182	186	186	182	178	172	164	153	143	136	135	134	136	134	133
5e+0		158	161	165	170	172	172	173	175	173	172	171	167	166	166	167	166	165	166
1e+1		147	150	154	158	162	165	163	165	169	171	174	175	177	178	178	178	178	177
MY 30, $Ls = \mathbf{0}^\circ$																			
5e-3																			
1e-2																			
5e-2		151		141															
1e-1		158		158	153	143	136		132					132	136	140	134	141	
5e-1		170		177	175	174	174	164	159		159	157	154	146	145	147	149	144	138
1e+0		168		175	171	171	166	165	158		177	172	170	156	140	145	134	132	127
5e+0		149		161	168	169	170	166	165		160	156	157	158	157	155	151	153	157
1e+1		139		149	157	161	167	170	165		160	159	161	165	168	173	171	169	168
MY 30, $Ls = \mathbf{90}^\circ$																			
5e-3		128	126																
1e-2		135	131	127	125	122	121	121	120	124	122	127	127	129	130	132	133	132	134
5e-2		143	139	133	130	128	126	125	126	128	128	132	132	132	132	132	133	133	134
1e-1		150	147	142	138	134	131	129	129	130	131	133	133	132	132	132	132	132	133
5e-1		161	165	167	166	162	156	149	142	138	136	135	137	140	143	144	144	144	141
1e+0		156	161	167	168	163	157	152	148	146	145	142	141	140	141	141	140	139	137
5e+0		135	141	152	160	164	160	155	152	148	147	146	145	144	143	142	143	143	142
1e+1		130	134	143	150	158	159	157	153	152	152	154	156	157	156	155	154	153	151
MY 30, $Ls = \mathbf{180}^\circ$																			
5e-3																			
1e-2				186															
5e-2		165	159	154	148	142	137	136	137	138	138	139	140	140	139	139	139	139	140
1e-1		170	166	161	157	151	144	142	141	142	143	145	145	144	142	141	141	141	143
5e-1		173	176	178	176	172	164	160	161	164	157	149	143	139	136	135	134	133	133
1e+0		173	176	180	181	179	172	170	170	162	152	146	143	142	141	141	140	138	137
5e+0		155	158	162	167	172	176	173	163	158	156	157	161	164	165	166	166	167	166
1e+1		146	149	152	156	162	167	165	165	167	171	172	173	174	176	177	177	178	178

Table B.2: Same as Table B.1 except for the northern hemisphere.

p (Pa), Lat	0	5	10	15	20	25	30	35	40	45	50	55	60	65	70	75	80	85	90
MY 28, $Ls = \mathbf{180}^\circ$																			
5e-3							131			147	157	182	183	170	165	162			
1e-2						129	129	132	131	137	148	162	167	155	152	152	154		
5e-2	119	119	119	120	119	122	122	122	122	124	125	129	135	141	147	153	155	144	
1e-1	122	121	118	118	118	120	122	122	124	125	125	128	134	143	151	157	159	155	
5e-1	122	120	121	122	122	125	131	136	141	147	151	159	168	172	171	169	169	169	
1e+0	132	132	133	134	133	134	138	144	152	162	169	175	179	177	174	171	168	165	
5e+0	164	163	163	162	164	167	168	169	172	174	177	178	171	163	159	157	155	153	
1e+1	177	176	177	179	179	177	177	177	178	177	174	168	158	152	150	149	149	149	
MY 28, $Ls = \mathbf{270}^\circ$																			
5e-3																			
1e-2														137	141				
5e-2	124	123	124	125	122	121	120	121	121	122	121	118	120	125	131	145	154	160	
1e-1	127	127	128	127	125	124	123	126	128	129	127	125	127	132	137	152	165	172	
5e-1	144	143	141	128	138	139	142	146	150	156	160	160	163	167	168	181	184	192	
1e+0	156	157	156	155	155	154	153	156	161	167	172	174	178	182	184	188	185	192	
5e+0	181	180	181	181	182	182	182	186	192	198	199	201	201	206	209	194	174	174	
1e+1	188	188	188	188	191	192	192	192	197	202	202	201	197	207	210	192	167	162	
MY 29, $Ls = \mathbf{0}^\circ$																			
5e-3																			
1e-2			137		133	133	130	128	127	125	128	130	133	138	142	148	154	160	
5e-2	139	138	137	135	135	134	132	132	130	130	132	135	143	147	151	158	164	163	
1e-1	140	138	136	135	135	135	134	135	134	134	137	141	147	154	158	163	167	165	
5e-1	131	131	130	130	132	137	144	150	154	158	159	160	165	169	169	170	170	168	
1e+0	134	134	135	135	135	140	145	152	157	160	162	165	171	175	174	173	169	167	
5e+0	160	160	160	159	159	158	157	157	160	163	165	167	167	164	163	163	160	159	
1e+1	172	171	172	171	170	167	166	166	166	168	166	163	158	153	153	150	152	153	
MY 29, $Ls = \mathbf{180}^\circ$																			
5e-3																			
1e-2								126	122	120				145	150	157	158	158	
5e-2	140	141	141	140	139	137	134	132	128	128	128	131	140	148	160	163	163	164	
1e-1	142	141	140	141	142	140	136	134	130	130	132	136	144	155	163	165	165	165	
5e-1	132	132	135	138	137	139	141	145	148	152	156	160	166	174	170	167	167	166	
1e+0	133	135	137	137	135	136	140	148	158	165	170	173	177	177	171	167	167	166	
5e+0	166	165	163	162	164	166	168	173	177	180	181	181	171	162	157	156	156	155	
1e+1	177	177	178	180	181	180	180	180	180	179	176	171	160	153	151	150	150	150	
MY 29, $Ls = \mathbf{270}^\circ$																			
5e-3																169	155	152	
1e-2													122			165	157	153	
5e-2	140	140	139	139	140	142	141	143	143	142	138	134	134	136	154	170	165	164	
1e-1	142	143	143	143	145	146	147	149	150	150	148	146	145	145	149	169	168	167	
5e-1	149	150	149	149	150	151	152	153	153	153	155	159	161	161	163	172	164	161	
1e+0	152	150	149	150	151	152	153	152	150	149	153	158	163	167	167	164	155	153	
5e+0	165	164	163	164	165	165	167	167	167	166	164	166	171	174	171	129	126	126	
1e+1	173	173	173	174	174	176	178	181	183	185	184	184	186	183	180	121	121	124	
MY 30, $Ls = \mathbf{0}^\circ$																			
5e-3																			
1e-2																			
5e-2		135								141	140	137	145	145	155	158	170		
1e-1	141	138	136							139	138	46	143	144	152	160	167		
5e-1	138	133	137	133			154	148		148	151	154	150	161	162	162	160		
1e+0	127	132	135	142			156	150		161	156	157	158	157	158	157	155		
5e+0	157	154	161	162			157	151		156	160	160	158	157	156	150	150		
1e+1	168	166	168	164			158	154		162	161	159	158	154	153	148	145		
MY 30, $Ls = \mathbf{180}^\circ$																			
5e-3																			
1e-2								127	124		123		138	136	151	155	159		
5e-2	140	140	139	138	136	135	134	134	131	131	133	135	143	152	158	162	164	157	
1e-1	143	143	140	140	139	139	138	137	135	136	137	139	146	155	1659	162	165	154	
5e-1	133	132	133	135	137	141	145	148	153	156	156	159	164	169	168	167	166	171	
1e+0	137	137	139	140	140	142	145	150	156	163	166	168	172	174	171	167	164	164	
5e+0	166	166	164	164	165	166	166	167	169	173	175	174	168	159	156	154	153	151	
1e+1	178	172	177	178	178	176	175	176	176	176	172	167	157	151	150	149	149	149	
MY 30, $Ls = \mathbf{270}^\circ$																			
5e-3																	157	151	
1e-2																	160	153	
5e-2	141	141	142	141	141	141	142	143	142	141	138	133	133	134	150	165	159	159	
1e-1	142	144	146	145	144	145	147	148	148	149	148	145	145	142	155	172	163	161	
5e-1	150	151	153	151	151	152	151	154	155	156	160	164	166	164	154	166	160	156	
1e+0	152	150	151	150	151	152	151	153	153	154	158	164	168	168	167	158	150	147	
5e+0	171	169	167	168	167	165	164	163	161	159	159	163	167	173	159	129	124	125	
1e+1	176	175	174	175	175	177	178	179	179	179	178	178	177	176	166	121	122	125	

APPENDIX C

Tabulated PW Observations

Tables C.1 - C.6 provide tabulated PW results from MCS, SPICAM and ACC observations for select pressure surfaces. The quantities σ_{Tmax} and σ_{Tmin} are the standard deviation of temperatures about the longitudinal mean at Lat_{Tmax} and Lat_{Tmin}, respectively. The other quantities reported are defined in Chapter 3. The top eight rows of each seasonal frame in the MCS tables show results for standard pressures interpolated by MCS. Specifically, they are the standard pressures closest to half-decade intervals of log-pressure between 10 Pa ($\sim$ 30 km altitude) and the top of the MCS dataset, $p = 5$ x 10^{-3} Pa ($\sim$ 80-90 km altitude). The bottom row of each seasonal frame (highlighted in grey) of the MCS tables shows results for the pressure at which $\Delta_p T$ maximizes in that hemisphere at that season. The SPICAM and ACC tables show results for half-decades of log pressure over the pressure ranges observed by the respective instruments.

Table C.1: Polar warming as observed by MCS. Nightside. Southern hemisphere.

MY, Ls	p (Pa)	$\Delta_p T$ (K)	T_{max} (K)	σ_{Tmax} (K)	Lat_{Tmax}	T_{min} (K)	σ_{Tmin} (K)	Lat_{Tmin}	z (km)	$\nabla_p T$ (K/°)
MY 28, $Ls = 115°$	5e-3									
	1e-2									
	5e-2	22	145	6.6	-85	123	7.5	-40	71	0.2
	1e-1	27	154	6.4	-85	127	11.4	-40	65	0.2
	5e-1	33	173	6.6	-75	140	6.0	-40	55	0.3
	1e+0	39	174	4.9	-70	135	8.4	-5	50	0.5
	5e+0	22	169	5.4	-65	147	4.4	-5	37	0.3
	1e+1									
	1.5e+0	43	174	4.4	-70	131	6.0	-5	47	0.6
MY 28, $Ls = 180°$	5e-3									
	1e-3									
	5e-2									
	1e-1									
	5e-1	20	138	1.0	-35	118	1.0	-20	61	0.4
	1e+0	49	182	4.6	-65	133	8.1	-5	53	0.7
	5e+0									
	1e+1									
	7.1e-1	53	178	3.4	-65	125	9.7	-25	56	0.6
MY 29, $Ls = 0°$	5e-3									
	1e-3									
	5e-2	22	156	4.7	-80	134	4.3	-40	77	0.2
	1e-1	24	164	6.5	-80	140	7.7	-5	71	0.3
	5e-1	42	172	3.8	-65	130	6.1	-15	60	0.5
	1e+0	40	174	4.7	-60	134	5.2	-5	55	0.6
	5e+0									
	1e+1									
	5.6e-1	42	173	3.7	-65	131	5.1	-15	59	0.5
MY 29, $Ls = 90°$	5e-3									
	1e-3									
	5e-2									
	1e-1									
	5e-1									
	1e+0									
	5e+0									
	1e+1									
MY 29, $Ls = 180°$	5e-3									
	1e-3									
	5e-2	27	160	4.1	-85	133	4.0	-40	76	0.2
	1e-1	30	167	5.4	-85	137	4.6	-40	70	0.2
	5e-1	54	184	5.5	-65	130	5.6	-15	59	0.7
	1e+0	52	186	8.8	-65	134	5.8	-15	53	0.6
	5e+0									
	1e+1									
	6.3e-1	56	186	5.8	-65	130	6.6	-15	57	0.7
MY 30, $Ls = 0°$	5e-3									
	1e-3									
	5e-2									
	1e-1	26	158	2.0	-85	132	2.8	-25	65	0.2
	5e-1	33	177	6.8	-75	144	7.2	- 5	56	0.4
	1e+0	45	177	4.1	-40	132	4.2	- 5	54	1.0
	5e+0	19	170	2.0	-60	151	0.7	-10	38	0.3
	1e+1									
	1.2e+0	47	178	1.0	-40	131	1.8	-5	53	1.0
MY 30, $Ls = 90°$	5e-3									
	1e-3									
	5e-2	18	143	5.0	-85	125	5.1	-55	69	0.1
	1e-1	21	150	5.1	-85	129	6.3	-55	63	0.2
	5e-1	32	167	5.0	-75	135	5.5	-35	54	0.3
	1e+0	29	168	4.9	-70	139	8.3	- 5	49	0.4
	5e+0	22	164	5.4	-65	142	3.3	-15	37	0.3
	1e+1									
	1.9e+0	35	166	4.6	-70	131	5.0	-5	44	0.5
MY 30, $Ls = 180°$	5e-3									
	1e-3									
	5e-2	29	165	6.5	-85	136	6.6	-55	75	0.2
	1e-1	29	170	7.7	-85	141	7.9	-10	69	0.3
	5e-1	45	178	4.7	-75	133	6.7	- 5	59	0.6
	1e+0	43	181	5.2	-70	138	5.4	- 5	53	0.6
	5e+0	20	176	6.8	-60	156	5.7	-40	41	0.2
	1e+1									
	5.6e-1	45	178	4.9	-75	133	6.3	-5	58	0.6

Table C.2: Polar warming as observed by SPICAM. Nightside. Southern hemisphere.

MY, Ls	p (Pa)	$\Delta_p T$ (K)	T_{max} (K)	Lat_{Tmax}	T_{min} (K)	Lat_{Tmin}	z (km)	$\nabla_p T$ (K/°)
	1e-4	32	135	-85	103	-45		0.3
	5e-4	20	116	-35	96	-15		0.4
	1e-3	19	120	-85	101	-15		0.2
MY 27, $Ls = \mathbf{115}^\circ$	5e-3							
	1e-2	22	139	-85	117	-35		0.2
	5e-2							
	1e-1	24	166	-85	142	-35		0.2
	1e-4	24	133	-65	109	-15		0.3
	5e-4							
	1e-3							
MY 27, $Ls = \mathbf{90}^\circ$	5e-3							
	1e-2							
	5e-2							
	1e-1							

Table C.3: Polar warming as observed by aerobraking accelerometers. Nightside. Southern hemisphere.

Ls	p (Pa)	$\Delta_p T$ (K)	T_{max} (K)	Lat_{Tmax}	T_{min} (K)	Lat_{Tmin}	z (km)	$\nabla_p T$ (K/°)
	1e-4							
	5e-4	27	142	-85	115	-75		0.2
$Ls = \mathbf{90}^\circ$	1e-3	31	140	-85	109	-75		0.2
	5e-3							

Table C.4: Polar warming as observed by MCS. Nightside. Northern hemisphere.

MY, Ls	p (Pa)	$\Delta_p T$ (K)	T_{max} (K)	σ_{Tmax} (K)	Lat_{Tmax}	T_{min} (K)	σ_{Tmin} (K)	Lat_{Tmin}	z (km)	$\nabla_p T$ (K/°)
MY 28, $Ls = 180°$	5e-3	52	183	10.2	65	131	9.5	35	100	1.7
	1e-2	38	167	10.0	60	129	9.7	25	94	1.1
	5e-2	36	155	6.7	80	119	7.8	10	77	0.5
	1e-1	41	159	13.3	80	118	10.4	10	72	0.6
	5e-1	52	172	9.4	65	120	9.7	5	62	0.9
	1e+0	47	179	10.3	60	132	8.3	0	57	0.8
	5e+0	16	178	9.1	55	162	3.8	15	45	0.4
	1e+1									
	5.5e-3	54	185	9.7	60	131	8.8	35	100	2.1
MY 28, $Ls = 270$ °	5e-3									
	1e-2									
	5e-2	42	160	6.9	85	118	2.8	55	85	1.4
	1e-1	49	172	8.5	85	123	10.7	30	80	0.9
	5e-1	54	192	17.8	85	138	8.2	20	67	0.8
	1e+0	39	192	19.5	85	153	5.4	30	61	0.7
	5e+0	29	209	16.1	70	180	6.4	5	50	0.5
	1e+1	22	210	17.2	70	188	8.5	15	43	0.4
	3.4e-1	55	188	17.6	85	133	9.7	20	70	0.9
MY 29, $Ls = 0$ °	5e-3									
	1e-2	35	160	1.7	85	125	6.0	45	93	0.9
	5e-2	34	164	7.6	80	130	5.4	45	81	1.0
	1e-1	33	167	5.2	80	134	6.2	30	75	0.7
	5e-1	40	170	7.7	80	130	10.5	15	62	0.6
	1e+0	41	175	8.7	65	134	6.1	0	57	0.6
	5e+0									
	1e+1									
	8.1e-1	42	174	8.2	65	132	5.7	0	59	0.7
MY 29, Ls =180 °	5e-3									
	1e-2	38	158	5.8	80	120	6.2	45	94	1.1
	5e-2	36	164	7.2	80	128	8.1	45	82	1.0
	1e-1	35	165	6.1	80	130	8.9	40	76	0.9
	5e-1	42	174	10.0	65	132	6.0	0	64	0.6
	1e+0	44	177	6.6	60	133	4.8	0	59	0.7
	5e+0	19	181	8.8	50	162	4.4	15	48	0.6
	1e+1									
	1.5	45	181	10.7	60	136	5.0	20	57	1.1
MY 29, $Ls = 270$ °	5e-3									
	1e-2	43	165	6.5	75	122	3.0	60	93	2.9
	5e-2	36	170	5.4	75	134	4.8	60	80	2.4
	1e-1	27	169	8.1	75	142	6.8	0	76	0.4
	5e-1	23	172	2.0	75	149	5.8	15	63	0.4
	1e+0	18	167	7.1	65	149	6.4	45	61	0.9
	5e+0									
	1e+1									
	1.0e-2	43	165	6.5	75	122	3.0	60	93	2.9
MY 30, $Ls = 0$ °	5e-3									
	1e-2									
	5e-2	35	170	4.0	80	135	5.3	5	81	0.5
	1e-1	25	161	4.2	80	136	5.3	10	75	0.4
	5e-1	29	162	4.3	75	133	2.9	15	63	0.5
	1e+0	34	161	2.8	45	127	2.6	0	57	0.8
	5e+0									
	1e+1									
	3.0e-1	38	165	1.7	70	127	0.9	15	66	0.7
MY 30, $Ls = 180$ °	5e-3									
	1e-2	36	159	6.5	80	123	5.8	50	93	1.2
	5e-2	33	164	6.5	80	131	5.5	45	81	0.9
	1e-1	30	165	6.1	80	135	5.8	40	75	0.7
	5e-1	39	171	4.2	85	132	8.2	5	61	0.5
	1e+0	37	174	8.7	65	137	6.7	0	58	0.6
	5e+0									
	1e+1									
	5e-1	39	171	4.2	85	132	8.2	5	61	0.5
MY 30, $Ls = 270$ °	5e-3									
	1e-2									
	5e-2	32	5.4	165	75	5.0	133	60	79	2.1
	1e-1	30	6.9	172	75	9.7	142	0	74	0.4
	5e-1	16	7.9	166	75	6.5	150	0	61	0.2
	1e+0	18	9.0	168	65	6.2	150	5	61	0.3
	5e+0									
	1e+1									
	1.5e-2	37	160	5.0	80	123	5.0	60	87	1.8

Table C.5: Polar warming as observed by SPICAM. Nightside. Northern hemisphere.

MY, Ls	p (Pa)	$\Delta_p T$ (K)	T_{max} (K)	Lat_{Tmax}	T_{min} (K)	Lat_{Tmin}	z (km)	$\nabla_p T$ (K/°)
MY 27, $Ls = \mathbf{180}^\circ$	1e-4	43	153	75	110	25		0.9
	5e-4							
	1e-3							
	5e-3							
	1e-2							
	5e-2							
	1e-1							
MY 27, $Ls = \mathbf{270}^\circ$	1e-4	27	137	45	110	15		0.9
	5e-4							
	1e-3	25	133	40	108	15		1.0
	5e-3							
	1e-2	30	153	40	123	35		6.0
	5e-2							
	1e-1							

Table C.6: Polar warming as observed by aerobraking accelerometers. Nightside. Northern hemisphere.

Ls	p (Pa)	$\Delta_p T$ (K)	T_{max} (K)	Lat_{Tmax}	T_{min} (K)	Lat_{Tmin}	z (km)	$\nabla_p T$ (K/°)
$Ls = \mathbf{270}^\circ$	1e-4	21	124	80	103	75		4.3
	5e-4							
	1e-3							
	5e-3							

Table C.7: Polar warming as observed by MCS. Dayside. Southern hemisphere.

MY, Ls	p (Pa)	$\Delta_p T$ (K)	T_{max} (K)	Lat_{Tmax}	T_{min} (K)	Lat_{Tmin}	z (km)	$\nabla_p T$ (K/°)
MY 28, $Ls = 115°$	5e-3							
	1e-2							
	5e-2	31	147	-80	116	-55	70	0.2
	1e-1	33	153	-80	120	-55	64	0.2
	5e-1	42	169	-75	127	-5	56	0.5
	1e+0	39	174	-70	135	-5	51	0.5
	5e+0							
	1e+1	17	171	-60	154	-5	33	0.3
	6.3e-1	44	172	-70	128	-5	55	0.6
MY 28, $Ls = 180$ °	5e-3							
	1e-2							
	5e-2							
	1e-1							
	5e-1							
	1e+0	28	179	-75	150	-25	52	0.3
	5e+0							
	1e+1							
	7.1e-1	34	181	-80	147	-10	55	0.4
MY 29, $Ls = 0$ °	5e-3							
	1e-2							
	5e-2	27	166	-85	139	-15	77	0.3
	1e-1	32	169	-80	137	-5	73	0.4
	5e-1	26	167	-75	141	-25	60	0.3
	1e+0	26	170	-65	144	-30	56	0.3
	5e+0							
	1e+1							
	1.2e-1	32	169	-80	137	-5	72	0.4
MY 29, $Ls = 90$ °	5e-3							
	1e-2							
	5e-2							
	1e-1							
	5e-1							
	1e+0							
	5e+0							
	1e+1							
MY 29, $Ls = 180$ °	5e-3							
	1e-2							
	5e-2	28	164	-80	136	-25	78	0.3
	1e-1	23	167	-80	144	-20	72	0.2
	5e-1	32	180	-75	148	-30	61	0.3
	1e+0	30	185	-70	155	-35	56	0.3
	5e+0							
	1e+1							
	3.4e-1	33	179	-80	146	-30	63	0.3
MY 30, $Ls = 0$ °	5e-3							
	1e-2							
	5e-2							
	1e-1	33	165	-80	132	-55	67	0.2
	5e-1	43	180	-75	137	-30	56	0.4
	1e+0	41	181	-75	140	-35	50	0.4
	5e+0	20	185	-60	165	-40	38	0.2
	1e+1							
	5.6e-1	55	182	-75	127	-35	55	0.5
MY 30, $Ls = 90$ °	5e-3							
	1e-2							
	5e-2							
	1e-1	27	150	-85	123	-55	63	0.2
	5e-1	32	161	-75	129	-5	55	0.4
	1e+0	33	166	-70	133	-5	50	0.4
	5e+0							
	1e+1							
	7.1e-1	35	164	-75	129	-5	52	0.4
MY 30, $Ls = 180$ °	5e-3							
	1e-2							
	5e-2	23	171	-80	148	-60	78	0.2
	1e-1	27	174	-85	147	-5	73	0.3
	5e-1	28	175	-80	147	-25	59	0.3
	1e+0	27	178	-75	151	-35	54	0.2
	5e+0							
	1e+1							
	3.0e-1	32	179	-85	147	-20	63	0.3

Table C.8: Polar warming as observed by MCS. Dayside. Northern hemisphere.

MY, Ls	p (Pa)	$\Delta_p T$ (K)	T_{max} (K)	Lat_{Tmax}	T_{min} (K)	Lat_{Tmin}	z (km)	$\nabla_p T$ (K/°)
MY 28, $Ls = 180°$	5e-3	19	164	85	145	65	98	1.0
	1e-2	22	158	80	136	55	93	0.9
	5e-2	26	157	85	131	40	80	0.6
	1e-1	33	165	85	132	30	74	0.6
	5e-1	27	175	65	148	40	66	1.1
	1e+0	25	178	70	153	40	58	0.8
	5e+0	15	176	60	161	5	46	0.3
	1e+1	16	182	50	166	5	41	0.4
	9.7e-2	37	164	85	127	30	75	0.7
MY 28, $Ls = 270$ °	5e-3							
	1e-2							
	5e-2	31	157	85	126	65	84	1.6
	1e-1	40	172	85	132	65	81	2.0
	5e-1	31	184	85	153	45	67	0.8
	1e+0	20	186	75	166	30	63	0.4
	5e+0	33	204	65	171	25	53	0.8
	1e+1	37	218	65	181	25	45	0.9
	1.8e-1	43	181	85	138	65	77	2.1
MY 29, $Ls = 0$ °	5e-3							
	1e-2							
	5e-2							
	1e-1	18	161	80	143	0	76	0.2
	5e-1	31	172	65	141	30	65	0.9
	1e+0	31	175	70	144	35	58	0.9
	5e+0							
	1e+1							
	6.3e-1	32	173	65	141	30	63	0.9
MY 29, Ls =180 °	5e-3							
	1e-2	18	165	75	147	55	96	0.9
	5e-2	20	168	85	148	30	82	0.4
	1e-1	29	172	85	143	30	76	0.5
	5e-1	35	180	70	145	25	65	0.8
	1e+0	31	184	65	153	30	59	0.9
	5e+0							
	1e+1							
	5.6e-1	35	181	70	146	25	64	0.8
MY 29, $Ls = 270$ °	5e-3							
	1e-2							
	5e-2	21	162	85	141	70	79	1.5
	1e-1	22	172	85	150	70	73	1.5
	5e-1	38	184	75	146	50	64	1.5
	1e+0	35	180	75	145	50	58	1.4
	5e+0							
	1e+1							
	6.3e-1	38	183	75	145	50	62	1.5
MY 30, $Ls = 0$ °	5e-3							
	1e-2							
	5e-2	17	167	75	150	50	84	0.7
	1e-1	26	172	80	146	50	77	0.9
	5e-1	34	172	70	138	30	64	0.8
	1e+0	34	174	70	140	30	58	0.8
	5e+0							
	1e+1							
	4.3e-1	34	172	70	138	30	65	0.9
MY 30, $Ls = 180$ °	5e-3							
	1e-2							
	5e-2	20	166	85	146	5	82	0.2
	1e-1	26	171	85	145	5	75	0.3
	5e-1	34	179	70	145	35	65	1.0
	1e+0	27	178	65	151	40	59	1.1
	5e+0							
	1e+1							
	4.9e-1	34	179	70	145	35	65	1.0
MY 30, $Ls = 270$ °	5e-3							
	1e-2	22	157	85	135	75	89	2.3
	5e-2	26	166	85	140	70	79	1.8
	1e-1	21	172	85	151	60	74	0.8
	5e-1	37	186	75	149	50	63	1.5
	1e+0	36	182	75	146	50	57	1.4
	5e+0							
	1e+1							
	6.3e-1	38	186	75	148	50	61	1.5

BIBLIOGRAPHY

BIBLIOGRAPHY

Acuña, M. H., et al. (1999), Global distribution of crustal magnetization discovered by the Mars Global Surveyor MAG/ER experiment, *Science*, *284*, 790–793.

Alexander, M. J., and T. J. Dunkerton (1999), A spectral parameterization of mean-flow forcing due to breaking gravity waves, *J. Atmos. Sci.*, *56*, 4167–4182.

Arakawa, A., and V. R. Lamb (1977), Computational design of the basic dynamical processes of the UCLA general circulation model, *Methods Comput. Phys.*, *17*, 173–265.

Arkani-Hamed, J. (2004), Timing of the martian core dynamo, *J. Geophys. Res.*, *109*(E03006), doi:10.11029/2003JE002195.

Arkani-Hamed, J. (2005), Magnetic crust of Mars, *J. Geophys. Res.*, *110*(E08005), doi:10.11029/2004JE002397.

Bandfield, J. L., V. E. Hamilton, and P. R. Christensen (2000), A global view of martian surface compositions from MGS-TES, *Science*, *287*, 1626–1630.

Barnes, J. R. (1990), Possible effects of breaking gravity waves on the circulation of the middle atmosphere of Mars, *J. Geophys. Res.*, *95*(B2), 1401–1421, doi: 10.1029/JB095iB02p01401.

Bell, J. M., S. W. Bougher, and J. R. Murphy (2007), Vertical dust mixing and the interannual variations in the Mars thermosphere, *J. Geophys. Res.*, *112*(E12002), doi:10.1029/2006JE002856.

Bertaux, J.-L., et al. (2006), SPICAM on Mars Express: Observing modes and overview of UV spectrometer data and scientific results, *J. Geophys. Res.*, *111*(E10S90), doi:10.1029/2006JE002690.

Bougher, S. W., R. E. Dickinson, R. G. Roble, and E. C. Ridley (1988), Mars thermospheric general circulation model: Calculations for the arrival of Phobos at Mars, *Geophys. Res. Lett.*, *15*, 1511–1514.

Bougher, S. W., J. Murhy, and R. Haberle (1997), Dust storm impacts on the Mars upper atmosphere, *Adv. Space Res.*, *19*(8), 1255–1260.

Bougher, S. W., S. Engel, R. G. Roble, and B. Foster (1999a), Comparative terrestrial planet thermospheres 2. solar cycle variation of global structure and winds at equinox, *J. Geophys. Res.*, *104*(E7), 16,591–16,611.

Bougher, S. W., G. Keating, R. Zurek, J. R. Murphy, R. M. Haberle, J. L. Hollingsworth, and R. T. Clancy (1999b), Mars Global Surveyor aerobraking: Atmospheric trends and model interpretation, *Adv. Space Res.*, *23*(11), 1887–1897.

Bougher, S. W., S. Engel, R. G. Roble, and B. Foster (2000), Comparative terrestrial planet thermospheres 3. solar cycle variation of global structure and winds at solstices, *J. Geophys. Res.*, *105*(E7), 17,669–17,692.

Bougher, S. W., S. Engel, D. P. Hinson, and J. R. Murphy (2004), MGS radio science electron density profiles: Interannual variability and implications for the neutral atmosphere, *J. Geophys. Res.*, *109*(E03010), doi:10.1029/2003JE002154.

Bougher, S. W., J. M. Bell, J. R. Murphy, M. A. López-Valverde, and P. G. Withers (2006), Polar warming in the Mars thermosphere: Seasonal variations owing to changing insolation and dust distributions, *Geophys. Res. Lett.*, *33*(L02203), doi: 10.1029/2005GL024059.

Bougher, S. W., P. L. Blelly, M. Combi, J. L. Fox, I. Mueller-Wodarg, A. Ridley, and R. G. Robel (2008), *Comparative Aeronomy*, chap. Neutral Upper Atmosphere and Ionosphere modeling, pp. 107–142, Springer, doi:10.1007/s11214-008-9401-9.

Bougher, S. W., T. McDunn, K. Zoldak, and J. M. Forbes (2009), Solar cycle variability of Mars dayside exospheric temperatures: Model evaluation of underlying thermal balances, *Geophys. Res. Lett.*, *36*(L05201), doi:10.1029/2008GL036376.

Bougher, S. W., T. McDunn, J. Murphy, M. Chizek, and A. Kleinböhl (2011a), Coupling of Mars lower and upper atmosphere revisited: Impacts of gravity wave momentum deposition on upper atmosphere structure, in *The Fourth International Workshop on the Mars Atmosphere: Modeling and observations*, pp. 370–373, Paris, FRANCE.

Bougher, S. W., A. Ridley, D. Pawlowski, J. M. Bell, and S. Nelli (2011b), Development and validation of the ground-to-exosphere Mars GITM code: Solar cycle and seasonal variations of the upper atmosphere, in *The Fourth International Workshop on the Mars Atmosphere: Modeling and observations*, pp. 379–381, Paris, FRANCE.

Bougher, S. W., D. A. Brain, J. L. Fox, F. Gonzalez-Gálindo, C. Simon-Wedluard, and P. G. Withers (submitted 2011), *Mars*, chap. Ch. 14 Upper Atmosphere and Ionosphere, University of Cambridge Press.

Brain, D. A., et al. (2006), On the origin of aurorae on Mars, *Geophys. Res. Lett.*, *33*(L01201), doi:10.1029/2005GL024782.

Clancy, R. T., B. J. Sandor, M. J. Wolff, P. R. Christensen, M. D. Smith, J. C. Pearl, B. J. Conrath, and R. J. Wilson (2000), An intercomparison of ground-based millimeter, MGS TES, and Viking atmospheric temperature measurements: Seasonal and interannual variability of temperatures and dust loading in the global Mars atmosphere., *J. Geophys. Res.*, *105*(E4), 9553–9571, doi:10.1029/1999JE001089.

Collins, M., S. R. Lewis, and P. L. Read (1997), Gravity wave drag in a global circulation model of the martian atmosphere: parameterisation and validation, *Adv. Space Res.*, *19*(8), 1245–1254.

Conrath, B. J. (1975), Thermal structure of the martian atmosphere during the dissipation of the dust storms of 1971, *Icarus*, *24*, 34–46.

Deming, D., M. J. Mumma, F. Espenak, T. Kostiuk, and D. Zipoy (1986), Polar warming in the middle atmosphere of Mars, *ICARUS*, *66*, 366–379.

Eckermann, S., J. Ma, and X. Zhu (2011), Scale-dependent infrared radiative damping rates on Mars and their role in the deposition of gravity-wave momentum flux, *Icarus*, *211*, 429–442.

Forbes, J. M. (2004), Tides in the middle and upper atmospheres of Mars and Venus, *Adv. Space Res.*, *33*, 125–131, doi:10.1016/j.asr.2003.05.007.

Forget, F., F. Hourdin, R. Fournier, C. Hourdin, O. Talagrand, M. Collins, S. R. Lewis, P. L. Read, and J.-P. Huot (1999), Improved general circulation models of the martian atmosphere from the surface to above 80 km, *J. Geophys. Res.*, *104*, 24,155–24,176.

Forget, F., F. Costard, and P. Lognonné (2008), *Planet Mars: Story of Another World*, Springer-Praxis, Chichester, UK.

Forget, F., F. Montmessin, J.-L. Bertaux, F. Gonzalez-Gálindo, S. Lebonnois, E. Quémerais, A. Reberac, E. Dimarellis, and M. A. López-Valverde (2009), Density and temperatures of the upper martian atmosphere measured by stellar occultations with Mars Express SPICAM, *J. Geophys. Res.*, *114*(E01004), doi:10.1029/2008JE003086.

Fox, J. L., P. Zhou, and S. W. Bougher (1995), The martian thermosphere/ionosphere at high and low solar activities, *Adv. Space Res.*, *17*(11), 203–218.

Fritts, D., L. Wang, and R. Tolson (2006), Mean and gravity wave structures and variability in the Mars upper atmosphere inferred from Mars Global Surveyor and Mars Odyssey aerobraking densities, *J. Geophys. Res.*, *111*(A12304), doi:10.1029/2006JA011897.

González-Galindo, F., F. Forget, M. A. López-Valverde, M. A. i Coll, and E. Millour (2009a), A ground-to-exosphere martian general circulation model: 1. Seasonal, diurnal, and solar cycle variation of thermospheric temperatures, *J. Geophys. Res.*, *114*(E04001), doi:10.1029/2008JE003246.

González-Galindo, F., F. Forget, M. A. López-Valverde, and M. A. i Coll (2009b), A ground-to-exosphere martian general circulation model: 2. Atmosphere during solstice conditions - Thermospheric polar warming, *J. Geophys. Res.*, *114*(E08004), doi:10.1029/2008JE003277.

Guo, X., G. Lawson, M. I. Richardson, and A. Toigo (2009), Fitting the Viking Lander surface pressure cycle with a Mars General Circulation Model, *J. Geophys. Res.*, *114*(E07006), doi:10.1029/2008JE003302.

Guo, X., M. I. Richardson, A. Soto, and A. Toigo (2010), On the mystery of the perennial carbon dioxide cap at the south pole of Mars, *J. Geophys. Res.*, *115*(E04005), doi:10.1029/2009JE003382.

Gurwell, M. A., E. A. Bergin, G. J. Melnick, and V. Tolls (2005), Mars surface and atmospheric temperature during the 2001 global dust storm, *Icarus*, *175*, 23–31, doi:10.1016/j.icarus.2004.10.009.

Haberle, R., C. Leovy, and J. Pollack (1982), Some effects of global dust storms on the atmospheric circulation of Mars, *Icarus*, *50*, 322–367.

Haberle, R. M., et al. (1999), General circulation model simulations of the Mars Pathfinder atmospheric structure investigation/meteorology data, *J. Geophys. Res.*, *104*(E4), doi:10.1029/1998JE900040.

Haberle, R. M., J. R. Murphy, and J. Schaeffer (2003), Orbital change experiments with a Mars general circulation model, *Icarus*, *161*, 66–89, doi:10.1016/S0019-1035(02)00017-9.

Hanson, W. B., S. Sanatani, and D. R. Zuccaro (1977), The martian ionosphere as observed by the Viking Retarding Potential Analyzers, *J. Geophys. Res.*, *82*(28), 4,351–4,363.

Hartogh, P., A. Medvedev, T. Kuroda, R. Saito, G. Villanueva, A. Feofilov, A. Kutepov, and U. Berger (2005), Description and climatology of a new general circulation model of the martian atmosphere, *J. Geophys. Res.*, *110*(E11008), doi:10.1029/2005JE002498.

Hartogh, P., A. S. Medvedev, and C. Jarchow (2007), Middle atmosphere polar warmings on Mars: Simulations and study on the validation with sub-millimeter observations, *Plan. and Space Sci.*, *55*, 1103–1112, doi:10.1016/j.pss.2006.11.018.

Heavens, N. G. (2010), The impact of mesoscale processes on the atmospheric circulation of Mars, Ph.D. thesis, California Institute of Technology, Pasadena, CA, USA.

Heavens, N. G., M. I. Richardson, W. G. Lawson, D. J. McCleese, D. M. Kass, A. Kleinböhl, J. T. Schofield, W. A. Abdou, and J. H. Shirley (2010), Convective instability in the martian middle atmosphere, *ICARUS*, *208*, 574–589, doi:10.1016/j.icarus.2010.03.023.

Heavens, N. G., D. J. McCleese, M. I. Richardson, D. M. Kass, A. Kleinböhl, and J. T. Schofield (2011a), Structure and dynamics of the martian lower and middle atmosphere as observed by the Mars Climate Sounder: 2. Implications of the thermal structure and aerosol distributions for the mean meridional circulation, *J. Geophsy. Res.*, *116*(E01010), doi:10.1029/2010JE003713.

Heavens, N. G., et al. (2011b), Vertical distribution of dust in the martian atmosphere during northern spring and summer: High-altitude tropical dust maximum at northern summer solstice, *J. Geophys. Res.*, *116*(E01007), doi:10.1029/2010JE003692.

Holton, J. R. (1982), The role of gravity wave induced drag and diffusion in the momentum budget of the mesosphere, *J. Atmos. Sci.*, *39*, 791–799.

Hong, S. Y., and H. L. Pan (1996), Nonlocal boundary layer vertical diffusion in a Medium-Range Forecast Model, *Mon. Weather Rev.*, *124(10)*, 2322–2339.

Huestis, D. L., S. W. Bougher, J. L. Fox, M. Galand, R. E. Johnson, J. L. Moses, and J. C. Pickering (2008), Cross sections and reaction rates for comparative planetary aeronomy, *Space Sci. Rev.*, *139*, 63–105, doi:10.1007/s11214-008-9383-7.

Jacobson, M. Z. (1999), *Fundamentals of Atmospheric Modeling*, Cambridge Univ. Press, Cambridge, U.K.

Jakosky, B. M., and C. B. Farmer (1982), The seasonal and global behavior of water vapor in the Mars atmosphere: Complete global results of the Viking Atmospheric Water Detector Experiment, *J. Geophys. Res.*, *87*(B4), 2999–3019.

Jakosky, B. M., and T. Z. Martin (1987), Mars: North-polar atmospheric warming during dust storms, *Icarus*, *72*, 528–534.

Johnson, S. S., M. A. Mischna, T. L. Grove, and M. T. Zuber (2008), Sulfur-induced greenhouse warming on early Mars, *J. Geophys. Res.*, *113*(E08005), doi:10.1029/2007JE002962.

Kahre, M. A., J. R. Murphy, and R. M. Haberle (2006), Modeling the martian dust cycle and surface dust reservoirs with the NASA Ames general circulation model, *J. Geophys. Res.*, *111*(6008), doi:10.1029/2005JE002588.

Kahre, M. A., J. L. Hollingsworth, R. M. Haberle, and J. R. Murphy (2008), Investigations of the variability of dust particle sizes in the martian atmosphere using the NASA Ames Mars General Circulation Model, *Icarus*, *195*, 576–597, doi:10.1016/j.icarus.2008.01.023.

Keating, G. M., et al. (1998), The structure of the upper atmosphere of Mars: In situ accelerometer measurements from Mars Global Surveyor, *Science*, *279*(5357), 1672–1676.

Keating, G. M., M. E. Theriot, R. H. Tolson, S. W. Bougher, F. Forget, M. A. i Coll, and J. M. Forbes (2003), Recent detection of winter polar warming in the Mars upper atmosphere, in *The Third International Mars Polar Science Conference*, pp. 8033–+, Pasadena, California.

Keating, G. M., S. W. Bougher, M. E. Theriot, R. W. Zurek, R. C. Blanchard, R. H. Tolson, and J. R. Murphy (2006), Atmospheric structure from Mars Reconnaissance Orbiter accelerometer measurements, in *Europlanet 1: Proceedings of European Planetary Science Congress*, p. 644, Berlin, Germany.

Keating, G. M., S. W. Bougher, M. E. Theriot, and R. H. Tolson (2008), Properties of the Mars upper atmosphere derived from accelerometer measurements., in *Proceedings of 37th COSPAR Scientific Assembly 2008 and 50th Anniversary*, Montreal, Canada.

Kellogg, W. W., and G. F. Schilling (1951), A proposed model of the circulation in the upper stratosphere, *J. Meteorology*, *8*, 222–230.

Kieffer, H. H. (1979), Mars south polar spring and summer temperatures: A residual CO_2 frost, *J. Geophys. Res.*, *84*(B14), 8263–8288.

Kieffer, H. H., B. M. Jakosky, C. W. Snyder, and M. S. Matthews (Eds.) (1992), *Mars*, University of Arizona Press, Tuscon, AZ, USA.

Kleinböhl, A., et al. (2009), Mars Climate Sounder limb profile retrieval of atmospheric temperature, pressure, and dust and water ice opacity, *J. Geophys. Res.*, *114*(E10006), doi:10.1029/2009JE00358.

Kleinböhl, A., J. T. Schofield, W. A. Abdou, P. G. J. Irwin, and R. J. de Kok (2011), A single-scattering approximation for infrared radiative transfer in limb geometry in the martian atmosphere, *J. Quant. Spectrosc. Radiat. Transfer*, *112*, 1568–1580, doi:10.1016/j.jqsrt.2011.03.006.

Kuroda, T., A. Medvedev, P. Hartogh, and M. Takahashi (2009), On forcing the winter polar warmings in the martian middle atmosphere during dust storms, *J. Meteorol. Soc. Japan*, *87*, 913–921, doi:10.2151/jmsj.87.913.

Laprise, R. (1992), The Euler equations of motion with hydrostatic-pressure as an independent variable, *Mon. Weather Rev.*, *120*(1), 197–208.

Lee, C., et al. (2009), Thermal tides in the martian middle atmosphere as seen by the Mars Climate Sounder, *J. Geophys. Res.*, *114*(E03005), doi:10.1029/2008JE003285.

Leovy, C. B. (1964), Simple models of thermally driven mesospheric circulations, *J. Atmos. Sci.*, *21*, 327–341.

Leovy, C. B., and Y. Mintz (1969), Numerical simulations of the atmospheric circulation and climate of Mars, *J. Atmos. Sci.*, *26*(6), 1167–1190.

Lewis, S. R., M. Collins, P. L. Read, F. Forget, F. Hourdin, R. Fournier, C. Hourdin, and O. Talagrand (1999), A climate database for Mars, *J. Geophys. Res.*, *104*(E10), 24,177–24,194.

Lindzen, R. (1981), Turbulence and stress due to gravity wave and tidal breakdown, *J. Geophys. Res.*, *86*, 9707–9714.

Liou, K. N. (2002), *An Introduction to Atmospheric Radiation*, Academic Press, San Diego, CA.

Liu, J., M. I. Richardson, and R. J. Wilson (2003), An assessment of the global, seasonal, and interannual spacecraft record of martian climate in the thermal infrared, *J. Geophys. Res.*, *108*(E8), doi:10.1029/2002JE001921.

López-Valverde, M. A., D. P. Edwards, M. López-Puertas, and C. Roldán (1998), Nonlocal thermodynamic equilibrium in general circulation models of the martian atmosphere 1. effects of the local thermodynamic equilibrium approximation on thermal cooling and solar heating, *J. Geophys. Res.*, *103*, 16,799–16,812.

Magalhães, J. A., J. T. Schofield, and A. Seiff (1999), Results of the Mars Pathfinder atmospheric structure investigation, *J. Geophys. Res.*, *104*(E4), 8943–8956.

McCleese, D. J., et al. (2008a), Intense polar temperature inversion in the middle atmosphere on Mars, *Nature Geoscience*, *1*, 745–749, doi:10.1038/ngeo332.

McCleese, D. J., A. Kleinböhl, M. Richardson, T. Schofield, G. Lawson, N. Heavens, D. Kass, R. Zurek, and W. Abdou (2008b), Vertical profiling of the martian atmosphere with the Mars Climate Sounder, in *The 37th Scientific Assembly of the Committee on Space Research*, pp. B02–0009–08, Montreal, CANADA.

McCleese, D. J., et al. (2010), The structure and dynamics of the martian lower and middle atmosphere as observed by the Mars Climate Sounder: Seasonal variations in zonal mean temperature, dust and water ice aerosols, *J. Geophys. Res.*, *115*(E12016), doi:10.1029/2010JE003677.

McDunn, T., S. Bougher, M. Mischna, J. Murphy, and S. Nelli (2011), Modeling polar warming at Mars: Preliminary results of the newly vertically extended MARS-WRF GCM and comparisons with constraints from data, in *The Fourth International Workshop on the Mars Atmosphere: Modeling and observations*, pp. 382–383, Paris, FRANCE.

McDunn, T. L., S. W. Bougher, J. Murphy, M. D. Smith, F. Forget, J.-L. Bertaux, and F. Montmessin (2010), Simulating the density and thermal structure of the middle atmosphere (80-130 km) of Mars using the MGCM-MTGCM: A comparison with MEX/SPICAM observations, *ICARUS*, *206*, 5–17, doi:10.1016/j.icarus.2009.06.034.

Medvedev, A., E. Yigit, and P. Hartogh (2011a), Estimates of gravity wave drag on Mars: Indication of a possible lower thermospheric wind reversal, *Icarus*, *211*, 909–912, doi:10.1016/j.icarus2010.10.013.

Medvedev, A. S., and P. Hartogh (2007), Winter polar warmings and the meridional transport on Mars simulated with a general circulation model, *ICARUS*, *186*, 97–110, doi:10.1016/j.icarus.2006.08.020.

Medvedev, A. S., E. Yigit, P. Hartogh, and E. Becker (2011b), Influence of gravity waves on the martian atmosphere: General circulation modeling, *J. Geophys. Res.*, *116*(E10004), 14–32, doi:doi:10.1029/2011JE003848.

Mellor, G. L., and T. Yamada (1982), Development of a turbulence closure model for geophysical fluid problems, *Rev. Geophys.*, *20*, 851–875.

Mischna, M., and R. J. Wilson (2008), The Mars general circulation model intercomparison study, in *Third International Workshop on the Mars Atmosphere: Modeling and observations*, Williamsburg, VA.

Mischna, M. A. (2004), Origin and evolution of volatiles on Mars, Ph.D. thesis, University of California, Los Angeles, Los Angeles, CA, USA.

Mischna, M. A., M. Allen, M. I. Richardson, C. E. Newman, and A. D. Toigo (2011), Atmospheric modeling of Mars methane surface releases, *Planet. and Space Science*, *59*, 227–237, doi:10.1016/j.pss.2010.07.005.

Montmessin, F., et al. (2006), Subvisible co_2 ice clouds detected in the mesosphere of Mars, *Icarus*, *183*, 403–410, doi:10.1016/j.icarus.2006.03.015.

Moudden, Y., and J. M. Forbes (2008), Effects of vertically propagating thermal tides on the mean structure and dynamics of Mars' lower thermosphere, *Geophys. Res. Lett.*, *35*(L23805), doi:10.1029/2008GL036086.

Murphy, J. R., J. B. Pollack, R. M. Haberle, C. B. Leovy, O. B. Toon, and J. Schaeffer (1995), Three-dimensional numerical simulation of martian global dust storms, *J. Geophys. Res.*, *100*(E12), 26,357–26,376.

Nappo, C. (2002), *An Introduction to Atmospheric Gravity Waves*, Academic Press, San Diego, CA.

Nelli, S. M., J. R. Murphy, A. L. Sprague, W. V. Boynton, K. E. Kerry, D. M. Janes, and A. E. Metzger (2007), Dissecting the polar dichotomy of the noncondensable gas enhancement on Mars using the NASA Ames Mars General Circulation Model, *J. Geophys. Res.*, *112*(E08S91), doi:10.1029/2006JE002849.

Newman, C. E., S. R. Lewis, and P. L. Read (2005a), The atmospheric circulation and dust activity in different orbital epochs on Mars, *Icarus*, *174*, 135–160, doi:10.1016/j.icarus.2004.10.023.

Newman, C. E., S. R. Lewis, P. L. Read, and F. Forget (2005b), Modeling the dust cycle in a Mars general circulation model, 1. Representations of dust transport processes, *J. Geophys. Res.*, *107*(E12), 5123, doi:10.1029/2002JE001910.

Nier, A. O., and M. B. McElroy (1977), Composition and structure of Mars' upper atmosphere: Results from the Neutral Mass Spectrometers on Viking 1 and 2, *J. Geophys. Res.*, *82*(28), 4341–4349.

Ockert-Bell, M. E., J. F. Bell, J. B. Pollack, C. P. McKay, and F. Forget (1997), Absorption and scattering properties of the martian dust in the solar wavelengths, *J. Geophys. Res.*, *102*(E4), 9039–9050.

Palmer, T., G. Shutts, and R. Swinbank (1986), Alleviation of a systematic westerly bias in general circulation and numerical weather prediction models through an orographic gravity wave drag parameterization, *Quart. J. R. Met. Soc.*, *112*, 1001–1039.

Parish, H. F., G. Schubert, M. P. Hickey, and R. L. Walterscheid (2009), Propagation of tropospheric gravity waves into the upper atmosphere of Mars, *Icarus*, *203*, 28–37, doi:10.1016/j.icarus.2009.04.03.

Pawlowski, D., S. Bougher, and A. Ridley (2010), The effect of solar variability on the martian thermosphere and ionosphere system, in *The 38th Scientific Assembly of the Committee on Space Research*, p. 74, Bremen, GERMANY.

Pollack, J., D. Colburn, F. Flasar, R. Kahn, C. Carlston, and D. Pidek (1979), Properties and effects of dust particles suspended in the martian atmosphere, *J. Geophys. Res.*, *84*(B6).

Pruppacher, H. R., and J. D. Klett (2000), *Microphysics of Clouds and Precipitation*, 416 pp., Kluwer Academic Publishers.

Quémerais, E., J.-L. Bertaux, O. Korablev, E. Dimarellis, C. Cot, B. R. Sandel, and D. Fussen (2006), Stellar occultations observed by SPICAM on Mars Express, *J. Geophys. Res.*, *111*(E09S04), doi:10.1029/2005JE002604.

Read, P. L., and S. R. Lewis (2004), *The Martian Climate Revisited*, Springer-Praxis, Chichester, UK.

Rennó, N. O., and M. Mehta (2010), Deliquescence, liquid water, and the search for sources and sinks of methane on Mars, in *Proceedings of SPIE*, vol. 7819, doi:10.1117/12.863653.

Rennó, N. O., et al. (2004), MATADOR 2002: A pilot field experiment on convective plumes and dust devils, *J. Geophys. Res.*, *109*(E07001), doi:10.1029.2003JE002219.

Rennó, N. O., et al. (2009), Possible physical and thermodynamical evidence for liquid water at the Phoenix landing site, *J. Geophys. Res.*, *114*(E00E03), doi:10.1029.2009JE003362.

Richardson, M. I., and R. J. Wilson (2002), A topographically forced asymmetry in the martian circulation and climate, *Nature*, *416*, 298–301.

Richardson, M. I., A. D. Toigo, and C. E. Newman (2007), PlanetWRF: A general purpose, local to global numerical model for planetary atmospheric and climate dynamics, *J. Geophys. Res.*, *112*(E09001), doi:10.1029/2006JE002825.

Santee, M., and D. Crisp (1993), Thermal structure an dust loading of the martian atmosphere during late southern summer: Mariner 9 revisited, *J. Geophys. Res.*, *98*(E2), 3261–3279.

Schneider, E. K. (1983), Martian great dust storms: Interpretive axially symmetric models, *ICARUS*, *55*, 302–331.

Schofield, J. T., J. R. Barnes, D. Crisp, R. M. Haberle, S. Larsen, J. A. Magalhaes, J. R. Murphy, A. Seiff, and G. Wilson (1997), The Mars Pathfinder Atmopsheric Structure Investigation/Meteorology (ASI/MET) Experiment, *Science*, *278*, 1752–1757.

Schunk, R. W., and A. F. Nagy (2009), *Ionospheres: Physics, Plasma Physics, and Chemistry*, 2^{nd} ed., Cambridge University Press, New York, NY.

Seiff, A., and D. B. Kirk (1977), Structure of the atmosphere of Mars in summer at mid-latitudes, *J. Geophys. Res.*, *82*, 4364–4378.

Skamarock, W. C., J. B. Klemp, J. Dudhia, D. O. Gill, D. M. Barker, M. G. Duda, X.-Y. Huang, W. Wang, and J. G. Powers (2008), A description of the Advanced Research WRF version 3, *NCAR Technical Note TN-475+STR*, NCAR, Boulder, CO.

Smagorinsky, J. (1963), General circulation experiments with the primitive equations, *Mon. Weather Rev.*, *91(3)*, 99–164.

Smith, D. E., and M. T. Zuber (1996), The shape of Mars and the topographic signature of the hemispheric dichotomy, *Science*, *271*, 184–188.

Smith, D. E., et al. (1999), The global topography of Mars and implications for surface evolution, *Science*, *284*(5419), 1495–1503.

Smith, M. D. (2002), The annual cycle of water vapor on Mars as observed by the Thermal Emission Spectrometer, *J. Geophys. Res.*, *107*(E11), doi: 10.1029/2001JE001522.

Smith, M. D. (2003), TES limb-geometry observations of aerosols, in *The Sixth International Conference on Mars*, pp. 3174–+, Pasadena, California.

Smith, M. D. (2004), Interannual variability in TES atmospheric observations of Mars during 1999-2003, *Icarus*, *167*, 148–165, doi:doi:10.1016/j.icarus.2003.09.010.

Smith, M. D. (2008), Spacecraft observations of the martian atmosphere, *Annu. Rev. Earth Planet. Sci.*, *36*, 191–219, doi:10.1146/annurev.earth.36.031207.124334.

Smith, M. D. (2009), THEMIS observations of Mars aerosol optical depth from 20022008, *Icarus*, *202*, 444–452, doi:10.1016/j.icarus.2009.03.027.

Smith, M. D., J. C. Pearl, B. J. Conrath, and P. R. Christensen (2001), Thermal Emission Spectrometer results: Mars atmospheric thermal structure and aerosol distribution, *J. Geophys. Res.*, *106*(E10), 23,929–23,945, doi:doi:10.1029/2000JE001321.

Smith, M. D., M. J. Wolff, N. Spanovich, A. Ghosh, D. Banfield, P. R. Christensen, G. A. Landis, and S. W. Squyres (2006), One martian year of atmospheric observations using MER Mini-TES, *J. Geophys. Res.*, *111*(E12S13), doi:10.1029/2006JE002770.

Smith, M. D., S. Bougher, T. Encrenaz, F. Forget, and A. Kleinböhl (submitted 2011), *Mars*, chap. Ch. 4 Thermal Structure and Composition, University of Cambridge Press.

Sonnabend, G., M. Sornig, P. J. Krötz, R. T. Schieder, and K. E. Fast (2006), High spatial resolution mapping of Mars mesospheric zonal winds by infrared heterodyne spectroscopy of CO_2, *GRL*, *33*(L18201), doi:10.1029/2006GL026900.

Sprague, A. L., W. V. Boynton, K. E. Kerry, D. M. Janes, D. M. Hunten, K. J. Kim, R. C. Reedy, and A. E. Metzger (2004), Mars' south polar Ar enhancement: A tracer for south polar seasonal meridional mixing, *Science*, *306*, 1364–1367.

Sprague, A. L., et al. (2007), Mars' atmospheric argon: tracer for understanding martian atmospheric circulation and dynamics, *J. Geophys. Res.*, *112*(E03S02), doi:10.1029/2005JE002597.

Stewart, A. I. F., M. J. Alexander, R. R. Meier, L. J. Paxton, S. W. Bougher, and C. Fesen (1992), Atomic oxygen in the martian thermosphere, *J. Geophys. Res.*, *97*, 91–102.

Suarez, M. J., and L. L. Takacs (1995), Technical report series on global modeling and data assimilation. documentation of the AIRES/GEOS dynamical core, version 2, *NASA Technical Memorandum 104606*, *5*.

Tasahashi, Y. O., H. Fujiwara, and H. Fukunishi (2003), Topographically induced north-south asymmetry of the meridional circulation in the martian atmosphere, *J. Geophys. Res.*, *108*(E3), doi:10.1029/2001JE001638.

Théodore, B., E. Lellouch, E. Chassefière, and A. Hauchecorne (1993), Solstitial temperature inversions in the martian middle atmosphere: Observational clues and 2-D modeling, *ICARUS*, *105*, 512–528.

Thomas, P., and P. Gierasch (1985), Dust devils on Mars, *Science*, *230*, 175–177.

Tillman, J. E. (1988), Mars global atmospheric oscillations: Annually synchronized, transient normal-mode oscillations and the triggering of global dust storms, *J. Geophys. Res.*, *93*(D8), 9433–9451.

Tolson, R. H., G. M. Keating, G. J. Cancro, J. S. Parker, S. N. Noll, and B. L. Wilkerson (1999), Application of accelerometer data to Mars Global Surveyor aerobraking operations, *J. Spacecraft and Rockets*, *36*, 323–329, doi:10.2514/2.3474.

Tolson, R. H., G. M. Keating, S. N. Noll, D. T. Baird, and T. J. Shellenberg (2000), *Astrodynamics 1999, Volume 103 of the Advances in the Astronautical Sciences Series*, chap. Utilization of Mars Global Surveyor accelerometer data for atmospheric modeling, pp. 1329–1346, American Astronautical Society.

Tolson, R. H., A. M. Dwyer, J. L. Hanna, G. M. Keating, B. E. George, P. E. Escalera, and M. R. Werner (2005), Application of accelerometer data to Mars Odyssey aerobraking and atmospheric modeling, *J. Spacecraft and Rockets*, *42*, 435–443, doi:10.2514/1.15173.

Tolson, R. H., et al. (2008), Atmospheric modeling using accelerometer data during Mars Reconnaissance Orbiter aerobraking operations, *J. Spacecraft and Rockets*, *45(3)*, 511–518, doi:10.2514/1.34301.

Tomasko, M. G., L. R. Doose, M. Lemmon, P. H. Smith, and E. Wegryn (1999), Properties of dust in the martian atmosphere from the imager on Mars Pathfinder, *J. Geophys. Res.*, *104*(E4), 8987–9007.

Toon, O., J. Pollack, and C. Sagan (1977), Physical properties of the particles composing the martian dust storm of 1971-1972, *Icarus*, *30*, 663–696.

Wallace, J., and P. Hobbs (1977), *Atmospheric Science, An Introductory Survey*, Academic Press, San Diego, CA.

Wilson, R. J. (1997), A general circulation model simulation of the martian polar warming, *Geophys. Res. Lett.*, *24*(2), 123–126.

Wilson, R. J., Y. Takahashi, F. Forget, M. Mischna, T. Kuroda, Y. Moudden, and A. Medvedev (2006), Mars general circulation model intercomparison, in *Second International Workshop on the Mars Atmosphere: Modeling and observations*, Granada, Spain.

Withers, P. (2006), Mars Global Surveyor and Mars Odyssey Accelerometer observations of the martian upper atmosphere during aerobraking, *Geophys. Res. Lett.*, *33*(L02201), doi:10.1029/2005GL024447.

Withers, P., M. C. Towner, B. Hathi, and J. C. Zarnecki (2003a), Analysis of entry accelerometer data: A case study of Mars Pathfinder, *Plan. and Space Sci.*, *51*, doi:10.1016/S0032-0633(03)00077-1.

Withers, P., R. Pratt, J.-L. Bertaux, and F. Montmessin (2011), Observations of thermal tides in the middle atmosphere of Mars by the SPICAM instrument, *J. Geophys. Res.*, *116*(E11005), doi:10.1029/2011JE003847.

Withers, P. G., S. W. Bougher, and G. M. Keating (2003b), The effects of topographically-controlled thermal tides in the martian upper atmosphere as seen by the MGS accelerometer, *Icarus*, *164*, 14–32, doi:doi:10.1016/S0019-1035(03)00135-0.

Wolff, M. J., et al. (2006), Constraints on dust aerosols from the Mars Exploration Rovers using MGS overflights and Mini-TES, *J. Geophys. Res.*, *111*(E12S17), doi:10.1029/2006JE002786.